Direct Numerical Simulation Studies of Sedimentation of Spherical Particles

Adnan Hamid

2014

KYOTO UNIVERSITY

Abstract

Department of Chemical Engineering

Doctor of Philosophy

Direct Numerical Simulation Studies of Sedimentation of Spherical Particles

by Adnan Hamid

The behavior of sedimenting particles is investigated widely due to its ubiquitous nature and industrial applications, such as paper and pulp, water purification and hydro-power dams. Despite the extensive research, sedimentation is still an active area of non-equilibrium dynamics due to its paradoxical nature. In order to explore this enigmatic phenomena, we performed direct numerical simulations of mono-dispersed spherical particles, using the smoothed profile method and investigated the evolution of its microstructure, static (time independent) and dynamic properties (time dependent): (1) at finite Peclet number (Pe) in the Stokes regime, which measures the interplay of thermal and hydrodynamic forces; (2) at high Pe and low Reynolds number (Re), where particles show typical non-Brownian characteristics; (3) at finite Re, where inertial forces have significant effects on transport properties.

Firstly, we investigated the scaling of hydrodynamic velocity fluctuations and the self-diffusion of sedimenting particles at finite Pe over a moderate range of volume fractions ($0.01 \leq \phi \leq 0.12$). We found a complete transition from an isotropic microstructure at low Pe due to the dominance of the thermal force to an anisotropic microstructure at high Pe, where particles preferred to orient themselves in the horizontal direction with respect to neighbouring particles. Apart from these two regimes, we also observed a transition regime, where both of these forces interplay. We observed that at $\mathrm{Pe} \gtrsim 30$, velocity fluctuations scaled with the Stokes velocity, their relaxation times scaled with the Stokes time and the particle diffusion scaled with the product of the Stokes velocity and the particle radius remained unchanged, showing the dominating effects of hydrodynamic forces. Moreover, the diffusion anisotropy increased with increasing Pe and saturated at high Pe values.

Secondly, we investigated the non-Brownian sedimenting particles ($\mathrm{Pe} \gtrsim 80$) over a wide range of volume fractions from 0.01 to 0.5. The microstructure analysis of the suspension showed that at low volume fractions, the anisotropic microstructure determined the transport properties and at $\phi \gtrsim 0.15$, many-body interactions dominated the phenomena, whereas a cross-over existed in between these two regimes. We found that hydrodynamic velocity fluctuations scaled as $\phi^{1/2}$, both parallel and perpendicular to gravity at the low volume fraction regime ($\phi \lesssim 0.04$) due to

an anisotropic microstructure, remained unchanged at the cross-over regime ($0.04 < \phi \lesssim 0.12$) and decayed sharply at high volume fractions because of many-body hydrodynamic interactions. Unlike velocity fluctuations, vertical relaxation times scaled as $\phi^{-1/2}$ for the full range of volume fractions, whereas horizontal relaxation times decreased as $\phi^{-1/2}$ at low volume fractions, remained unchanged and then decreased sharply at high volume fractions. Similarly, horizontal and vertical diffusion coefficients increased as $\phi^{1/2}$ at low volume fraction. Moreover, the vertical diffusion decayed with further increase in the ϕ, whereas the horizontal diffusion remained unchanged and then decreased.

Thirdly, we investigated the inertial effects on the static and dynamic properties of the suspension over a wide range of volume fraction from 0.01 to 0.4. We found that at Reynolds number $\mathrm{Re} \leq 0.5$, static and dynamic properties showed the typical non-Brownian, Stokes regime characteristics due to insignificant inertial effects. We observed that high inertial forces at Re=1, created a deficiency of neighbouring particles around a test particle and this deficiency is increased with further increase in inertial forces. At Re=1, this deficit is more pronounced in the vertical direction which reduced the velocity fluctuations and the particle diffusion, whereas both of these properties remained unchanged in the horizontal direction due to insignificant structural changes in the horizontal direction. Moreover, at Re=10, strong inertial forces generated a significant deficit of particles in both directions, which decreased both velocity fluctuations and particle diffusion. We also observed that the range of volume fraction affected by inertial forces is increased with the increase of Re. At high volume fraction $\phi \gtrsim 0.15$, intrinsic many-body interactions dominated the phenomena and governed the transport properties thereafter.

Concisely, we explored the effects of thermalized particles, non-Brownian particles and inertial forces on their transport properties during sedimentation. Our finite Pe analysis revealed that at $\mathrm{Pe} \gtrsim 30$ settling particles showed the typical non-Brownian characteristics. We found that transport properties of suspended non-Brownian particles are largely depended on its microstructure at low volume fractions in the Stokes regime, whereas at large volume fractions, many-body interactions governed these properties. In addition, with the increase of inertial forces, which caused a deficit of neighbouring particles around a test particle, we found that microstructure of the suspension governed the transport properties for the longer range of volume fraction, before many-body interactions over-powered the phenomena. Moreover, this dissertation also revealed a clear dependency of velocity fluctuations, their relaxation times and the self-diffusion on the wide range of particle volume fraction, system size and Re. At low volume fraction and in the Stokes regime, velocity fluctuations followed the $\phi^{1/2}$ scaling, plateaued at moderate volume fractions and decayed at high volume fractions, in both directions. The self-diffusion followed the $\phi^{1/2}$ scaling at low volume fractions and decayed sharply at high volume fractions in both directions. In contrast, at moderate volume fractions, the vertical self-diffusion decreased, whereas the horizontal diffusion remained unchanged. We also observed a decrease in the velocity fluctuations and self-diffusion at high Re, due to less number of particles available to interact with a given particle.

Acknowledgements

All praises for ALLAH whose blessings are abundant who guides us in darkness and helps me in all sorts of difficulties.

Carrying out the requisite work and then writing this thesis was, undoubtedly, the most arduous task I have undertaken. However, one of the joys of having completed the thesis is looking back at everyone who has helped me during my PhD.

I would like to begin by thanking my supervisor Prof. Ryoichi Yamamoto. Undoubtedly, it is not an overstatement to say that without the consistent guidance, tutelage, support, unparalleled knowledge, and encouragement of my supervisor, this thesis would never have existed. I would also like to acknowledge the valuable and insightful comments of Prof. Tsuyoshi Koga and Prof. Shuji Matsusaka. I must say a special thank to Dr. John Jairo Molina for whetting my appetite for research and also for going above and beyond to read every line of the manuscript in meticulous detail. Thank you also to my friends Dr. Hideyuki Mizuno and Dr. Takahiro Murashima for piquing my interest in colloidal physics and helping me to understand the basics during my early days in this laboratory. My gratitude to Dr. Takashi Taniguchi and Dr. Hiroyuki Shinto for their useful suggestions and discussions. A very special thank to Saint Francis school and college's principal, my best friend and mentor Syed Saqlain Haider Rizvi for his guidance, unwavering support, love and shouldering me through each and every stage of my life.

I should also like to thank former and present graduate students and laboratory members Mr. Chun-Yu Shih, Mr. Antti Lamberg, Dr. Rei Tatsumi, Dr. Tomonori Fukasawa and Dr. Hideki Kobayashi for providing a wonderful and exciting environment. A very special thank to ever vigilant laboratory secretary Ms. Kana Ishida for taking a very good care of all the official matters.

Above all, I would like to thank particularly my parents Nasim Akhtar and Abdul Hameed, brothers, sisters, in-laws, beloved wife Fatima Tahir and my son Muhammad Shaheer Adnan for their love, encouragement, support, and unwavering belief in me. Without you, I would not be the person I am today. My special gratitude to Mr. Muhammad Zulfiqar Ali and family and Dr. Muhammad Shabbir and family for encouragement, support and all the quality time spent together.

Finally, the work reported in this thesis would not have been possible without the financial support of monthly scholarship and the Global COE Program, "International Center for Integrated Research and Advanced Education in Materials Science" from MEXT, for which I am grateful.

List of Publications

1. Adnan Hamid and Ryoichi Yamamoto, “Anisotropic velocity fluctuations and particle diffusion in sedimentation", *Journal of the Physical Society of Japan*, 2013, **82**, 024004.

2. Adnan Hamid and Ryoichi Yamamoto, “Direct numerical simulations of anisotropic diffusion of spherical particles in sedimentation", *Physical Review E*, 2013, **87**, 022310.

3. Adnan Hamid and Ryoichi Yamamoto, “Sedimentation at finite Peclet number: Direct numerical simulation", *AIP Conference Proceedings*, 2013, **1518**, 444-447.

4. Adnan Hamid, John Jairo Molina and Ryoichi Yamamoto, “Sedimentation of non-Brownian spheres at high volume fractions", *Soft Matter*, 2013, **9**, 10056-10068.

5. Adnan Hamid, John Jairo Molina and Ryoichi Yamamoto, “Simulation studies of microstructure of colloids in sedimentation", *Molecular Simulation*, **accepted**.

6. Adnan Hamid, John Jairo Molina and Ryoichi Yamamoto, “Direct numerical simulations of sedimenting spherical particles at finite Reynolds number”, **submitted**.

Contents

List of Figures

List of Tables

Abbreviations

AF	Anisotropic factor
AR	Archimedes number
DNS	Direct numerical simulations
DKT	Drafting-kissing-tumbling mechanism
HIs	Hydrodynamic interactions
LBM	Lattice Boltzmann method
MSD	Mean-square displacement
NS	Navier Stokes
PDF	Pair distribution function
Pe	Peclet number
PY	Percus-Yevick
RDF	Radial distribution function
Re	Reynolds number
SP	Smooth profile
SRD	Stochastic rotational dynamics
WCA	Weeks-Chandler-Andersen

Symbols

θ	Angular coordinate in cylindrical coordinates
V_{sed}	Average sedimentation velocity
$\varphi \boldsymbol{f}_{\text{p}}$	Body force
k_{B}	Boltzmann constant
$u_{\text{f}}^{r_{\text{cyl}}}(r_{\text{cyl}},z), u_{\text{f}}^{z}(r_{\text{cyl}},z)$	Components of fluid velocity in cylindrical coordinates after the particle
$u_{\text{f}}^{r_{\text{cyl}}}(r_{\text{cyl}},-z), u_{\text{f}}^{z}(r_{\text{cyl}},-z)$	Components of fluid velocity in cylindrical coordinates before the particle
$K(\phi)$	Coefficient that represents the effects of the finite volume fraction
$\Delta \boldsymbol{u}_{\text{f}}^{\text{Re}=\gamma}(r_{\text{cyl}},z)$	Difference in fluid velocity at $\text{Re} = \gamma$ with $\text{Re} = 0.1$
$\Delta \boldsymbol{u}_{\text{f}}^{\text{AB}}(r_{\text{cyl}},z)$	Difference in fluid velocity before and after the particle
$\boldsymbol{F}_i^{\text{c}}$	Direct inter-particle interactions
z	Direction of gravity
x	Direction perpendicular to gravity
r	Distance from the particle
r^x	Distance in x direction
r^y	Distance in y direction
r^z	Distance in z direction
C_D	Drag coefficient
n	Exponent of Richardson Zaki power law
$\boldsymbol{F}_i^{\text{ext}}$	External force
$\boldsymbol{N}_i^{\text{ext}}$	External torque
ρ_{f}	Fluid density
$\boldsymbol{v}_{\text{f}}$	Fluid velocity
$\boldsymbol{u}_{\text{f}}^{\text{Re}=\gamma}(r_{\text{cyl}},z)$	Fluid velocity at at $\text{Re} = \gamma$
$\boldsymbol{u}_{\text{f}}(r_{\text{cyl}},z)$	Fluid velocity in cylindrical coordinates
$\boldsymbol{u}_{\text{f}}^{\text{A}}(r_{\text{cyl}},z)$	Fluid velocity in cylindrical coordinates after the particle

$\boldsymbol{u}_{\mathrm{f}}^{\mathrm{B}}(r_{\mathrm{cyl}}, z)$	Fluid velocity in cylindrical coordinates before the particle
η	Fluid viscosity
g	Gravity
Δ	Grid spacing
D_{H}^{β}	Hydrodynamic diffusion coefficient
$\boldsymbol{F}_i^{\mathrm{H}}$	Hydrodynamic force
$\boldsymbol{N}_i^{\mathrm{H}}$	Hydrodynamic torque
$\Delta V_{\mathrm{H}}^{\beta}$	Hydrodynamic velocity fluctuations
$C_{\beta}(0)$	Initial value of temporal autocorrelation function
r_1, r_2	Integration limits of anisotropic factor
ξ	Interface thickness
M_i	Mass of particle i
$\boldsymbol{I}_i$	Moment of inertia of particle i
n_d	Number density of particles
N	Number of particles
$\boldsymbol{Q}_i$	Orientation matrix
$g(\boldsymbol{r})$	Pair distribution function
$g\left(r_{\mathrm{cyl}}, z\right)$	Pair distribution function in cylindrical coordinates
α^n	Parameter that controls the temperature of the system $(n \in \mathrm{V}, \Omega)$
ρ_{p}	Particle density
σ	Particle diameter
$Q^{\gamma\beta}$	Particle orientation tensor
a	Particle radius
$\boldsymbol{v}_{\mathrm{p}}$	Particle velocity
ϕ	Particle volume fraction
$\boldsymbol{R}_i$	Position of particle i
R_{ix}	Position of particle i in x direction
R_{iz}	Position of particle i in z direction
k	Prefactor of hindered settling function
r_{cyl}	Radial distance in cylindrical coordinates
$g(r)$	Radial distribution function
$\boldsymbol{G}_i^{\mathrm{V}}$	Random force
$\boldsymbol{G}_i^{\Omega}$	Random torque

$\tau_{\mathrm{H}}^{\beta}$	Relaxation time of hydrodynamic velocity fluctuations
$\boldsymbol{\Omega}_i$	Rotational velocity
B_1^{β}	Saturation value of hydrodynamic velocity fluctuations
B_2^{x}	Saturation value of the relaxation time in x direction
A_1^{β}, A_2^{β}	Scaling coefficients
Δr	Shell thickness in RDF
l	Size of hypothetical blob of fluid
$\boldsymbol{\varphi}(\boldsymbol{x})$	Smooth profile function
$\boldsymbol{x}$	Spatial coordinate
$C_{\beta}(\boldsymbol{r})$	Spatial correlation function
t_{s}	Stokes time
V_{s}	Stokes velocity
$\boldsymbol{\sigma}_{\mathrm{f}}$	Stress tensor
S_i	Surface
L	System size
T	Temperature
$C_{\beta}(t)$	Temporal autocorrelation function ($\beta \in x, z$)
t_{t}	Terminal time
V_{t}	Terminal velocity
D_0	Thermal diffusion coefficient at $g = 0$
${D_0}^{\phi=0}$	Thermal diffusion coefficient at $g = 0$ and at infinite dilution
$C_0(t)$	Thermal velocity fluctuations autocorrelation function
t	Time
D_{β}	Total diffusion coefficient
$\boldsymbol{v}$	Total velocity
$\boldsymbol{v}_{xy}$	Total velocity in XY plane
$\boldsymbol{v}_{xz}$	Total velocity in XZ plane
$\boldsymbol{V}_i$	Translational velocity
V_{ix}	Translational velocity in x direction
V_{iz}	Translational velocity in z direction
$\boldsymbol{I}$	Unit tensor
$U_{(r_{ij})}$	Weeks-Chandler-Andersen potential
$\boldsymbol{\varepsilon}$	Weeks-Chandler-Andersen potential's energy unit

r_{ij}	$\mid \boldsymbol{R}_i - \boldsymbol{R}_j \mid$
δV_{iz}	$V_{iz} - V_{\text{sed}}$
$\hat{r}_{ij}^{\beta}$	$\frac{r_i^{\beta} - r_j^{\beta}}{r_{ij}}$
β	$\in x, z$

This dissertation is dedicated to my parents, teachers, friends, wife and my son for their endless and unparalleled prayers, support and encouragements.

Chapter 1

Introduction

1.1 Overview and Motivation

In general, sedimentation is the settling through fluid of suspended material of various sizes, ranging from large rocks to proteins and peptides. The diffusive nature of sedimenting particles in a fluid plays a key role in many chemical industries, such as paper and pulp, paints, water purification, etc., impacting a wide range of processes, like pneumatic and sediment transport, rheological behavior of pastes, fluidized beds, combustion and erosion. Sediments are also a big problem in hydro-power dams and in industrial drainage, from which they must be continuously removed. Along with the other separation techniques, sedimentation is an essential, cheap and widely used clarification process. Typically, the settling of particles is achieved by decreasing the velocity of the fluid such that particles sediment. This apparently simple technique is strongly affected by the host fluid and particle parameters as well as the configuration of the container, which make this phenomena difficult to tackle both experimentally and computationally. Microscopically, it is a typical example of non-equilibrium dynamics, which shows interesting yet perplexing static (time independent) and dynamic (time dependent) properties. Numerous theoretical [1–4], experimental [5–13] and simulation [14–32] studies have been performed to investigate these parameters.

1.2 Brief Literature Survey

The first significant theoretical work on sedimentation was performed by Stokes [33], who calculated the settling velocity of a single particle in an incompressible fluid, in the absence of appreciable inertia, known as the Stokes velocity. This result was used later by Einstein [34] to calculate the diffusivity of an isolated particle undergoing Brownian motion. Later, Batchelor [35] found the effect of particle volume fraction and fluid back flow on the settling velocity

at low volume fractions, based on the assumption of a uniform distribution for the separation of pairs of spheres. This is also known as hindered settling caused by the drag force induced by the fluid back flow and the particle-particle interactions, which make the particle to undergo fluctuating motions. Researchers characterize this fluctuating motion of particles mainly by calculating velocity fluctuations, their relaxations times and particle diffusion. Since these properties are largely dependent on particle and fluid based parameters, along with the size and shape of the container, the accurate measurement of these properties has become immensely important to get a clear and more insightful picture of the physical phenomena.

Unlike particles undergoing Brownian motion, sedimenting particles show different behavior in the direction parallel and perpendicular to gravity. Caflisch and Luke [4] predicted that at infinite particle limit, the velocity fluctuations are infinite by assuming pair wise additivity, which is certainly unphysical. Hinch [36] solved this paradox by considering a hypothetical blob of fluid of size l, having $n_d l^{1/3}$ average number of particles (n_d is the number density of the particles), with $\sqrt{n_d l^{1/3}}$ statistical fluctuations in particle number. If m is the mass of the particles which balance the buoyancy, then the fluctuations in the weight are $mg\sqrt{n_d l^{1/3}}$. Balancing this weight with the drag force, Hinch came up with the scaling of velocity fluctuations as $\sim \sqrt{\phi l/a}$, where ϕ and a denote the particle volume fraction and radius, respectively.

These predictions stimulated many experimental studies [5–11, 37, 38]. Batchelor [37] investigated the bidispersed suspension, where those particles lighter than the fluid rose and those heavier sank. Later, Nicolai performed a series of experiments [5–7] to investigate the effects of particle volume fraction, system size and polydispersity on velocity fluctuations and particle diffusion. These studies quantified the transport properties, but gave little information about the physics. Guazzelli [38] investigated the effects of walls and found that these walls act as kinetic traps and reduce the velocity fluctuations of the particle in the near vicinity. Segre [8–11], in a series of experiments, also investigated the effect of particle volume fraction ϕ on velocity fluctuations at low volume fraction and found that these velocity fluctuations scale as $\phi^{1/3}$, in contrast to the theoretical prediction of Hinch [36] and experimental results of Bernard [13]. This contradiction between the theory and experiments was solved by Brenner [39] through a theoretical investigation, scaling arguments and numerical simulations. He found that vertical walls play a critical role in this scaling. In a large confined box (larger than the correlation length), the velocity field of a particle near the wall decays as r^{-2} or higher depending upon the shape of the wall, whereas in the vertical mid plane of the cell where walls have no effects this velocity field decays as r^{-1}. Due to this large velocity field in the middle plane, the interaction of the velocity field of a particle with other particles is larger than the velocity field of the particle near the walls. This strong interaction of particles in the middle plane will induce larger velocity fluctuations than particles near the walls. Hence, there exists a gradient in the velocity fluctuations, being maximum in the middle plane and the minimum near the walls. This gradient will drift the particles from the center to the wall and cause a depletion of particles in the mid plane. Brenner [39] analysed previous experiments [5, 9] in the context of the above

mentioned phenomena and argued that if we consider the path of a tracked particle (Ref. [5], Figure 1), it shows that some of the particles are close to the side walls. Since these side walls act as kinetic traps, particles spend more time close to the wall, where velocity fluctuations are smallest and relax quickly. He reported that the previous experiments [5,9] had not taken care of the side walls effects and the particles near the side walls should not be used to calculate the velocity fluctuations. He recalculated the velocity fluctuations of Segre's work by considering the particles not affected by the side walls and found the $\phi^{1/2}$ scaling, in good agreement with the theoretical prediction [36]. The side walls have significant effects in the Stokes regime, whereas Koch et al. [40] found a weaker logarithmic scaling when particle inertia is significant. This suggests that bounding solid walls which suppress the velocity fluctuations in the Stokes regime, are relatively less pronounced when inertial forces are significant [40]. The velocity fluctuations lead to randomly fluctuating particle motions, characteristic of a diffusion process, which has been studied first Beenakker [41–43], Ham and Homsy [44] and later Nicolai et al. [5,7] extensively, in a series of experimental studies in the Stokes regime. They found that the self-diffusion coefficients increase at low volume fraction and then decrease sharply at high volume fractions in both parallel and perpendicular to the gravity. This decrease in self-diffusivity at high volume fractions is attributed to the formation of clusters and the fact that the basic mechanism for diffusion is the fluctuating motion of the clusters rather than individual particles. Similar to the velocity fluctuations, diffusion is also strongly dependent on system size. Brenner [39] suggested that the diffusion coefficient should show a $\phi^{1/2}$ dependency at low volume fraction. In addition, the diffusion anisotropy is a key parameter to characterize the nature of the sedimentation phenomena. Nicolai et al. [5] have obtained a quantitatively small decrease in the diffusion anisotropy with volume fraction. Despite the importance of self-diffusion in chemical and biochemical industries, only few studies are attributed to its investigation.

Theories have long predicted that velocity fluctuations diverge with the system size, whereas experiments showed no such dependency. Researchers [9] found that if the system size is less than the blob size then velocity fluctuations diverge with the system, whereas for system sizes larger than the blob size, there is no such divergence. These results were later confirmed by Nguyen and Ladd [20], using the lattice Boltzmann method (LBM). This stimulated the simulation work and with the availability of highly sophisticated computer facilities and fast computational schemes, researchers were able to explore the phenomena at the particle and fluid level, some thing which was not possible in experiments. Ladd [14–18] and Koch [3,40,45,46] pioneered the simulation work on sedimentation, using LBM and explored the effects of particle microstructure, particle and fluid inertia and system size. Koch [1] found that the difference between the vertical and horizontal relaxation times decreases with increasing aspect ratio of the system. He suggested that this difference between the relaxation times originates from the vertical periodic boundary conditions because less time is required for a particle to sample all vertical positions than is required to sample the horizontal positions. The simulations performed

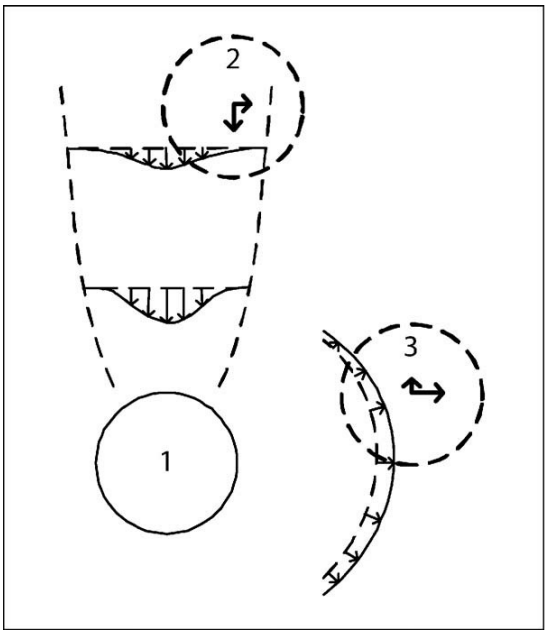

FIGURE 1.1: Schematic representation of drafting-kissing-tumbling (DKT) mechanism. This figure is adapted from Ref. [45].

by Ladd [14] and Padding [23] observed the same phenomena, using vertical periodic boundary conditions. Later, Cunha [24] used direct numerical simulations (DNS) and validated the $\phi^{1/2}$ and $(L/a)^{1/2}$ behavior of velocity fluctuations with respect to volume fraction and system size at low volume fraction, respectively. Cunha also calculated the particle diffusion and its anisotropy and found that diffusion anisotropy remain unchanged at low volume fraction, in good agreement with Padding [23]. In contrast, the 2D simulations of Kuusela [27–31] showed a large change in diffusion anisotropy at high volume fraction. It will be interesting to see how diffusion anisotropy behaves at large volume fraction in 3D. Despite the importance of diffusion in chemical and petroleum industries, only a few studies [5, 47] have focused on diffusion, and in particular at large volume fractions. Recently, Padding [21–23] used stochastic rotation dynamics (SRD) to explore the sedimentation at low Peclet number (Pe), to highlight the relative effects of thermal and hydrodynamic forces on sedimenting particles.

The theoretical aspects of sedimentation phenomena in the Stokes regime are relatively well developed, where velocity fluctuations scale as $\phi^{1/2}$ at low volume fraction [23, 39, 48–51] and as $(L/a)^{1/2}$ with the system size, whereas these properties are not explored extensively at finite Reynolds number (Re), where Re is the ratio of inertial forces to viscous forces. Koch [1, 40, 45] explored the physical aspects of sedimentation at finite Re and found that at low volume fraction and in the Stokes regime, the flow field produced by a settling sphere has a fore-aft symmetry relative to the horizontal plane through its center, which is broken by the fluid inertia at finite Re. This breaking of symmetry generates a wake behind the particle, as shown by the particle 1 in Fig. 1.1, which is adapted from Koch's study [45]. This wake convects fluid towards the rear of the particle and this fluid flux is balanced by the source flow. The trailing particle 2 will

thus drift to the leading particle and it also experiences a lift force due to shear flow in the wake which pushes it outward and cause a particle deficiency in the near vicinity of the particle 1. If this lift force is small then two particle will kiss and then tumble into a horizontal orientation and repel each other due to source flow. This mechanism is known as drafting-kissing-tumbling (DKT) mechanism. Similarly, the horizontally oriented particles like Particle 3 will repel each other due to source flow, which will also induce the deficiency of particles. At high volume fractions, this weak interaction competes with the many-body interactions, which then lead to the isotropic microstructure, similar to that in hard-sphere distribution. Climent et al. [52] observed a similar mechanism in their study.
Under sedimentation, the microstructure of the suspension is determined by the long-range hydrodynamic interaction (HIs), which are characterized by large time and length scales, features that render the non-equilibrium properties of the colloidal particles challenging to tackle both experimentally and by simulations. Despite the fact that experiments can use large system sizes, the statistical variations and the many non-ideal conditions, such as secondary flow, instability caused by the techniques used to track the particles, and polydispersity limited the experiments to the Stokes regime, low volume fraction and to non-Brownian particles. Although, simulations complement the experimental results and help to understand the physics behind the phenomenological changes, it also has its own shortcomings like finite system size and numerical errors.

1.3 Open Problems and Work Plan

Despite the extensive work on sedimentation as briefly reviewed above, there are still some open problems which are needed to be investigated, e.g.:

- Characterization of correlation length and finite size effects.
- Interplay of thermal and hydrodynamic forces especially at high Pe.
- Particle and fluid inertial effects on transport properties.
- System size and shape effects.
- Effects of particle polydispersity and shape.
- Evolution of particle microstructure with inertial forces and its effects on transport properties.

We planned this work to find the answers to some of the above mentioned open problems by DNS, using the smoothed profile (SP) method [53–58], which replaces the original sharp boundaries between the particle and the host fluid with a diffuse interface of finite thickness. This

approach enabled us to use a fixed Cartesian grid, thereby significantly improving the speed of the numerical computations. A similar smoothed profile [59] was adopted in the previously proposed fluid-particle dynamics method in which particles are modelled by a highly viscous fluid. This large viscosity in turn requires small time increment. While, we treated particles as non-deformable solids such that no additional constraints arose for time increment. On the basis of the above mentioned open problems in sedimentation, we focused on three aspects of sedimentation.

- Sedimentation at finite Peclet number: In this part, we investigated the interplay between the thermal and hydrodynamic forces, by changing the Pe and studied its effects on the transport properties of the suspension. Previously, Padding [23] investigated the finite Pe effect, but mainly at Pe ≤ 12, whereas we performed simulations at Pe $\lesssim 120$ and found that at Pe $\gtrsim 30$ hydrodynamic forces completely dominate the sedimentation phenomena. The details of this investigation are presented in Chapter 2.

- Sedimentation of non-Brownian particles: In this part, we focused on the effects of hydrodynamic forces on particles in the Stokes regime. Most of the previous studies [9, 13, 24, 39] focused on non-Brownian particles are at low ϕ, except Nicolai's work [5], which was performed at $\phi \leq 0.4$, but these studies were unable to give a clear dependence of the transport properties on volume fraction and microstructure. In this investigation, we studied the evolution of particle microstructure with the increase of volume fraction and its effects on particle properties. Furthermore, this study also provided a clear picture of the dependence of transport properties on low, moderate (cross-over) and high volume fraction regimes. The details of this investigation are presented in Chapter 3.

- Sedimentation at finite Reynolds number: In this part, we studied the effects of particle inertia on microstructure, velocity fluctuations, their relaxation time and diffusion coefficient. It is very difficult to perform experiments and simulations at high Re due to fast phenomenological changes. Koch [1, 3, 40, 45] performed LBM simulations to investigate the microstructure changes with the increase in Re and its effects on transport properties at four different volume fractions and system sizes. We tried to evaluate both the static and the dynamic properties as a function of Re for $0.01 \leq \phi \leq 0.4$. This study also gave a clear picture of Re effects on low, moderate and high volume fraction regimes. The details of this investigation are presented in Chapter 4.

In brief, this dissertation consists of simulation studies of mono-dispersed spherical particles settling in an incompressible fluid. We explored the phenomena ranging from low Pe and low Re to the finite Re and high Pe, giving rise to the interplay of thermal and hydrodynamic forces (finite Pe and low Re), complete dominance of hydrodynamic forces (high Pe and low Re) and

unignorable inertial forces (high Pe, finite Re). This study not only quantifies the transport properties of the suspension, it also gives a better understanding of the phenomenological changes based on a particle microstructure analysis.

1.4 Simulation Method

In the SP method, the boundary between the colloidal particle and the host fluid is replaced with a continuous interface by assuming a smoothed profile [60], having thickness equal or larger than the grid spacing Δ, as shown in Fig. 1.2. This simple modification enabled us to accurately characterize the hydrodynamic interactions, without neglecting many-body interactions. In this section, we briefly explain the salient features of our method.

In this method, the colloid's density profile is defined such that it changes smoothly within the interface. Quantities such as the velocity and pressure are defined over the entire computational domain, which includes the colloid as well as the solvent. We enforced the total field velocity zero condition, i.e., $\int d\boldsymbol{r}\boldsymbol{v}(\boldsymbol{r}) = 0$, which guarantees that the sedimentation velocity is the same as the superficial velocity.

The motion of the ith colloidal particle is obtained by solving Newton and Euler's equations of motion for a given particle position $\boldsymbol{R}_i$, translational velocity $\boldsymbol{V}_i$ and rotational velocity $\boldsymbol{\Omega}_i$:

$$M_i\dot{\boldsymbol{V}}_i = \boldsymbol{F}_i^{\mathrm{H}} + \boldsymbol{F}_i^{\mathrm{c}} + \boldsymbol{F}_i^{\mathrm{ext}} + \boldsymbol{G}_i^{\mathrm{V}}, \quad \dot{\boldsymbol{R}}_i = \boldsymbol{V}_i, \tag{1.1}$$

$$\boldsymbol{I}_i \cdot \dot{\boldsymbol{\Omega}}_i = \boldsymbol{N}_i^{\mathrm{H}} + \boldsymbol{N}_i^{\mathrm{ext}} + \boldsymbol{G}_i^{\Omega}, \quad \dot{\boldsymbol{Q}}_i = \mathrm{skew}(\boldsymbol{\Omega}_i) \cdot \boldsymbol{Q}_i, \tag{1.2}$$

where

$$\mathrm{skew}(\boldsymbol{\Omega}) = \begin{pmatrix} 0 & -\Omega^3 & \Omega^2 \\ \Omega^3 & 0 & -\Omega^1 \\ -\Omega^2 & \Omega^1 & 0 \end{pmatrix} \tag{1.3}$$

Mass and moment of inertia are denoted as M_i and $\boldsymbol{I}_i$, respectively, and $\boldsymbol{Q}_i$ is the orientation matrix. The hydrodynamic torque and force exerted by the solvent on the particle are represented as $\boldsymbol{N}_i^{\mathrm{H}}$ and $\boldsymbol{F}_i^{\mathrm{H}}$, respectively. $\boldsymbol{F}_i^{\mathrm{ext}}$ and $\boldsymbol{N}_i^{\mathrm{ext}}$ are the external force and torque, respectively. $\boldsymbol{G}_i^{\mathrm{V}}$ and $\boldsymbol{G}_i^{\Omega}$ are the random force and torque due to thermal fluctuations, which can be described as $\langle \boldsymbol{G}_i^n(t)\boldsymbol{G}_j^n(0)\rangle = \alpha^n \boldsymbol{I}\delta(t)\delta_{ij}$, where $\langle \boldsymbol{G}_i^n(t)\rangle = 0$ and α^n ($n \in \mathrm{V}, \Omega$) is the parameter that controls the temperature of the system T. The actual value of the particle temperature is determined using the long-time diffusion coefficient of the equilibrium system at infinite dilution ${D_0}^{\phi=0}$ by Stokes-Einstein equation, $k_{\mathrm{B}}T = 6\pi\eta a {D_0}^{\phi=0}$. When simulating a Brownian particle using HIs, the diffusion coefficient is affected by the finite size effects (i.e., artefacts arise when the system size is smaller than the correlation length). These effects can be accounted for by ${D_0}^{\phi=0} = D_0 K(\phi)$, in which D_0 is the thermal diffusion coefficient of Brownian particles obtained for $\phi \neq 0$ and $K(\phi)$ is the coefficient that represents the effects of the finite volume fraction of

dispersed particles under periodic boundary conditions and its values for the given system size and volume fraction is available in the literature [61]. For the given terminal velocity V_t of a single sedimenting particle, which is same as the Stokes velocity in creeping flow conditions (Stokes regime), Brownian motion of the particles can be characterized by using the Peclet number as, $\mathrm{Pe} = aV_t/D_0$, which measures the ratio of convection transport to diffusion transport due to Brownian motion [62]. The detailed implementation of Brownian motion in some test cases is presented by Iwashita et al. [63].

Direct inter-particle interactions are denoted by $\boldsymbol{F}_i^c$ and we represent these interactions using the following Weeks-Chandler-Andersen (WCA) type potential [64],

$$U(r_{ij}) = \begin{cases} 4\varepsilon\left[\left(\frac{\sigma}{r_{ij}}\right)^{24} - \left(\frac{\sigma}{r_{ij}}\right)^{12}\right] + \varepsilon & \left(r_{ij} \leq 2^{\frac{1}{12}}\sigma\right), \\ 0 & \left(r_{ij} > 2^{\frac{1}{12}}\sigma\right), \end{cases} \tag{1.4}$$

where $r_{ij} = \mid \boldsymbol{R}_i - \boldsymbol{R}_j \mid$. The parameters $\sigma = 2a$ and $\varepsilon = 2.5$ denote the length and energy units, respectively.

In the SP method, the fluid motion is obtained by solving the incompressible Navier-Stokes (NS) equation for a given value of fluid viscosity η and density ρ_f:

$$(\partial_t + \boldsymbol{v}_f \cdot \nabla)\boldsymbol{v}_f = \rho_f^{-1}\nabla \cdot (-p\boldsymbol{I} + \boldsymbol{\sigma}_f) \tag{1.5}$$

$$\nabla \cdot \boldsymbol{v}_f = 0 \tag{1.6}$$

for the stress tensor $\boldsymbol{\sigma}_f$, fluid velocity $\boldsymbol{v}_f$ and pressure field p, under the incompressibility condition ($\boldsymbol{\nabla} \cdot \boldsymbol{v}_f = 0$). The center-of-mass of the suspension is kept constant to avoid an indefinite acceleration of the system. We would also like to comment that we have not included the lubrication force explicitly, as done in the Stokesian dynamics, but we are still able to reproduce the many particle dynamics convincingly. More details about the lubrication force can be found in previous publications [60, 65]. For given values of η and ρ_f, the remaining units of mass, time, pressure and energy are respectively defined as $\rho_f\Delta^3$, $\rho_f\Delta^2/\eta$, $\eta^2/\rho_f\Delta^2$ and $\eta^2\Delta/\rho_f$. Reynolds number, which measures the relative effects of inertial and viscous forces is defined as, $\mathrm{Re} = \rho_f V_t \sigma/\eta$ [66]. The hydrodynamic force $\boldsymbol{F}_i^H$ and torque $\boldsymbol{N}_i^H$ acting on a particle can be obtained by integrating the stress tensor over the surface as,

$$\boldsymbol{F}_i^H = \int_{S_i} \boldsymbol{\sigma}_f \cdot d\boldsymbol{S_i}, \tag{1.7}$$

$$\boldsymbol{N}_i^H = \int_{S_i} r_i \times (\boldsymbol{\sigma}_f \cdot d\boldsymbol{S_i}). \tag{1.8}$$

The basic idea of the SP method is to solve the modified NS equation over the entire domain, by treating the colloids as fluid particles, where particles are represented using a smooth phase

field $0 \leq \varphi(\boldsymbol{x},t) \leq 1$, which removes the troublesome boundary conditions at the particle surface. Here $\varphi = 0$ stands for the fluid, $0 < \varphi < 1$ describes the interface and $\varphi = 1$ the particle domain. The rigidity of the particles can be maintained by introducing a body force $\varphi \boldsymbol{f}_\mathrm{p}$ in the NS equation, which is computed assuming momentum conservation between the fluid and the particles.

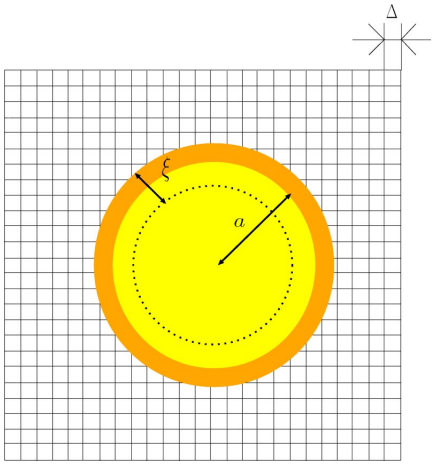

FIGURE 1.2: Schematic representation of the diffuse particle interface, where ξ shows the thickness of interface.

$$(\partial_t + \boldsymbol{v}\cdot\nabla)\,\boldsymbol{v} = \rho_\mathrm{f}^{-1}\nabla\cdot(-p\boldsymbol{I} + \boldsymbol{\sigma}_\mathrm{f}) + \varphi\boldsymbol{f}_\mathrm{p} \tag{1.9}$$

$$\boldsymbol{v} = (1-\varphi)\boldsymbol{v}_\mathrm{f} + \varphi\boldsymbol{v}_\mathrm{p} \tag{1.10}$$

$$\varphi\boldsymbol{v}_\mathrm{p} = \sum_i \varphi_i\,[\boldsymbol{V}_i + \boldsymbol{\Omega}_i \times \boldsymbol{r}_i] \tag{1.11}$$

The detailed formulas, algorithm and applicability of the SP method with numerous test cases can be found in previous publications [53–58, 60, 63, 65, 67–78]. Recently, SP method has also been extended to self-propelled swimmers [79], assemblies of spheres [80] and compressible fluid [81–83].

A rigorous study [84] by Luo et al. revealed that compared to a high resolution DNS [85] based on high-order spectral/*hp* element discretization on hybrid grids, the SP method is computationally less expensive and advantageous for simulating moving particles because it avoids the complex discretizations around the particles. This study simulated many test cases and found that the SP method is accurately resolving the lubrication force and far and near field flows. In addition, the computational cost for this method depends upon the number of grid points (system size), however it is insensitive to the number of particles. This enabled us to study dense colloidal dispersion, which is difficult to do with other methods.

Chapter 2

Sedimentation at Finite Peclet Number

2.1 Introduction

Sedimentation at finite Peclet number (Pe) describes the relative effects of thermal fluctuations and hydrodynamic fluctuations. Unlike most previous studies [5, 9, 14, 24, 25, 86], which were performed in a non-Brownian regime (Pe $\rightarrow \infty$), we focused our work at finite Pe defined as $\mathrm{Pe} = aV_s/D_0$, in which $V_s = \frac{2}{9}ga^2(\rho_p - \rho_f)/\eta$ represents the Stokes velocity, at different volume fractions and system sizes. Padding et al. [21–23] were the first to simulate sedimentation at a finite Pe, using coarse-grained SRD simulations. The simplified dynamics allowed accurate calculation of the transport properties; however, due to its stochastic nature, SRD is less effective for large Pe. In SRD, the highest achievable Pe is limited by the constraints on the Mach and Reynolds numbers (Re), whereas no such constraints exist for the SP method. Consequently, a wide range of Pe is achievable using our method. Padding [21–23] focused his work in the low volume fraction regime. The present work not only validates the work of Padding at low volume fraction but also explores the effects of moderate volume fractions on static and dynamic properties of the suspension.

The main objective of the present study is to investigate the relative effects of thermal and hydrodynamic forces on velocity fluctuations and particle diffusion for different volume fractions.This Chapter provides new insights into the relative effects of thermal and hydrodynamic forces on the particle microstructure and anisotropic behavior of the velocity fluctuations and diffusion. Moreover, we suggest scaling relations of the velocity fluctuations, their relaxation times and self-diffusion for a moderate volume fraction regime. In this Chapter, Section 2.2 describes the selection of the working parameters, results are provided in Section 2.3 and we present conclusions based on our work in Section 2.4.

2.2 Simulation Parameters

Simulations were performed under periodic boundary conditions with a volume fraction ranging from 0.01 to 0.12. In the present study, we divide the range of volume fractions into a low volume fraction regime defined as $\phi \lesssim 0.04$ and a moderate volume fraction regime defined as $0.04 < \phi \lesssim 0.12$. This division helps to explain the scaling of the hydrodynamic velocity fluctuations and the self-diffusion in an effective way, which will be evident later. Three different cubic periodic boxes of dimensions $L/a = 16$, 32 and 64 were used and the particle size was held constant at 4Δ for all simulations. The thermal fluctuations $k_{\mathrm{B}}T$ were maintained at ~ 0.3, and the ε of the WCA potential was set at 2.5.

In this study, the range of Pe is achieved by increasing the value of gravity, which is introduced in the $-z$ direction. The increase in gravity also increases the Reynolds number, $\mathrm{Re} = \rho_{\mathrm{f}}\sigma V_{\mathrm{s}}/\eta$ from 10^{-3} to 0.3, which is still low enough to ignore the inertial effects and remains within the Stokes regime. In contrast to the simulations studies [23, 24], most of the experiments [5, 9, 87] have been performed at low Re values, usually of the order of 10^{-5} or less. Because a relative deviation from the Stokes regime scales with the square of Re, we can probe relatively high Re values without straying from the relevant experimental conditions. In addition, maintaining such a low value of Re is computationally more expensive. For a given initial configuration, particles require a certain time to acquire their steady-state velocities. We monitored the data, and only that corresponding to the steady-state velocities is used. The simulations are run upto $500t_{\mathrm{s}}$ for $\mathrm{Pe} = 0.7$ and to $1200t_{\mathrm{s}}$ for $\mathrm{Pe} > 50$; sufficient to yield statistically meaningful data for the analysis in which t_{s} denotes the Stokes time ($t_{\mathrm{s}} = a/V_{\mathrm{s}}$).

2.3 Results and Discussion

2.3.1 Microstructure

One can expect HIs to play a dominant role at higher Pe values, thereby leading to changes in the microstructure. The additional hindrance caused by these HIs changes the microstructure of the system. A quantitative measure of the microstructure at the particle scale is provided by the pair distribution function (PDF),

$$g(\boldsymbol{r}) = \frac{2L^3}{N^2}\left\langle \sum_{i<j} \delta\left(\boldsymbol{r} - \boldsymbol{r}_{ij}\right) \right\rangle, \tag{2.1}$$

in which N is the total number of particles, $\boldsymbol{r} = (r^x, r^y, r^z)$ with r^x, r^y and r^z the components in each direction, $\boldsymbol{r}_{ij} = \boldsymbol{R}_i - \boldsymbol{R}_j$, $\langle \ldots \rangle$ denotes an ensemble average, and the summation $\sum_{i<j}$ is taken over all particle pairs. The definition of $g(r)$ is such that $4\pi\rho g(r) r^2 \Delta r$ represents the mean

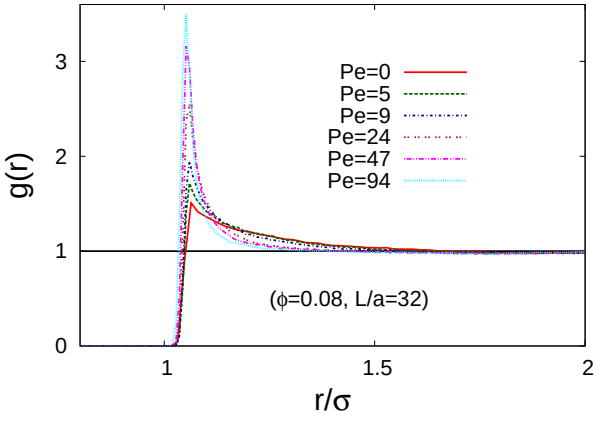

FIGURE 2.1: Radial distribution function $g(r)$ for different Pe values. Simulations are performed in a cubic periodic box of length $L/a = 32$ with a particle size of $a = 4$, keeping ϕ and $k_B T$ constant at ≈ 0.08 and 0.3, respectively.

number of particles in a shell of radius r and thickness Δr that surrounds a particle at the origin [88]. Figure 2.1 shows the spherically averaged PDF which is known as radial distribution function (RDF) $g(r)$ for different Pe values for a system of size $L/a = 32$ and $\phi = 0.08$. The peak of the function increases with increasing Pe, demonstrating the formation of aggregates or particle clusters in close contact. This clustering is induced by the dominance of hydrodynamic forces with increasing Pe, which in turn progressively reduces the effects of thermal fluctuations. A similar phenomena has also been observed by Brady et al. [89] in their investigation of the relative effects of thermal and shear forces. They reduced the effects of thermal fluctuations by increasing the shear rate and observed a similar cluster formation. Apart from the initial peak, the results are indistinguishable from the equilibrium results for Pe ≤ 9, demonstrating the strong effects of the thermal fluctuations. For Pe > 9, these results are differentiable, providing evidence that the HIs exert a progressively dominating effect. A relatively large change in the RDF at Pe ≥ 24 indicates that the HIs overpower the sedimentation phenomena. Moreover, the peak of $g(r)$ at Pe $= 0$ is higher than the peak value provided by the well-known exact solution [90] of the Percus-Yevick (PY) integral equation for the RDF. In our results, this discrepancy arises from an overlapping of the smoothed profiles of two particles in close contact. Similar discrepancies are also reported in the literature [23].

The $g(r)$ gives useful information for an isotropic suspension, whereas in an anisotropic suspension like sedimentation under gravity, we need to determine whether particles prefer to position themselves in a particular direction with respect to a neighbouring particle. In order to investigate this preference, we compute the pair distribution function $g\left(r_{\text{cyl}}, z\right)$ in cylindrical coordinates averaged over the angular coordinate θ in Fig. 2.2, where $\theta = \arctan\left(r^y/r^x\right)$, $r_{\text{cyl}} = \sqrt{\left(r^x\right)^2 + \left(r^y\right)^2}$, $z = r^z$ is the height and lines are drawn at σ, $\sqrt{2}\sigma$, $\sqrt{3}\sigma$ and 2σ to visualize the long range ordering. These density maps clearly show the evolution of particle configuration with respect to the neighbouring particle, as a function of Pe. At low Pe, an isotropic

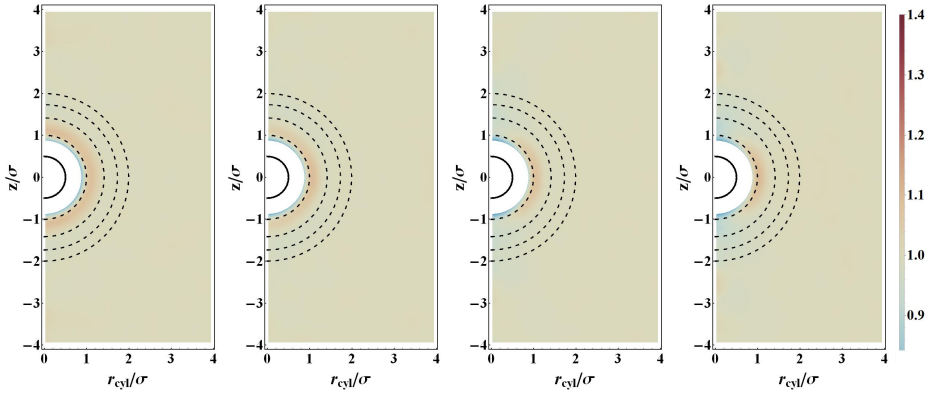

(a) $Pe = 0$ (b) $Pe = 9$ (c) $Pe = 31$ (d) $Pe = 113$

FIGURE 2.2: Pair distribution function of particles in cylindrical coordinates ($g\left(r_{\mathrm{cyl}}, z\right)$) for a system size $L/a = 32$ and $\phi = 0.1$.

microstructure is evident, which shows the dominance of thermal fluctuations. At Pe $\gtrsim$ 30, anisotropic microstructure is evident which shows the dominance of hydrodynamic interactions. This anisotropic microstructure is caused by the drafting-kissing-tumbling mechanism, as explained by Koch [40].

2.3.2 Hydrodynamic Velocity Fluctuations and their Scaling

One of the main objectives of the current study is to develop a scaling for the hydrodynamic velocity fluctuations and their relaxation times, which are two of the key parameters for diffusion in sedimentation. To establish a scaling relationship that accounts for the effects of system size, volume fraction and thermal fluctuations on the hydrodynamic velocity fluctuations, we calculate the temporal autocorrelation functions of the velocity fluctuations as follows:

$$C_x(t) = \left\langle V_{ix}(t)\, V_{ix}(0) \right\rangle \tag{2.2}$$

and

$$C_z(t) = \left\langle \delta V_{iz}(t)\, \delta V_{iz}(0) \right\rangle, \tag{2.3}$$

in which $\delta V_{iz} = V_{iz} - V_{\mathrm{sed}}$, V_{iz} and V_{ix} are the temporal velocities of the ith particle in the z and x direction, respectively, and $V_{\mathrm{sed}} = \langle V_{iz} \rangle$ is the mean settling velocity of the particles.

Figure 2.3 shows the time decay of the correlation functions for the z and x components of the velocity fluctuations at $\phi = 0.04$ and $L/a = 32$. The main plots in Fig. 2.3 use the initial fluctuations $C_z(0)$ and $C_x(0)$ as normalization constants to visualize the relaxation of the velocity fluctuations, whereas the figure insets use the square of the Stokes velocity to normalize the correlations, highlighting the effects of the non-equilibrium hydrodynamic fluctuations. Time is

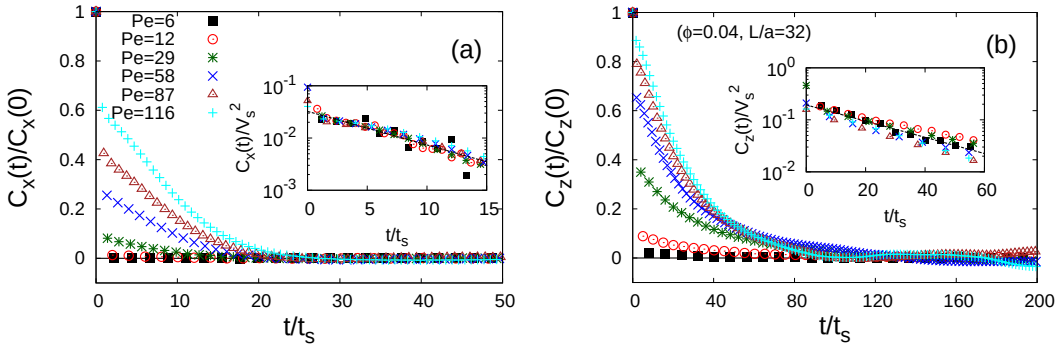

FIGURE 2.3: Temporal autocorrelation functions of the vertical $(C_z(t))$ and horizontal $(C_x(t))$ velocity fluctuations. The main plots show the correlation functions normalized by the initial fluctuations, whereas the temporal correlation functions shown in the insets are normalized by the square of the Stokes velocity on a semi-log scale. The insets also indicate that at large values of Pe, these correlation functions relax exponentially according to $C_\beta(t) = \left(\Delta V_{\rm H}^\beta\right)^2 \exp(-t/\tau_{\rm H}^\beta)$ as shown by the dotted lines in which $\Delta V_{\rm H}^\beta$ $(\beta \in x,z)$ and $\tau_{\rm H}^\beta$ denote the amplitude and the relaxation time of the hydrodynamic velocity fluctuations, respectively. Time is normalized by the Stokes time as $t_{\rm s} = a/V_{\rm s}$.

normalized by the Stokes time $t_{\rm s}$ such that $t_{\rm s} = a/V_{\rm s}$.

The main plots in Figs. 2.3(a) and (b) indicate the large difference in relaxation times for the vertical and horizontal correlations, whereas the experiments [5] show a small difference in these time scales. This difference in time scales can be reduced by increasing the aspect ratio of the periodic box or by increasing the volume fraction of the particles, as observed in other studies [3, 14, 23].

At low Pe, the strong effects of the thermal fluctuations cause a rapid decay in the correlations, whereas at higher Pe, an exponential decay is evident, as shown in Fig. 2.3. In an experimental study, Nicolai et al. [5] observed an exponential relaxation of the temporal correlations of velocity fluctuations of the form: $C_\beta(t) = \left(\Delta V_{\rm H}^\beta\right)^2 \exp(-t/\tau_{\rm H}^\beta)$ in which $\Delta V_{\rm H}^\beta$ $(\beta \in x,z)$ and $\tau_{\rm H}^\beta$ denote the amplitude and relaxation time of the hydrodynamic velocity fluctuations, respectively. The present DNS results support the following forms for the autocorrelations of the velocity fluctuations as the simulations are performed at finite Pe:

$$C_x(t) = C_0(t) + (\Delta V_{\rm H}^x)^2 \exp(-t/\tau_{\rm H}^x), \tag{2.4}$$

$$C_z(t) = C_0(t) + (\Delta V_{\rm H}^z)^2 \exp(-t/\tau_{\rm H}^z), \tag{2.5}$$

in which $C_0(t)$ represents the velocity autocorrelation function in the presence of thermal fluctuations but without gravity, which becomes negligible at higher Pe. These equations represent the summation of the pure thermal and hydrodynamic forces; the former is dominant at low Pe, and the latter plays a key role at high Pe. In addition to these two Pe regimes, a transition regime is also expected to exist in which neither of these two forces is dominant. Hence, the

scaling relations for the diffusion coefficients based on Eqs. (2.4) and (2.5) should deviate from the simulation results in this transition regime, which will be tested later.

At finite Pe, the velocity fluctuations consist of a thermal and a hydrodynamic component. The dominant role of the hydrodynamic fluctuations at higher Pe causes the correlation functions to fall on the same curve when scaled with the square of the Stokes velocity, as shown in Fig. 2.3 insets. Our data shows a good agreement with the fitted curves.

We obtained the values of $\Delta V_{\mathrm{H}}^{\beta}$ and $\tau_{\mathrm{H}}^{\beta}$ at different volume fractions and system sizes from the exponential fits. These values are plotted in Fig. 2.4 for three different system sizes. Hinch [36] proposed scaling relationships for the hydrodynamic velocity fluctuations and their relaxation times, as discussed in Chapter 1. Cunha et al. [24] explained this scaling by hypothetically dividing the simulation box into two equal parts. The imbalance in the particle weight caused by variations in the particle number in both parts is balanced by the Stokes drag. They predicted the scaling relations as $\Delta V_{\mathrm{H}}^{\beta}/V_{\mathrm{s}} = \sqrt{A_1^{\beta} L\phi/a}$ and $\tau_{\mathrm{H}}^{\beta}/t_{\mathrm{s}} = A_2^{\beta}\sqrt{L/(\phi a)}$ in which A_1^{β} and A_2^{β} are constants that depend on the system parameters (e.g., the container shape, swirl size, particle shape and polydispersity). This simple scaling is expected to work well for low volume fractions.

The pre-factors A_1^{β} and A_2^{β} are obtained by fitting the scaling relationships to the simulation data, as shown in Fig. 2.4, which shows the scaling of the hydrodynamic velocity fluctuations and their relaxation times as a function of the volume fraction for three different system sizes, in both directions. Our simulation results are in good agreement with the scaling relations in the low volume fraction regime, but deviations are evident in the moderate volume fraction, for all system sizes. Figure 2.4 also depicts that, for a given system size, $\Delta V_{\mathrm{H}}^{\beta}$ and τ_{H}^{x} reach a saturation value at moderate volume fractions, whereas τ_{H}^{z} continues to follow the scaling relation. The simulations of Padding et al. [23] and Cunha et al. [24] and the rationalized results [39] (considering the side wall effects) of Segre et al. [9] also demonstrated the similar scaling at low volume fractions. Cunha showed the transition from $\phi^{1/2}$, but unfortunately the scaling was unclear at high volume fraction. In contrast, Brenner [39] theoretically proposed the transition from $\phi^{1/2}$ to $\phi^{1/3}$, which has not been confirmed by any other simulation or experimental studies.

The velocity fluctuations and their relaxation times in both directions scale as $(L/a)^{1/2}$ for the full range of volume fractions studied, indicating that our simulations are in a spatially correlated regime. The relevant scaling effects induced by the size dependence of this finite system are discussed in detail in Section 2.3.4. The summary of the scaling is presented in Table 2.1. These new findings at moderate volume fraction lead us to split the scaling relationships into two: one for low volume fractions ($\phi \lesssim 0.04$), similar to that observed in other studies [23, 24, 39], and a second for moderate volume fractions ($0.04 < \phi \lesssim 0.12$), as shown in the Eqs. (2.6)-(2.8):

$$\Delta V_{\mathrm{H}}^{\beta}/V_{\mathrm{s}} = \begin{cases} \sqrt{A_1^{\beta} L\phi/a}, & (\phi \lesssim 0.04) \\ \sqrt{A_1^{\beta} B_1^{\beta} L/a}, & (0.04 < \phi \lesssim 0.12) \end{cases} \tag{2.6}$$

Scaling of $\Delta V_H^\beta/V_s$ and τ_H^β/t_s

	Low ϕ ($\phi \lesssim 0.04$)	Moderate ϕ ($0.04 < \phi \lesssim 0.12$)
$\Delta V_H^x/V_s$	$\sim \phi^{1/2}$	$\sim \phi^0$
$\Delta V_H^z/V_s$	$\sim \phi^{1/2}$	$\sim \phi^0$
τ_H^x/t_s	$\sim \phi^{-1/2}$	$\sim \phi^0$
τ_H^z/t_s	$\sim \phi^{-1/2}$	$\sim \phi^{-1/2}$

TABLE 2.1: Summary of the scaling obtained for the hydrodynamic velocity fluctuations ($\Delta V_H^\beta/V_s$) and their relaxation times (τ_H^β/t_s) in both the vertical and horizontal directions. In addition to the above scaling, both $\Delta V_H^\beta/V_s$ and τ_H^β/t_s are scaled as $(L/a)^{1/2}$ with system size in the low to moderate volume fraction regimes.

$$\tau_H^x/t_s = \begin{cases} A_2^x\sqrt{L/(\phi a)}, & (\phi \lesssim 0.04) \\ A_2^x\sqrt{L/(B_2^x a)} & (0.04 < \phi \lesssim 0.12) \end{cases}, \tag{2.7}$$

and

$$\tau_H^z/t_s = \left\{ A_2^z\sqrt{L/(\phi a)}, \quad (\phi \lesssim 0.12)\right., \tag{2.8}$$

in which B_1^β provides the saturation value of the hydrodynamic velocity fluctuations with respect to the volume fraction in both the x and z directions at moderate volume fractions. Furthermore, B_2^x is the saturation value of the relaxation time in the x direction only, as vertical relaxation times obey the corresponding scaling for the full range of volume fractions, as evident in Eqs. (2.7) and (2.8). Similar phenomena have been observed by Ladd [14] in a simulation study in which no change was found in the horizontal relaxation time at $\phi = 0.05$ and $\phi = 0.25$, but the vertical relaxation time decreased at these volume fractions. In the same study, Ladd also reported a saturation of the vertical relaxation times at high volume fractions ($\phi \geq 0.45$). In an experimental study, Bernard et al. [13] explored the dependency of the relaxation time on the volume fraction and system size and determined that the relaxation time scaled as $(L/a)^{0.65\pm0.1}$, in agreement with the $(L/a)^{0.5}$ scaling observed in this study. Unlike the present study, Bernard found no systematic dependency of the relaxation time on the volume fraction.

The different scaling of the vertical and horizontal relaxation times at moderate volume fractions leads to a decrease in the difference between the vertical and horizontal relaxation times with increasing volume fraction as shown in Fig. 2.5. This finding is important because it aids in characterizing the anisotropic nature of diffusion. Further discussion on the effect of this decrease is presented in Section 2.3.3. Our data show good consistency with the scaling Eqs. (2.6)-(2.8). The pre-factors A_1^β and A_2^β are determined from the fits to be $A_1^z \approx 0.151$, $A_2^z \approx 0.9857$, $A_1^x \approx 0.0253$ and $A_2^x \approx 0.239$ at low volume fractions. For moderate volume fractions, we extracted the values of B_1^β and B_2^x by fitting the new scaling relationships and obtained $B_1^z = 0.037$,

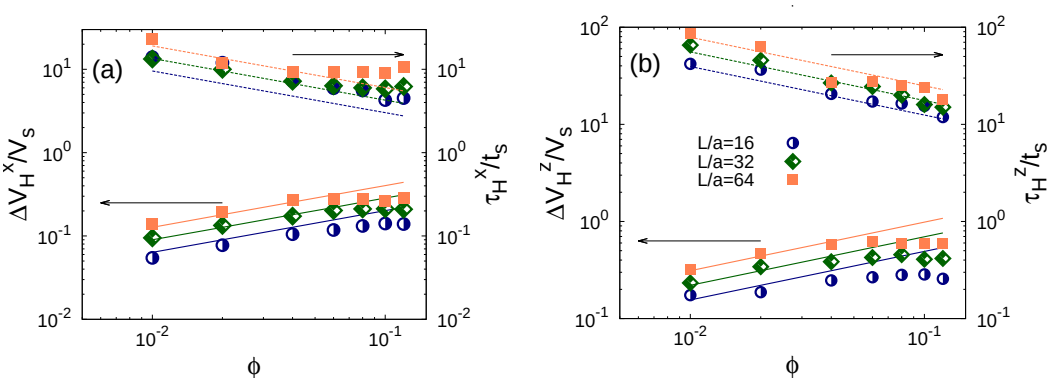

FIGURE 2.4: Scaling of the hydrodynamic velocity fluctuations (left scale) and their relaxation times (right scale) as functions of the volume fraction using three different system sizes, $L/a =$ 16, 32 and 64. The solid lines indicate a scaling to $\Delta V_{\mathrm{H}}^{\beta}/V_{\mathrm{s}}$ of the form $\sqrt{A_1^{\beta} L\phi/a}$, whereas the dashed lines indicate a scaling to $\tau_{\mathrm{H}}^{\beta}/t_{\mathrm{s}}$ of the form $A_2^{\beta}\sqrt{L/(\phi a)}$. The simulation results are represented by points. The symbols and lines are color coded with respect to the system size.

Scaling Coefficients	Values
A_1^x	0.0253
A_2^x	0.239
A_1^z	0.151
A_2^z	0.9857
B_1^x	0.0514
B_1^z	0.037
B_2^x	0.0526

TABLE 2.2: A quantitative comparison of the fitting coefficients obtained by fitting Eqs. (2.6)-(2.8) onto the simulation data. The difference between the x-direction and z-direction coefficients indicates the anisotropic nature of the phenomena.

$B_1^x = 0.0514$ and $B_2^x = 0.0526$. The values of these fitting coefficients are also summarized in Table 2.2. The differences in the vertical and horizontal pre-factors indicate the anisotropic behavior of the velocity fluctuations, with vertical fluctuations larger than the horizontal ones. This anisotropy in the velocity fluctuations varies from 2.5 to 4 in the simulations [14,18,24,26]. The experiments [5,9] have provided a value of ≈ 2.5. Notably, the ratio of the vertical to horizontal hydrodynamic velocity fluctuations in this study is $\Delta V_{\mathrm{H}}{}^{z}/\Delta V_{\mathrm{H}}{}^{x} \approx 2.44$ at low volume fractions, and 2.07 at moderate volume fractions, which are in good agreement with the experimental [5,9] and simulation [26] results. This anisotropic behavior in the velocity fluctuations is believed to be due to the asymmetry of the system induced by the gravity, which caused the larger velocity fluctuations in the direction of gravity than the perpendicular direction .

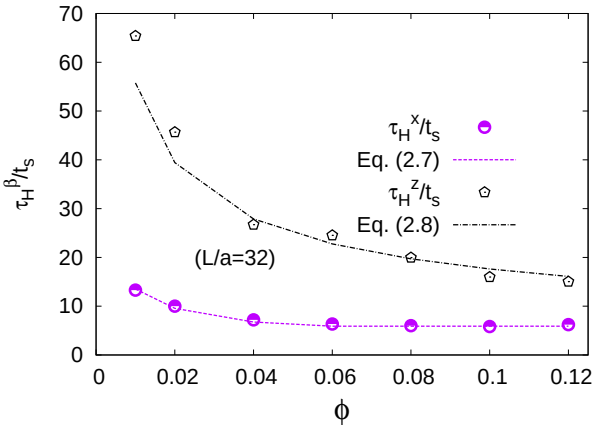

FIGURE 2.5: Hydrodynamic velocity fluctuation relaxation times for both the vertical and horizontal directions as a function of volume fraction. The dashed line indicates the scaling of τ_H^x/t_s and the dot-dashed line indicates the scaling of τ_H^z/t_s. The simulation data are represented by points. This plot shows that the difference in the vertical and horizontal relaxation times decreases with increasing volume fraction at moderate volume fraction regimes. Our data show good agreement with the scaling Eqs. (2.7) and (2.8).

2.3.3 Scaling and Anisotropic Behavior of Diffusion

Diffusion occurs due to the fluctuating motion of particles. Individual particles lose the memory of their velocity after experiencing hydrodynamic interactions with surrounding particles and thereafter follow a random-walk diffusion process. To find the scaling of a long-time steady-state self-diffusion coefficient, we consider the total diffusion coefficient D as the sum of the thermal contribution D_0 and the hydrodynamic contribution D_{H}, where the latter is estimated as:

$$D_{\mathrm{H}}^{\beta} \approx (\Delta V_{\mathrm{H}}^{\beta})^2 \tau_{\mathrm{H}}^{\beta}. \tag{2.9}$$

Based on the aforementioned scaling relationships for $\Delta V_{\mathrm{H}}^{\beta}$ and $\tau_{\mathrm{H}}^{\beta}$, for both low and moderate volume fraction regimes, we can also find the scaling for the diffusion coefficients in the z and x directions:

$$D_z/D_0 = \begin{cases} 1 + A_1^z A_2^z \mathrm{Pe}\,(L/a)^{3/2}\,\phi^{1/2} = 1 + 0.149\mathrm{Pe}\,(L/a)^{3/2}\,\phi^{1/2}, & (\phi \lesssim 0.04) \\ 1 + A_1^z A_2^z B_1^z \mathrm{Pe}\,(L/a)^{3/2}\,\phi^{-1/2} = 1 + 0.0056\mathrm{Pe}\,(L/a)^{3/2}\,\phi^{-1/2}, & (0.04 < \phi \lesssim 0.12) \end{cases}, \tag{2.10}$$

$$D_x/D_0 = \begin{cases} 1 + A_1^x A_2^x \mathrm{Pe}\,(L/a)^{3/2}\,\phi^{1/2} = 1 + 0.006\mathrm{Pe}\,(L/a)^{3/2}\,\phi^{1/2}, & (\phi \lesssim 0.04) \\ 1 + A_1^x A_2^x B_1^x (B_2^x)^{-1/2} \mathrm{Pe}\,(L/a)^{3/2} = 1 + 0.0013\mathrm{Pe}\,(L/a)^{3/2}. & (0.04 < \phi \lesssim 0.12) \end{cases}. \tag{2.11}$$

These scaling relations indicate that the vertical and horizontal diffusion coefficients normalized by the equilibrium diffusion coefficient increase linearly with Pe, but with a smaller pre-factor in the horizontal direction. In addition, they scale as $(L/a)^{3/2}$ with the system size for the full range of volume fractions that we have considered. Furthermore, both the vertical and horizontal

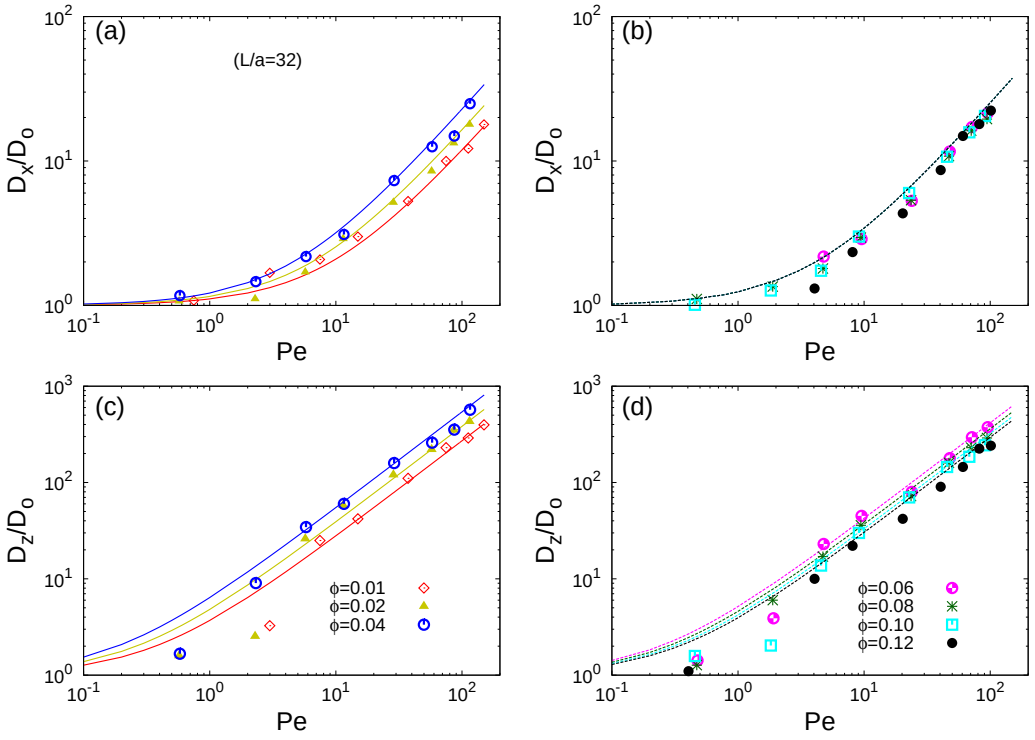

FIGURE 2.6: A comparison of the long-time steady-state self-diffusion coefficients in both the vertical and horizontal directions with those predicted by the scaling Eqs. (2.10) and (2.11) as a function of Pe. The self-diffusion coefficients are normalized by the equilibrium diffusion coefficient D_0. Figures "(a)" and "(b)" show the scaling of D_x/D_0 for low and moderate volume fractions, respectively, whereas "(c)" and "(d)" show the scaling of D_z/D_0 for low and moderate volume fractions, respectively. The simulation results are represented by points. The lines indicate the scaling relations. The symbols and lines are color-coded with respect to the volume fraction.

	Scaling of D_β/D_0	
	Low ϕ	Moderate ϕ
	($\phi \lesssim 0.04$)	($0.04 < \phi \lesssim 0.12$)
D_x/D_0	$\sim \phi^{1/2}$	$\sim \phi^{0}$
D_z/D_0	$\sim \phi^{1/2}$	$\sim \phi^{-1/2}$

TABLE 2.3: Summary of the scaling obtained for the self-diffusion coefficients (D_β/D_0) in both the vertical and horizontal directions. Additionally, diffusion coefficients in both directions scale as $(L/a)^{3/2}$ with system size and linearly with Pe.

diffusion coefficients scale with $\phi^{1/2}$ at low volume fraction, but at moderate volume fraction the diffusion coefficient in the vertical direction scales as $\phi^{-1/2}$, and the horizontal diffusion coefficient becomes independent of volume fraction. This additional dependency on $\phi^{-1/2}$ in the vertical direction at moderate volume fractions causes a decrease in the diffusion anisotropy with increasing volume fraction. The scaling relations for the diffusion coefficients are summarized in Table 2.3. The long-time steady-state self-diffusion coefficient ($D_\beta = \lim_{t\to\infty} D_\beta(t)$) is obtained

from the linear growth of the mean-square displacement (MSD) in the horizontal and vertical directions as follows:

$$D_x(t) = \frac{1}{2t}\left\langle \left(R_{ix}(t) - R_{ix}(0)\right)^2 \right\rangle, \tag{2.12}$$

$$D_z(t) = \frac{1}{2t}\left\langle \left(R_{iz}(t) - R_{iz}(0) - V_{\text{sed}}t\right)^2 \right\rangle. \tag{2.13}$$

The equilibrium self-diffusion coefficient can be obtained using the Einstein relationship:

$$D_0 = \lim_{t\to\infty} \frac{1}{6t}\left\langle \left(\boldsymbol{R}_i(t) - \boldsymbol{R}_i(0)\right)^2 \right\rangle. \tag{2.14}$$

Figure 2.6 shows a comparison of the long-time steady-state self-diffusion coefficients with the scaling relations. Figures 2.6 (a) and (b) show the diffusion coefficient, as a function of Pe in the horizontal direction for low and moderate volume fractions, respectively. Figures 2.6 (c) and (d) show the diffusion coefficient in the vertical direction, as a function of Pe for low and moderate volume fractions, respectively. Figures 2.6 (a) and (c) indicate that the diffusion coefficient increases with increasing volume fraction both in the horizontal and vertical directions at low volume fractions. In contrast with the low volume fraction regime, the vertical diffusion coefficient decreases with increasing volume fraction at moderate volume fractions, as shown in the Fig. 2.6 (d). Figure 2.6 (b) demonstrates no change in the horizontal diffusion coefficient. This decrease in the vertical diffusion coefficient is attributed to the $\phi^{-1/2}$ scaling of τ_{H}^{z}. However, due to the saturation of τ_{H}^{x} and ΔV_{H}^{x} at moderate volume fraction, no change is observed in the horizontal diffusion coefficient.

Our simulation results indicate that the diffusion coefficients increase linearly with increasing Pe, both parallel and perpendicular to gravity. A deviation from the scaling relations is evident at low Pe. Because scaling relations are derived by adding pure thermal and hydrodynamic forces, these relations are expected to show good agreement with the simulation results when either thermal or hydrodynamic fluctuations dominate the phenomena. Hence, this deviation indicates the transition regime in which neither force is dominant. Our simulations show good agreement with Eqs. (2.10) and (2.11) at high Pe, demonstrating the dominance of the hydrodynamic interactions.

The majority of studies [5, 9, 13, 14, 24, 47] on particle diffusion in sedimentation have focused on the non-Brownian regime. Particle diffusion and its anisotropic nature at finite Pe values have not yet been explored. We have attempted to investigate this anisotropic behavior and found that, for a given volume fraction, the anisotropy increases with increasing Pe, becoming saturated at higher Pe, as shown in Fig. 2.7. This observation suggests that the effect of thermal fluctuations is significant at low Pe, before the HIs begin to dominate the sedimentation phenomenon. We can predict the anisotropic behavior of the diffusion at finite Pe with scaling relationships.

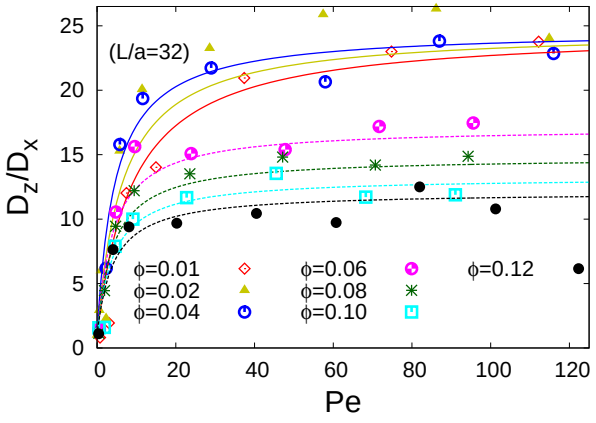

FIGURE 2.7: The anisotropy of the vertical (D_z) and horizontal (D_x) self-diffusion coefficients as a function of Pe for different volume fractions. The solid lines indicate the scaling of D_z/D_x at low volume fractions, whereas the dashed lines indicate the scaling at moderate volume fractions. The scaling lines are obtained by dividing Eq. (2.10) with Eq. (2.11) for the respective volume fraction regime. Lines and points of the same color indicate the results for the same volume fraction.

Our data show good agreement with the predicted diffusion anisotropy, as indicated in Fig. 2.7. Furthermore, the scaling relationships suggest that the saturated or steady-state value of the anisotropy remains unchanged at low volume fractions and decreases with increasing volume fraction at moderate volume fractions, as shown in Fig. 2.7. This decrease in anisotropy is attributed to the decrease in the difference between the vertical and horizontal relaxation times. This difference is decreased by the $\phi^{-1/2}$ scaling of the vertical relaxation time at moderate volume fractions. The horizontal relaxation time is independent of volume fraction in this regime as shown in Table 2.1.

Our simulation results are also compared with the previous experimental and simulation results in Fig. 2.8, which shows the diffusion anisotropy, as a function of the volume fraction. Nicolai [5] obtained these results in a spatially screened regime, whereas Cunha [24] and Padding [23] performed DNS and SRD simulations in an elongated simulation box with an aspect ratio of 3. We have obtained a relatively high value of the anisotropy at a low volume fraction. This higher value originates from the difference in vertical and horizontal relaxation times. Because diffusivity is the product of ΔV_{H}^2 and τ_{H}, a larger difference in relaxation time leads to a higher diffusion anisotropy. The diffusion anisotropy can be reduced by increasing the aspect ratio of the simulation box [3]. An increase in the aspect ratio reduces this difference and thus the diffusion anisotropy, as exhibited by Cunha [24] and Padding [23]. We obtained an anisotropy of ≈ 24, whereas Cunha and Padding found this anisotropy to be ≈ 10 and 7, respectively, at low volume fractions. In another simulations study [47], Kuusela et al. obtained large diffusion coefficients in both directions using a 2D periodic square simulation box, but the ratio of diffusion coefficients shows good agreement with our results. In contrast with the present

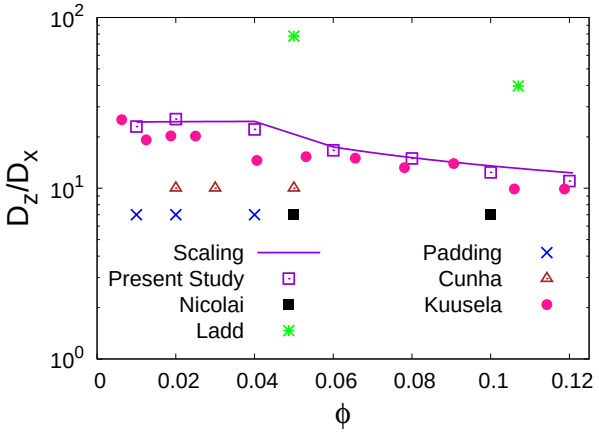

FIGURE 2.8: Comparison of the diffusion anisotropy with the scaling and previously published experimental and simulated data. Nicolai [5] obtained the low anisotropy value in an experimental study in a spatially screened regime, whereas Cunha [24], Padding [23] and Ladd [18] achieved these results from the DNS, SRD and LBM, respectively. A relatively large value of anisotropy is achieved due to cubic periodic box and spatially unscreened regime. Our data show good agreement with the simulation study of Kuusela et al. [47] and the scaling.

study, Nicolai [5] obtained an anisotropy of ≈ 7 and found no decrease in the anisotropy at moderate volume fractions, primarily because they obtained their results in a large container, which is many times greater than the correlation length. In simulations, the use of such a large system is impossible due to the large computational cost. Another possible explanation for the discrepancy between the simulations and the experimental results is the presence of a side wall in the experiments, which creates micro-structural inhomogeneities over time [38, 39]. In addition, the presence of polydispersity, even to a small extent, can temper the diffusion. Ladd [18] obtained a high anisotropy ≈ 77 at $\phi = 0.05$. This large value is attributed to the small system size and the use of full periodic boundary conditions. Similar to the present study, Ladd [18] demonstrated that diffusion anisotropy decreases with increasing volume fraction. The anisotropy of diffusion, which was ≈ 77 at $\phi \approx 0.05$, decreased to ≈ 39 at $\phi \approx 0.107$.

2.3.4 Finite Size Effects

Theoretical arguments [4] and simulations [18] have long exhibited the strong dependency of velocity fluctuations on the system size for a random suspension of particles. In contrast, experiments [5, 10] show no such divergence. This disagreement was solved by Segre et al. [9] who suggested that the velocity fluctuations increase with the system size only when the system size is smaller than the correlation length, and above this correlation length, the simulations and experiments should be in good agreement. In experiments, one has the freedom to use large system sizes, whereas in simulations, large systems require enormous resources. Thus, most simulation studies [14, 23, 24, 26] are affected by the artefacts induced by the finite system size.

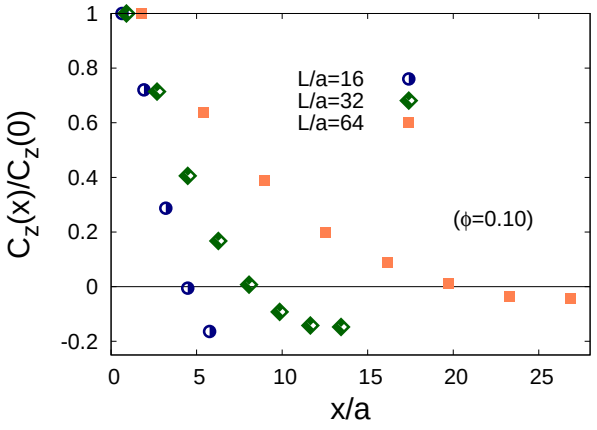

FIGURE 2.9: Spatial correlation function of the z-component of velocity, as a function of the distance perpendicular to gravity, demonstrating the effects of system size on velocity fluctuations. All simulations were performed at a volume fraction of $\phi \approx 0.10$ and Pe ≈ 80.

To observe the system size dependency in our results, we defined the spatial correlation function of the velocity fluctuations, which defines the flow pattern of the particles as follows:

$$C_z(\boldsymbol{r}) = \frac{2L^3}{N^2}\left\langle \sum_{i<j} \delta V_{iz}\delta V_{jz}\delta(\boldsymbol{r}-\boldsymbol{r}_{ij})\right\rangle. \tag{2.15}$$

We define $C_z(z)$ and $C_z(x)$, with respect to the distance vector $\boldsymbol{r}$, in either the vertical $\boldsymbol{r} = z\boldsymbol{\delta}_z$ or horizontal $\boldsymbol{r} = x\boldsymbol{\delta}_x$ direction. We plotted the spatial correlation function of the z-component of the velocity as a function of the distance perpendicular to gravity in Fig. 2.9, using three different cubic boxes L/a =16, 32, and 64, at $\phi = 0.10$. Figure 2.9 shows that the velocity fluctuations become long-ranged with an increase in the system size, which is in agreement with the tendencies observed in similar simulation studies [23, 47]. Our simulation results support the experimental findings of Segre [9] when the system size is smaller than the correlation length. Therefore, the particle motion should be affected by the finite system in our simulations. Figure 2.9 shows that a large system size is needed to reproduce the saturation of the velocity fluctuations, but this requires enormous computational time and resources. Therefore, most of the computational studies [14, 20, 23, 24] are similarly limited. Systematic experimental [6, 9] and simulation [17, 18] studies, however, have revealed that the effects of finite system size on velocity fluctuations can be effectively explained using the concept of finite-size scaling [23]. We believe that there is value in performing critical tests on the scaling concept. In addition, the experiments [6, 9] and simulations [17, 18] addressing the effects of finite system size on velocity fluctuations have also established that finite system size may lead to smaller velocity fluctuations [23].

2.4 Concluding Remarks

We performed the direct numerical simulations of steady-state sedimenting particles at a finite Peclet number and investigated the relative effects of thermal and hydrodynamic fluctuations and scaling of hydrodynamic velocity fluctuations and self-diffusion with respect to volume fraction and system size. We observed a clear transition from a Brownian motion dominant regime to a hydrodynamic fluctuations dominant regime. Moreover, the hydrodynamic velocity fluctuations increased with increasing volume fraction at low volume fraction ($\phi \lesssim 0.04$), whereas at moderate volume fraction ($0.04 < \phi \lesssim 0.12$), their behavior was independent of ϕ. We concluded that the amplitudes of the velocity fluctuation correlations scale with the square of the Stokes velocity at large Pe, with vertical hydrodynamic velocity fluctuations that are ≈ 2.4 times larger than the horizontal hydrodynamic velocity fluctuations at low volume fractions. At moderate volume fractions, this value drops to ≈ 2.07. In addition, we tested the scaling relations for the hydrodynamic velocity fluctuations suggested by Hinch [36] for different system sizes and volume fractions. We found that this scaling worked well for low volume fractions and deviated at moderate volume fraction regimes.

We found that both the vertical and horizontal velocity fluctuations scale as $(\phi L/a)^{1/2}$ at low volume fractions, saturating with respect to ϕ at moderate volume fractions. Similarly, the horizontal velocity fluctuation relaxation time scales as $(L/a\phi)^{1/2}$ at low volume fractions, saturating with respect to ϕ at moderate volume fractions. This result is in contrast with that of the vertical relaxation time, which scales as $(L/a\phi)^{1/2}$ for both regimes. Furthermore, we found that the difference in the vertical and horizontal hydrodynamic velocity fluctuation relaxation times decreased with increasing volume fraction at moderate volume fractions.

Based on the scaling of the hydrodynamic velocity fluctuations and their relaxation times, we inferred the scaling relations of the long-time steady-state self-diffusion coefficient for both low and moderate volume fraction regimes. We found that both the vertical and horizontal self-diffusion coefficients scale as $(L/a)^{3/2}\phi^{1/2}$ at low volume fractions. In contrast to the low volume fraction regimes, the vertical self-diffusion coefficient scales as $(L/a)^{3/2}\phi^{-1/2}$ at moderate volume fractions due to a decrease in the vertical relaxation time with volume fraction, whereas the horizontal diffusion coefficient is saturated with respect to ϕ in this regime. These relations of hydrodynamic velocity fluctuations, their relaxation times and the self-diffusion coefficients are summarized in Table 2.1 and 2.3. The scaling of the diffusion coefficients allows us to predict the anisotropy of the vertical and horizontal diffusion. We found that the diffusion anisotropy increases with increasing Pe, and saturates at high Pe. This saturated value remains unchanged at low volume fractions and decreases with increasing volume fraction at moderate volume fractions. The decrease in the anisotropy with volume fraction is induced by the decrease in the difference in magnitudes of the vertical and horizontal hydrodynamic relaxation times.

Chapter 3

Sedimentation of non-Brownian Particles

3.1 Introduction

Most of the studies [5, 9, 13, 23, 24, 36] on sedimentation are performed in the Stokes regime, where relatively simple phenomenological changes make it easy to explore experimentally and computationally. Due to extensive research in Stokes regime, which is mainly focused at low volume fraction, the theoretical aspects [36] at low volume fraction are well developed and also validated by experimental [5, 9, 13] and simulation studies [20, 23, 24], whereas these studies fail to give a convincing behavior of static and dynamic properties especially at moderate and high volume fractions. The main objective of this Chapter is to investigate the evolution of microstructure and its effects on velocity fluctuations, their relaxation times and self-diffusion, in a steady state homogeneous suspension of non-Brownian sedimenting particles, over a range of volume fraction from 0.01 to 0.5. We organized this work in such a way that we could test the ϕ dependency at the low, moderate and high volume fraction regimes. Unfortunately, we have only a limited number of results [5, 30] to compare with at high volume fraction, due to lack of research in this regime.

In this Chapter, Section 3.2 explains the simulation method and results are presented in Section 3.3. We conclude this Chapter in Section 3.4.

3.2 Simulation Parameters

Simulations of spherical colloidal particles were performed under periodic boundary conditions, with volume fraction ranging from 0.01 to 0.5. In the previous chapter, we explored the relative

effects of thermal and hydrodynamic interactions at finite Peclet number (Pe) ranging from 0 to 120, which revealed that at Pe $\gtrsim 30$, diffusivities, velocity fluctuations and their relaxation times show non-Brownian characteristics. Hence, we have used the Pe > 80 data of our previous study, along with the new simulation data at high volume fractions and system sizes. In principal, our method allows us to reach infinite Pe, but for this study the data at Pe > 80 is sufficient. Three different cubic periodic box of dimension $L/a = 16$, 32 and 64 are used, particle radius is kept constant at 4Δ and interface thickness is set to unity in the unit of grid spacing in all simulations. This particular particle size has already been used by Nakayama et al. [60] for different test cases and it accurately produced the near and far-field flows, pressure distribution, drag force and lubrication interactions. Gravity was introduced in the z-direction. We set the particle to fluid density ratio to 5 and fluid density equal to one. In order to ignore the inertial effects and remain within the Stokes regime, we kept the particle Reynolds number, $\mathrm{Re} = \rho_f \sigma V_s/\eta$, constant at ≈ 0.3.

3.3 Results and Discussion

3.3.1 Hindered Settling

The average settling velocity of the suspension is reduced with respect to the terminal velocity of an isolated particle with increasing volume fraction, due to fluid back flow and particle-particle interactions. If a simulation method has accurately characterized the many-body hydrodynamic interactions then it should reproduce the so called hindered settling function, which has been widely studied theoretically [35, 91–95] and experimentally [5]. The simplest semi-empirical relation for this function is proposed by Richardson and Zaki [91] as a power law function, $V_{\mathrm{sed}}/V_s = (1-\phi)^n$, where n is a power law exponent. We also verify our computation scheme by comparing the average settling velocity of the suspension with previous simulations [23, 52], theoretical predictions [35, 91–95] and experimental [5] results, as shown in Fig. 3.1. Different studies [5, 23, 24, 52, 92, 95] have found different exponents ranging from 4.7 to 6.55 for the Stokes flow. In our study the best suited exponent is 5.3, well within these two extremes. Our results also show a good agreement with the theoretical prediction of Hayakawa et al. [93], which takes into account HIs. A good agreement of our data with other theoretical, experimental and simulation results shows the accuracy of our method.

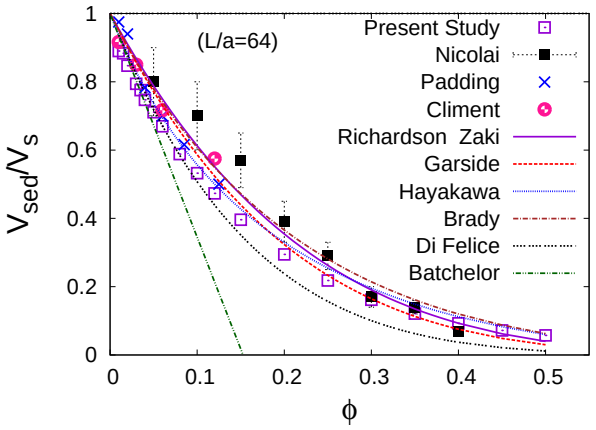

FIGURE 3.1: Average settling velocity V_{sed} of the particles normalized by the Stokes velocity V_s as a function of volume fraction to highlight the hindered settling of the particles. Theoretical predictions of Richardson and Zaki [91], Garside [92], Hayakawa [93], Brady [94], Di Felice [95] and Batchelor [35] are represented with lines, whereas points show the experimental data of Nicolai [5] and simulation data of Padding [23] and Climent [52].

3.3.2 Microstructure

For a given initial configuration, system require a certain period of time to acquire steady-state sedimentation velocity. Snapshots of steady state configuration of the particles for $\phi = 0.01$ and 0.04 are shown in Fig. 3.2. We monitored the data, and only that corresponding to the steady-

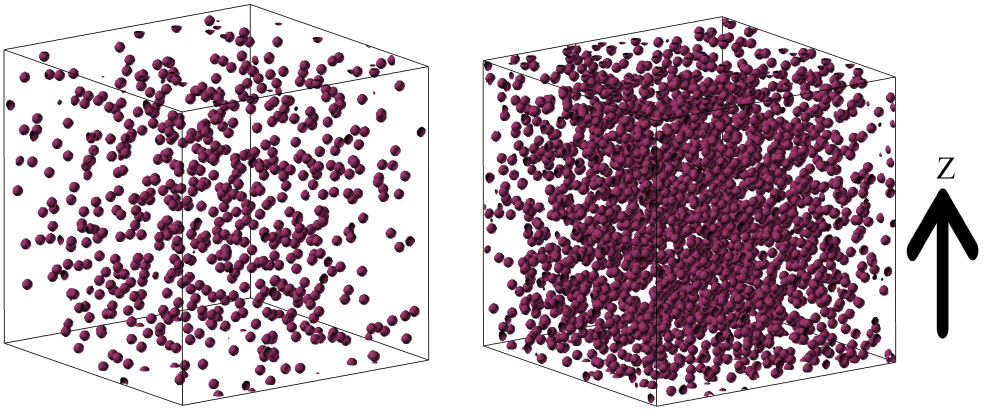

(a) $\phi = 0.01$ (b) $\phi = 0.04$

FIGURE 3.2: snapshots of steady state distribution of particles in a cubic box of size $L/a = 64$ for $\phi = 0.01$ and $\phi = 0.04$, where gravity is in $-z$ direction.

state velocities was used. Simulations are run for 1000-1500t_s; sufficient to yield statistically meaningful data for this analysis.

In order to characterize the modulation of the local density around a given particle as a function of radial distance, we calculated the RDF defined in Eq. (2.1) and plotted in Fig. 3.3. The $g(r)$ primarily depicts the local microstructure, but it also gives information about the long

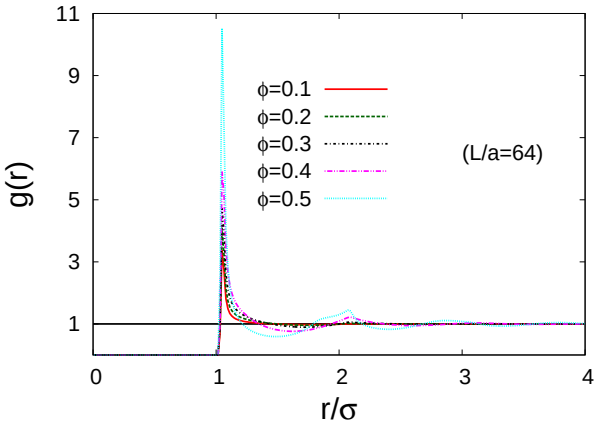

FIGURE 3.3: Radial distribution function $g(r)$ as a function of radial distance r for different volume fractions, where $r = |\boldsymbol{r}|$.

range ordering of particles. At low volume fraction this local ordering vanishes for small distance, whereas as we increase the volume fraction this ordering of the particles also increases as shown by the appearance of oscillations beyond the first peak at high volume fraction, which is in agreement with the theoretical predictions [90].

The $g(r)$ provides the information of the average number of particles in a shell, regardless of their positions within that shell. In a homogeneous and isotropic system like particle undergoing random Brownian motion, $g(r)$ gives useful information, whereas in an anisotropic suspension like sedimentation under gravity, we need to determine whether particles prefer to position themselves in a particular direction with respect to a neighbouring particle. In order to investigate this preference, we compute the PDF in cylindrical coordinates, as shown in Fig. 3.4.

These maps show that at low Re, particles prefer to position themselves in a horizontal direction with respect to a neighboring particle at low ϕ. This anisotropy decreases with the increase of volume fraction and at $\phi \gtrsim 0.15$, the microstructure is isotropic. Moreover, it also shows a long range ordering of the particles at high volume fractions. It depicts that microstructure is ordered and effects of the gravitational force on microstructure are nullified by the closely packed particles. The anisotropic nature of the phenomena is already diminished, which dictates the limit of volume fraction in this study. It will be interesting to see how this mictrostructure affects the transport properties of the suspension, as little is known about the influence of microstructure [12,25,96]. We will discuss these effects of microstructure on suspension properties briefly in the next section.

Figures 3.3 and 3.4 depict the qualitative picture of the particle orientation and to quantify this, we calculated the particle orientation tensor as,

$$Q^{\gamma\beta}(r) = \frac{\left\langle \sum_{i<j} \hat{r}_{ij}^{\gamma} \hat{r}_{ij}^{\beta} \delta\left(r - r_{ij}\right) \right\rangle}{\left\langle \sum_{i<j} \delta\left(r - r_{ij}\right) \right\rangle}, \tag{3.1}$$

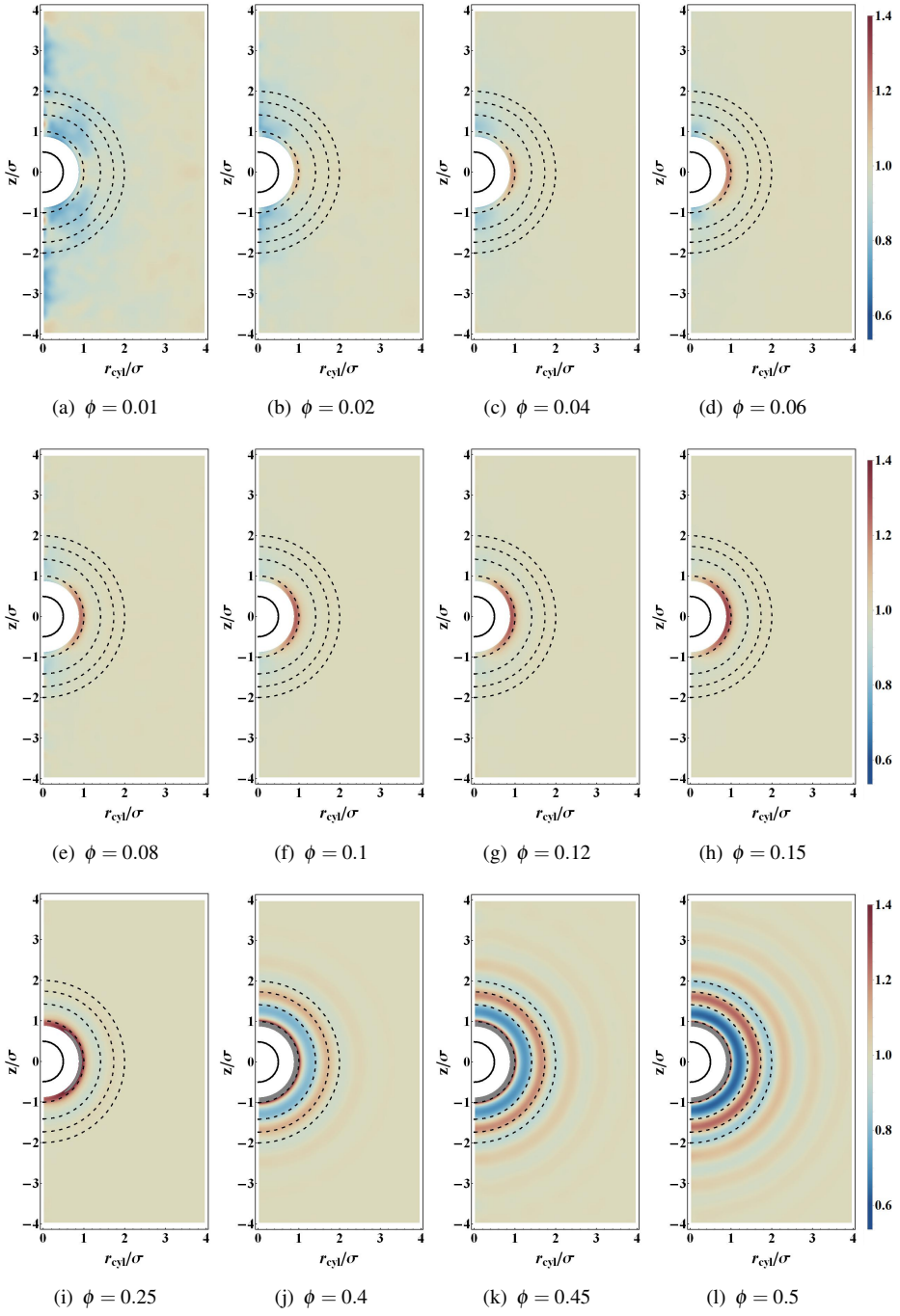

(a) $\phi = 0.01$ (b) $\phi = 0.02$ (c) $\phi = 0.04$ (d) $\phi = 0.06$

(e) $\phi = 0.08$ (f) $\phi = 0.1$ (g) $\phi = 0.12$ (h) $\phi = 0.15$

(i) $\phi = 0.25$ (j) $\phi = 0.4$ (k) $\phi = 0.45$ (l) $\phi = 0.5$

FIGURE 3.4: Pair distribution function of particles in cylindrical coordinates ($g\left(r_{\mathrm{cyl}}, z\right)$) for a system size $L/a = 64$.

where $\gamma, \beta \in x, y, z$ and $\hat{r}_{ij}^{\beta} = \frac{r_i^{\beta} - r_j^{\beta}}{r_{ij}}$. From this orientation tensor, we defined the anisotropic factor (AF) as,

$$\mathrm{AF} = \frac{1}{\mathrm{r}_2 - \mathrm{r}_1} \int_{\mathrm{r}_1}^{\mathrm{r}_2} [Q^{xx}(r) - Q^{zz}(r)] dr, \tag{3.2}$$

where the integration limits are taken from $r_1 = 1\sigma$ to $r_2 = 1.5\sigma$. We plotted this AF in Fig. 3.5 to quantify the anisotropy in particle orientation. It shows that particles have a preference to

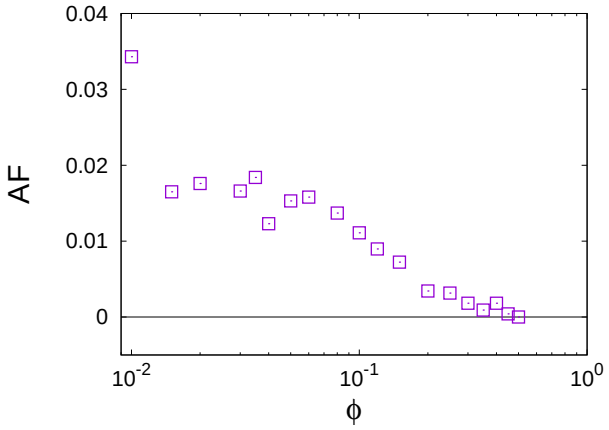

FIGURE 3.5: The anisotropic factor (AF) defined in Eq. (3.2) against the volume fraction.

orient themselves in a horizontal direction with respect to neighbouring particle at low volume fraction and this preference decreases at high volume fraction. This shows that at low volume fraction microstructure play a dominant role in determining the transport properties, whereas at high volume fraction many-body interactions overpower the phenomena and decrease the anisotropic nature of microstructure.

3.3.3 Velocity Fluctuations

In order to characterize the effect of volume fraction on velocity fluctuations, we calculate the autocorrelation functions of temporal velocity fluctuations, defined in Eqs. (2.2) and (2.3). We

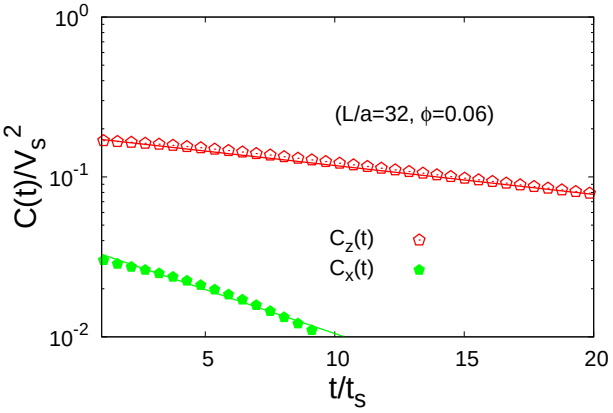

FIGURE 3.6: Temporal autocorrelation functions of the vertical $(C_z(t))$ and horizontal $(C_x(t))$ velocity fluctuations normalized by the square of the Stokes velocity V_s. Points show the simulation data, whereas lines show the exponential fit of the form, $C_\beta(t) = \left(\Delta V_H^\beta\right)^2 \exp(-t/\tau_H^\beta)$, where ΔV_H^β $(\beta \in x,z)$ and τ_H^β denote the amplitude and the relaxation time of the hydrodynamic velocity fluctuations, respectively. Time is normalized by the Stokes time t_s, where $t_s = a/V_s$. Lines and symbols are color-coded for the same direction.

plotted the velocity fluctuation autocorrelation functions in the z and x directions in Fig. 3.6.

These correlations are normalized by the square of the Stokes velocity to highlight the non-equilibrium hydrodynamic fluctuations. It shows a large difference in the vertical and horizontal velocity fluctuations relaxation times, whereas Nicolai et al. [5] observed a small difference in these relaxation times. This difference arises from the cubic periodic box, as suggested by Koch's theory [3] and explained in Chapter 2 and Section 2.3.2. Nicolai et al. [5] suggested that

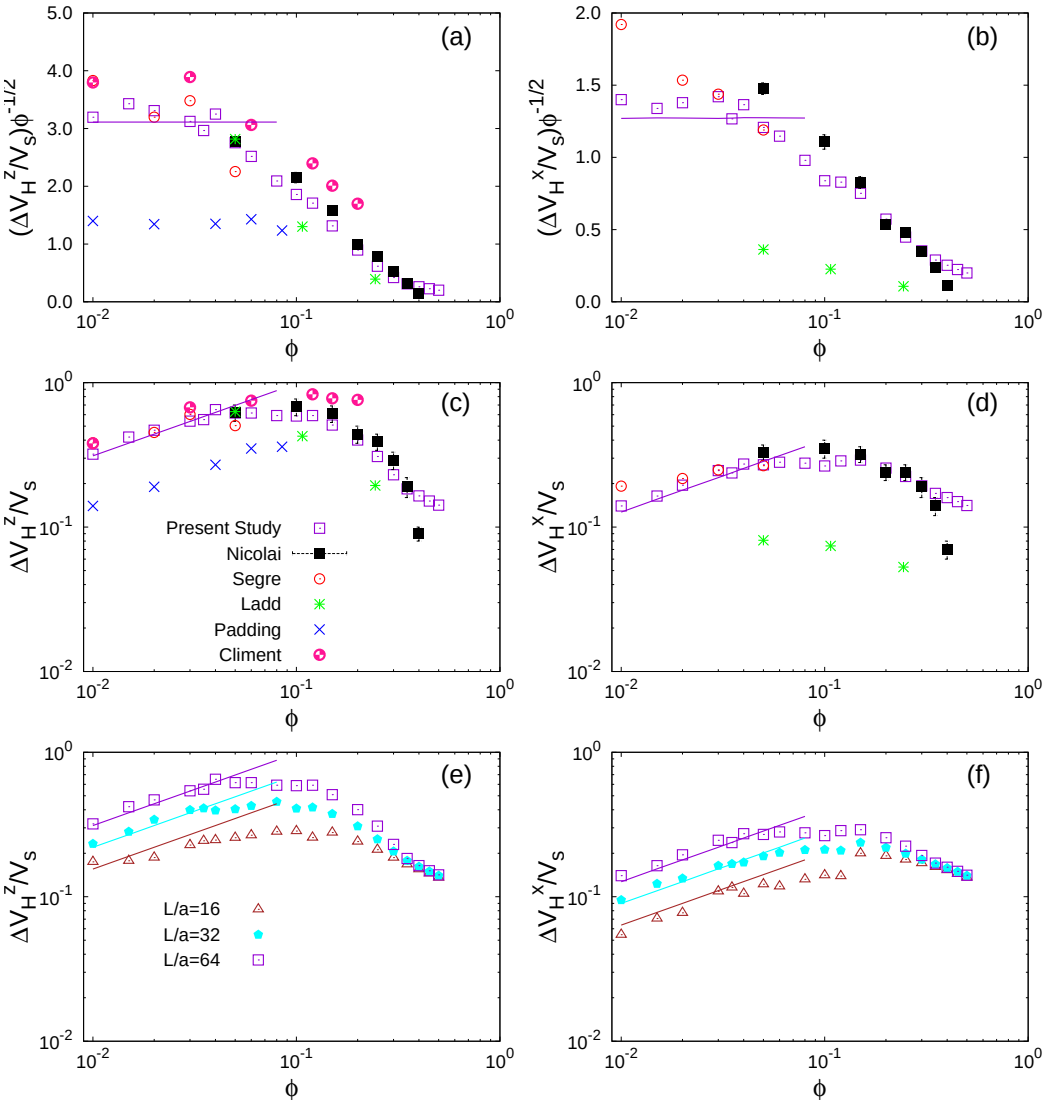

FIGURE 3.7: Hydrodynamic velocity fluctuations have been shown in three different representations to highlight the scaling of velocity fluctuations with respect to volume fraction and system size in both directions. In "(a)" and "(b)" velocity fluctuations are normalized by the product of the Stokes velocity and $\phi^{1/2}$ to show the $\phi^{1/2}$ scaling at low volume fractions, whereas "(c)" and "(d)" show the velocity fluctuations normalized by the Stokes velocity to emphasize the scaling at low, cross-over and high volume fraction regimes. Moreover, "(e)" and "(f)" depict the $(L/a)^{1/2}$ scaling with respect to three different system sizes $L/a = 16$, 32 and 64. We also compared our results of largest system size with the experimental data of Nicolai [5] and Segre [9] and simulation results of Ladd [18], Padding [23] and Climent [52] in top four figures. Lines in figures show the $\phi^{1/2}$ behavior.

these correlations decay exponentially as, $C_\beta(t) = \left(\Delta V_{\mathrm{H}}^{\beta}\right)^2 \exp(-t/\tau_{\mathrm{H}}^{\beta})$. We fit this expression

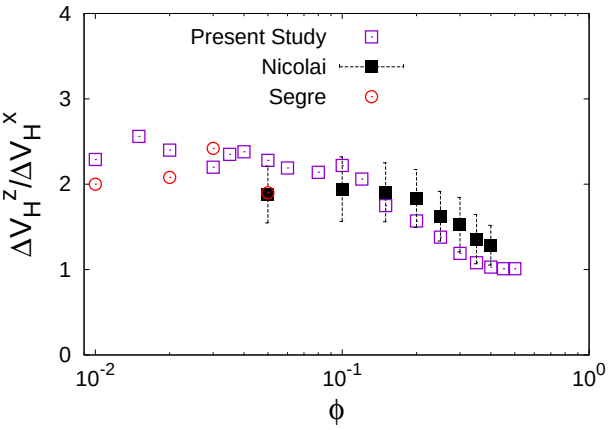

FIGURE 3.8: Anisotropy in velocity fluctuations as a function of volume fraction for system size $L/a = 64$. Results are compared with the experimental data of Nicolai [5] and Segre [9].

to obtain the values of $\Delta V_{\mathrm{H}}^{\beta}$ (hydrodynamic velocity fluctuation) and $\tau_{\mathrm{H}}^{\beta}$ (relaxation times), as shown by the solid lines in the Fig. 3.6. We calculated the values of $\Delta V_{\mathrm{H}}^{\beta}$ and $\tau_{\mathrm{H}}^{\beta}$ for different volume fractions and system sizes and plotted them in Figs. 3.7 and 3.9. Figure 3.7 shows the velocity fluctuations both in z and x directions, respectively, for three different system sizes to highlight the scaling with respect to the volume fraction and the finite size effects. Both the z and x direction velocity fluctuations show the same qualitative behavior. We observed that at the low volume fraction regime ($\phi \lesssim 0.04$), velocity fluctuations show a $\phi^{1/2}$ dependence in accordance with the theoretical prediction [36, 39] for homogeneous suspensions, as shown by the plateaus in Figs. 3.7(a) and (b), where velocity fluctuations are normalized by $V_{\mathrm{s}}\phi^{1/2}$. At $\phi > 0.04$, our results show a cross-over, where velocity fluctuations are independent of ϕ and at high volume fractions roughly at $\phi \gtrsim 0.15$, a sharp decrease in the velocity fluctuations similar to that observed by Nicolai et al. [5] is evident in both directions, as shown in Figs. 3.7(c) and (d).

Hinch [36] predicted the scaling of velocity fluctuations at low volume fraction as $\Delta V_{\mathrm{H}}^{\beta} \sim \phi^{1/2}$, which works well as far as particles are free to move, but with the increase of volume fraction particles have more resistance in the form of other particles. We have seen this in Fig. 3.4, where at the high volume fraction regime roughly at $\phi \gtrsim 0.15$, the particle density around a test particle is isotropic. Hence, this leads us to declare that at low volume fraction transport properties are dependent on the microstructure of the system. Moreover, at high volume fraction the phenomena is rather trivial, where particles are closely packed and many-body interactions dominate the phenomena and cause the sharp decrease in the velocity fluctuations at $\phi \gtrsim 0.15$. In addition, we believe that there is a cross-over, where neither is dominant. Most of the theoretical and experimental studies have focused on the low volume fraction regime, and the theoretical aspects of the physical phenomena is very well understood, whereas at high volume fractions, the phenomena is trivial, where the individual particle motion is suppressed by the formation of clusters or aggregates and the transport properties are governed by the motions of these clusters.

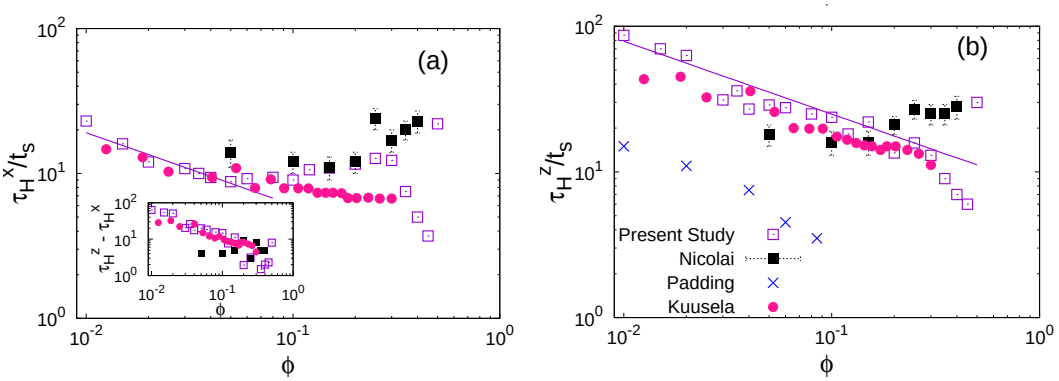

FIGURE 3.9: Decay of relaxation times as a function of volume fraction. Figures "(a)" and "(b)" show the x and z directions relaxation times, respectively. The τ^z_H/t_s relaxes approximately as $\phi^{-1/2}$ in the full range of volume fraction, whereas τ^x/t_s obeys a $\phi^{-1/2}$ dependency at low volume fraction only. The figure inset shows the the difference in vertical and horizontal relaxation times. Results are compared with the experimental data of Nicolai [5] and simulation results of Padding [23] and Kuusela [30]. Lines in figures "(a)" and "(b)" show the $\phi^{-1/2}$ behavior.

In contrast to these low and high volume fraction regimes, the physical aspects of the cross-over have not yet been explored theoretically. Brenner [39] has suggested a transition from $\phi^{1/2}$ to $\phi^{1/3}$, which has not yet been confirmed by any other study. Furthermore, Cunha et al. [24] also observed the transition/cross-over regime, but unfortunately the dependency on ϕ is not yet clear. Apart from the ϕ dependence, Figs. 3.7(e) and (f) also show the increase of velocity fluctuations with increasing system size as $\sim (L/a)^{1/2}$ at low volume fractions, in accordance with the theoretical predictions [24, 36, 39], whereas their character becomes independent of system size at very high volume fraction. Considering the correlation length found by Segre et al. [9], our system size $L/a = 64$ shows good agreement at high volume fraction with those studies, which are independent of finite size effects.

We have also compared our results with other simulations [18, 23, 52] and experimental [5, 9] data in Fig. 3.7. Our results show good qualitative and quantitative agreement with other studies [5, 9, 52]. Even though a good qualitative agreement is evident with the simulation studies of Padding et al. [23] and Ladd [18], the quantitative discrepancy is due to the finite system size effects in their studies, where the former used a rectangular periodic box of size $L/a = 20.6$ and the latter a small system with only 32 particles. We also compared the anisotropy in the velocity fluctuations in the Fig. 3.8. The vertical velocity fluctuations are approximately twice as large as horizontal velocity fluctuations for $0.01 \lesssim \phi \lesssim 0.12$, whereas a further increase in the volume fraction slightly decreases this anisotropy, in good agreement with Nicolai et al. [5].

Along with the velocity fluctuations, their relaxation times are another key parameter which dictates the dispersive motion of the particles. We plotted the hydrodynamic relaxation time in Fig. 3.9 and compared it with other simulation and experimental results. Unlike velocity fluctuations, we have found a different dependency of volume fraction in the vertical and perpendicular directions. Relaxation times in the vertical direction follow approximately a $\phi^{-1/2}$ relaxation in

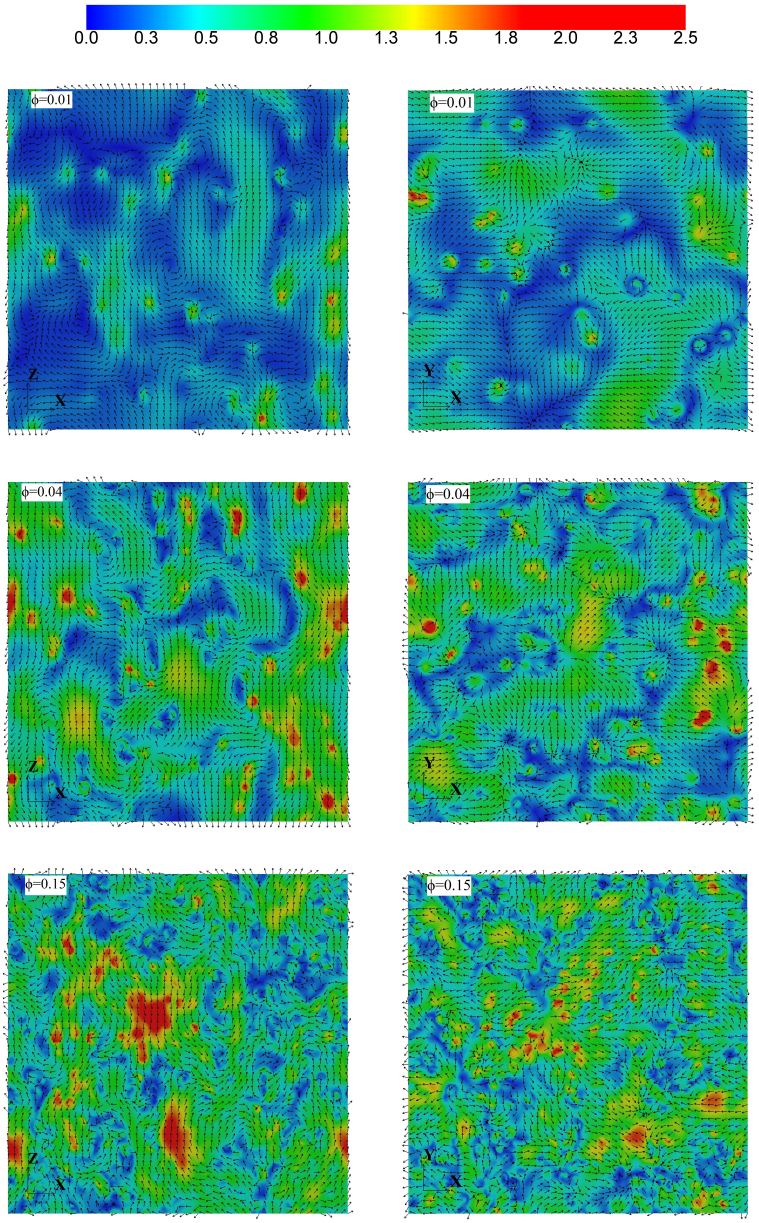

FIGURE 3.10: Snapshots of projection of total velocity field $\boldsymbol{v}$ on XZ (left) and XY (right) planes represented as $\boldsymbol{v}_{xz}$ and $\boldsymbol{v}_{xy}$, respectively, for three different volume fractions and system size $L/a = 64$. The color map represents the magnitude of the projected velocity normalized by the Stokes velocity, defined as, $|\boldsymbol{v}_{xz}|/V_s$ and $|\boldsymbol{v}_{xy}|/V_s$, where $\boldsymbol{v}_{xz} = (v_x, v_z)$ and $\boldsymbol{v}_{xy} = (v_x, v_y)$, whereas the arrows show the direction, defined as, $\boldsymbol{v}_{xz}/|\boldsymbol{v}_{xz}|$ and $\boldsymbol{v}_{xy}/|\boldsymbol{v}_{xy}|$.

the full range of volume fraction, in good agreement with Kuusela et al. [30], whereas Padding et al. [23] show the same qualitative but different quantitative behaviour mainly because of small system size and elongated periodic box. We have observed a sharp decrease in the relaxation times at $\phi > 0.3$ in both directions, caused by the ordering of the particles, whereas a jump in relaxation time at $\phi = 0.5$ could be because of very long range ordering of the particles and the artefacts generated from the use of a finite-width interface. In contrast to the present study, Nicolai et al. [5] didn't observe any decay behavior in the relaxation times.

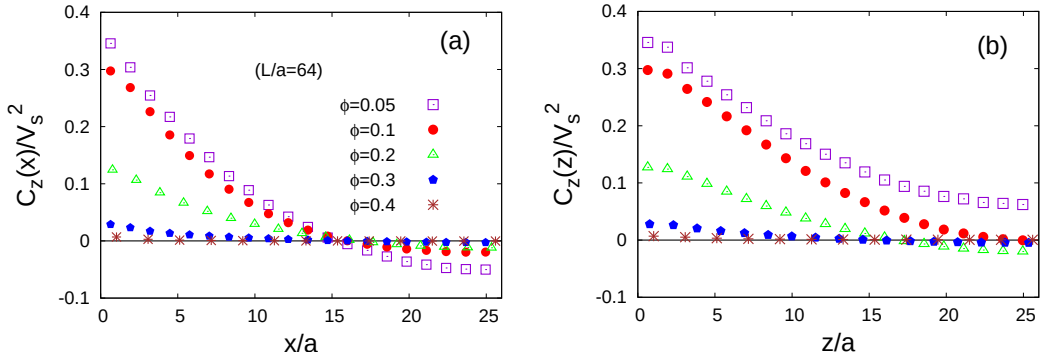

FIGURE 3.11: Spatial correlation function of velocity fluctuations of the z-component of the velocity normalized by the square of Stokes velocity as a function of the distance: "(a)" shows the spatial correlation function perpendicular to gravity and "(b)" shows the correlations parallel to gravity.

In order to understand this disagreement, we have to analyse Nicolai's results in the context of side wall effects. As explained in Chapter 1, Section 1.2 that side walls reduce the velocity fluctuations near its vicinity and particles affected by these walls should not be used. In contrast, Nicolai had not taken care of these side walls and particles affected by these walls are also included in the steady state analysis. Apart from the side wall effects, the cubic periodic box in our simulations is another reason for this discrepancy. According to Koch's theory [3], the relaxation time is reduced in an elongated box particularly in the direction of gravity, as cross-over effects are reduced. These effects are more pronounced at low volume fraction. If particle relaxation time is affected by the cross-over or periodic boundary effects, then the difference in vertical and horizontal relaxation times should decrease with the increase of volume fraction, as this reduces the cross-over effects . We have observed the decrease in the difference of relaxation times as shown in the inset of Fig. 3.9(b), which is consistent with our analysis. Hence, the discrepancy of our results from Nicolai partially comes from the side wall effects in Nicolai's study and partially from the cubic periodic box in our work.

The fluid in the vicinity of particles is shown to follow a swirling motion [9,13,52]. This motion induces the velocity fluctuations among the particles. In order to illustrate the swirling motion of the fluid (eddy formation), we projected the total velocity field $\boldsymbol{v}$ in XZ and XY planes represented as $\boldsymbol{v}_{xz}$ and $\boldsymbol{v}_{xy}$, respectively, for three different volume fractions in Fig. 3.10, for system size $L/a = 64$. The color map represents the magnitude of the projected velocity normalized by the Stokes velocity, defined as, $|\boldsymbol{v}_{xz}|/V_s$ and $|\boldsymbol{v}_{xy}|/V_s$, where $\boldsymbol{v}_{xz} = (v_x, v_z)$ and $\boldsymbol{v}_{xy} = (v_x, v_y)$, whereas the arrows show the direction, defined as, $\boldsymbol{v}_{xz}/|\boldsymbol{v}_{xz}|$ and $\boldsymbol{v}_{xy}/|\boldsymbol{v}_{xy}|$. Figure 3.10 shows the eddies of different sizes, which are more organized in the XZ plane due to the strong effects of gravity. A particle trapped in these eddies moves in a spiral motion, which in turn induces the fluctuations in the particle velocities in both directions. Figure 3.10 also shows that the size of eddies are reduced with the increase of volume fraction, in good agreement with Segre et al. [9]. We can also characterize the formation and size of swirls from the particle velocity fluctuations

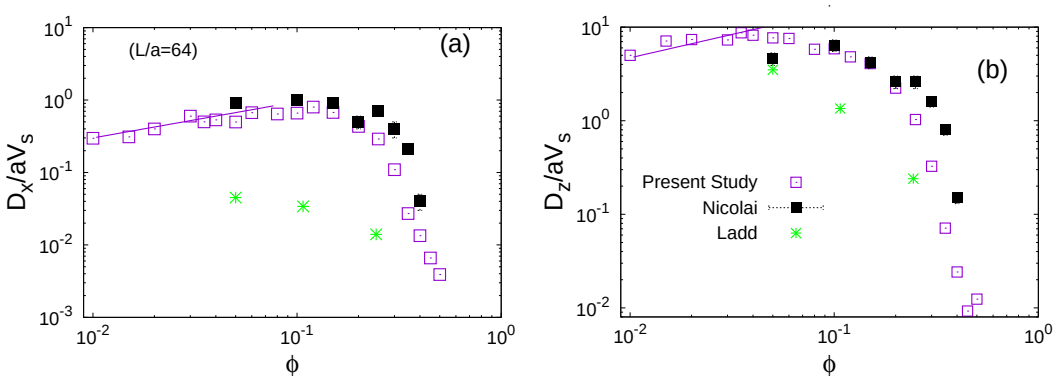

FIGURE 3.12: A comparison of the long time steady-state self-diffusion coefficients $D_\beta(\beta \in x,z)$, normalized by the product of particle radius a and Stokes velocity V_s with the experimental data of Nicolai [5] and simulation results of Ladd [18]. Figures "(a)" and "(b)" show the horizontal and vertical directions, respectively. Lines show the $\phi^{1/2}$ behavior

spatial correlation functions, as defined in Eq. (2.15). These correlations normalized by the square of the Stokes velocity are plotted in Fig. 3.11 for both vertical and horizontal directions. We define $C_z(z)$ and $C_z(x)$, with respect to the distance vector $\boldsymbol{r}$, in either the vertical $\boldsymbol{r} = z\boldsymbol{\delta}_z$ or horizontal $\boldsymbol{r} = x\boldsymbol{\delta}_x$ directions. Figure 3.11 shows that correlations in the vertical direction decay slower than those in the horizontal direction due to long ranged memory effects in the vertical direction. The correlations in the horizontal direction become negative before settling to zero and the minima of this is defined as the correlation length [9]. Unfortunately, we don't have the data beyond $L/a = 25$ due to periodic boundary conditions, but it already shows the unscreened behavior in both directions, in good agreement with the behavior shown by Segre [9]. In addition, a quantitatively small correlation value and rapid decay of these correlations at high volume fractions, confirm our argument of cluster formation.

3.3.4 Self-Diffusion

The particles subject to sedimentation colloid with neighbouring particles and undergo fluctuating motion, characteristic of a diffusion process. In order to quantify this diffusion, we calculated the self-diffusion from the slope of MSD in the x and z directions, as defined in Eqs. (2.12) and (2.12).

The saturated value of these diffusion coefficients ($D_\beta = \lim_{t\to\infty} D_\beta(t)$) normalized by the product of Stokes velocity and particle radius is plotted in Fig. 3.12, as a function of volume fraction. As with velocity fluctuations, we also observe that the D_z and D_x show a $\phi^{1/2}$ dependency at low volume fraction regime, in good agreement with the theoretical predictions [24, 36, 39]. Moreover, further increase in ϕ causes the decrease in vertical diffusion, whereas horizontal diffusion remains unchanged and then decreases sharply with increasing ϕ. At $\phi = 0.5$, diffusion in z direction shows an increase because of the large relaxation time caused by the long range ordering of the microstructure. Our data shows good agreement with Nicolai [5] at low and moderate

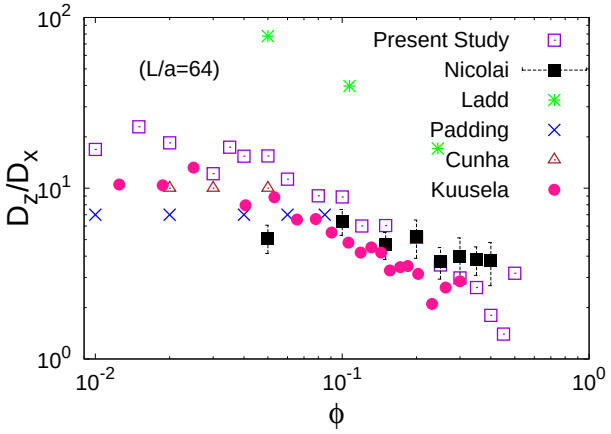

FIGURE 3.13: Comparison of the diffusion anisotropy with the experimental data of Nicolai [5] and simulation results of Ladd [18], Padding [23], Cunha [24] and Kuusela [47].

volume fractions, whereas a discrepancy is evident at high volume fractions regime. This discrepancy is the combination of side wall effects and poly-dispersity in experiments and cubic periodic box and finite system size in simulations. Brenner [39] has already shown the effects of side wall in experiments, whereas effects of poly-dispersity have been studied by Nguyen and Ladd [20]. These two factors have a significant impact on velocity fluctuations and their relaxation times. Moreover, as mentioned before, the cubic periodic box and finite system size also affect the velocity fluctuations and their relaxation times. Therefore, it is difficult to characterize the effects of the above mentioned parameters on particle diffusion, which depends both on velocity fluctuations and their relaxation times. A more detailed study is required to explore each of the above mentioned parameters, which requires large computational resources and is beyond the scope of the present study. In contrast to the present study, Ladd [18] has observed small values of the diffusion coefficients due to the small system size and full periodic boundary conditions.

In order to characterize the anisotropic nature of the sedimentation phenomena, we plotted the diffusion anisotropy, as a function of volume fraction in Fig. 3.13. Based on the diffusion scaling found in both directions, diffusion anisotropy should remain unchanged at low volume fraction, whereas our data show some fluctuations at low ϕ. At high volume fraction this anisotropy decreases with increasing ϕ. Our data shows a relatively large value of diffusion anisotropy at low volume fraction as compared to other studies, except for Ladd [18] which shows a large anisotropy due to the small system size used. This higher value in our study is mainly because of the cubic periodic box. The increase in the aspect ratio decreases the relaxation time, which in turn decreases the diffusion anisotropy. This causes a discrepancy with other studies [5, 18, 23, 24] at low volume fractions.

3.4 Concluding Remarks

In this Chapter, we presented the first detailed study of sedimentation of spherical particles, which covers the wide range of volume fraction from 0.01 to 0.5, using three different cubic periodic boxes of sizes $L/a = 16, 32$ and 64. We investigated the microstructure of the system and found that at low volume fraction, particles prefer to orient horizontally around a test particle and with increasing ϕ this preference decreases and at $\phi \gtrsim 0.15$ the microstructure becomes isotropic. We observed that at low ϕ, this anisotropic microstructure dominates the phenomena and at high ϕ many-body interactions determine the transport properties, whereas there is a cross-over, where both microstructure and many-body interactions try to dominate each other. In addition, we found the long range ordering of the microstructure at $\phi = 0.5$, which increased the relaxation times of velocity fluctuations. We found that velocity fluctuations show a $\phi^{1/2}$ dependency at low volume fraction due to the dependence on microstructure and then there is a cross-over and high volume fraction regimes, where these velocity fluctuations decreases with increasing ϕ. Our data showed good consistency with the well known experimental results of Nicolai et al. [5]. The relaxation times of velocity fluctuations show different behavior. The vertical relaxation time decays approximately as $\phi^{-1/2}$ in the full range of volume fractions, whereas horizontal relaxation time decays as $\phi^{-1/2}$ at low volume fractions.

The velocity fluctuations and their relaxation times lead us to define the dispersive motion of the particles and we calculated the steady state self-diffusion coefficients in both directions. We found that both the vertical and horizontal diffusion coefficients increase as $\phi^{1/2}$ at low volume fraction. Moreover, the horizontal diffusion coefficients show a plateau and then decreases sharply at high volume fractions, whereas the vertical diffusion decreases at high volume fraction regime. Our data shows good agreement with Nicolai et al. [5] Furthermore, we also calculate the diffusion anisotropy which shows a fluctuating behavior at low volume fraction and then decreases at high volume fraction regimes. We have found a relatively high anisotropy at low volume fraction mainly because of the cubic periodic box.

Chapter 4

Sedimentation at Finite Reynolds Number

4.1 Introduction

Most of the experimental [5,6,9,10,13], theoretical [1,3] and simulation [14,18,20,23–26,32,47] studies on sedimentation are focused in the Stokes regime, where theoretical aspects of the phenomena are rather developed, whereas little is known about the behavior of the suspension when fluid inertia is significant. This is because turbulent particle laden flows are difficult to investigate through experiments and simulations, as the former require sophisticated instrumentation and the latter enormous computational resources.

Due to the complexity of the phenomena, there are only a few studies, focused at moderate Re suspensions [1, 40, 45, 52, 97]. Koch et al. [1, 40, 45] have performed LBM simulations, which deal mostly with the microsturcture and theoretical aspects of the phenomena, whereas Climent et al. [52] used an approximate numerical method, where the particle velocity is calculated by averaging the fluid velocity in a Gaussian envelop to investigate the sedimentation at finite Re. The complex and perplexing nature of the phenomena at moderate Re makes it really hard to investigate through theory, experiments and simulations.

As mentioned above, most of the studies are in the Stokes regime, having a particle diameter based Reynolds number, $\mathrm{Re} = \rho_\mathrm{f} \mathrm{V_t} \sigma / \eta$ less than one, where V_t is the terminal velocity of a single particle. At low Re, where inertia can be ignored, the Navier-Stokes equations (NS) are reduced to a linear set of equations and are easy to tackle computationally, whereas with the introduction of appreciable inertia, the treatment of the nonlinear equations that govern the flow is very difficult and requires abundant computational resources. Computational schemes which use unstructured meshes [98] usually provide good results in the Stokes regime, whereas

at finite Re, these require very heavy computational resources because of the fast phenomenological changes. Hence, it is generally widely believed that the best way to investigate the non-equilibrium properties of a suspension with appreciable inertia is through DNS, with a fixed grid around the particles.

In this Chapter, we investigated the effects of moderate/finite Re on the microstructure, average sedimentation velocity, velocity fluctuations and self-diffusion in a steady state homogeneous suspension of non-Brownian sedimenting particles over a wide range of volume fraction from 0.01 to 0.4. Previous studies of this dissertation were based in the Stokes regime (Re $\lesssim$ 0.3), where inertial effects can be ignored, whereas in this study the particle Re varies from 0.05 to 10. We organized this work in such a way that we could test the effect of Re at the low, moderate and high volume fraction regimes.

In this Chapter, Section 4.2 explains the simulation parameters and results are presented in Section 4.4, where we investigated the evolution of microstructure in Section 4.4.3, velocity fluctuations and their relaxation times in Section 4.4.4 and self-diffusion in Section 4.4.5. We conclude our study in Section 4.5.

4.2 Simulation Parameters

In order to study the inertial effects, we varied Re from 0.05 to 10 by increasing the gravity. In principal, we can go beyond Re=10, but we have to reduce the time step to a much smaller value and need to refine the mesh as well, which require enormous computer resources and is beyond the scope of this study. A cubic periodic box of dimension $L/a = 32$ is used, where the particle radius is kept constant at 4Δ and the interface thickness is set to unity in the unit of grid spacing Δ in all simulations. Gravity was introduced in the $-z$ direction. We set the particle to fluid density ratio to 5 and fluid density equal to one. Direct interparticle interactions are introduced by a Weeks-Chandler-Andersen (WCA) type potential with powers of 36:18, as defined in Eq. (1.4). Simulations are run for 1000-1500t_t; sufficient to yield statistically meaningful data for this analysis, where t_t denotes the terminal time ($t_t = a/V_t$).

In order to characterize the accuracy of our method, we calculated the drag coefficient of an isolated sphere and compared it with an empirical relation [99], as shown in Fig. 4.1. The drag coefficient C_D is defined as,

$$C_D = \frac{24}{Re}[1 + 0.1315 Re^{0.82 - 0.05 \log_{10} Re}]. \quad 0.01 < Re < 20 \tag{4.1}$$

In order to simulate this test case, we used the same scheme as adopted by Koch et al. [45]. Since our input parameter in the simulations is gravity (g), we first fix the particle Re and calculated the respective Archimedes number (the ratio of gravitational to viscous force) from Eq. (4.2)

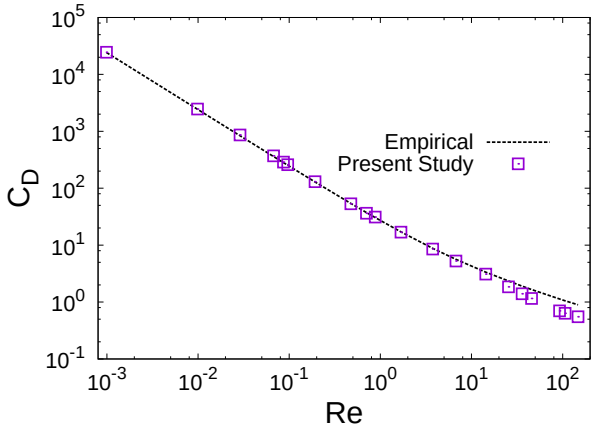

FIGURE 4.1: Drag coefficient of an isolated sphere as a function of particle Reynolds number.

as,

$$\mathrm{Ar} = 18\mathrm{Re}[1 + 0.1315\mathrm{Re}^{0.82-0.05\log_{10}\mathrm{Re}}]. \quad 0.01 < \mathrm{Re} < 20 \tag{4.2}$$

From Archimedes number (Ar), we calculated our input parameter g as $\mathrm{Ar} = \rho_\mathrm{f}(\rho_\mathrm{p} - \rho_\mathrm{f})\mathrm{g}\sigma^3/\eta^2$ and run the simulations for long time until steady state terminal velocity is achieved. From this terminal velocity, we calculated the Re and then $\mathrm{C_D}$ from Eq. (4.1). Thereafter, we compared the C_D from the simulations with the empirical relation in Fig. 4.1. It shows a good agreement with the empirical relation up to Re=14, whereas a deviation is evident at $\mathrm{Re} > 14$. In principal, we can enhance the accuracy at high Re as well, but this require enormous computer resources. Using the simulation parameters for a single particle, we simulated multiple spheres in a periodic cubic cell.

4.3 Drafting-Kissing-Tumbling Mechanism

Before discussing our main results, we investigated the DKT mechanism for particle pair interactions by simulating two interacting particles. We place particles one above the other, making sure that the trailing particle is in the wake of the leading particle. We calculated the distance between the particles in all three directions Δr_β, where $\beta \in x, y, z$ and plotted it as a function of the terminal time for three different Re, as shown in Fig. 4.2. The vertical distance between the particles decreases initially, showing the drafting of the trailing particle, as it experiences a low pressure due to the wake of the leading particle. After drafting, the two particles interact with each other, which is the kissing phase, which can be seen through the plateau in all three figures at a vertical distance equal to σ. After kissing phase, the lift force or the source flow sweep the particle to horizontal orientation, which is the tumbling phase. The horizontal distance between the particles increases in the tumbling phase, whereas vertical distance falls to zero. We have divided these three figures in three section to highlight the DKT mechanism, where "D" shows

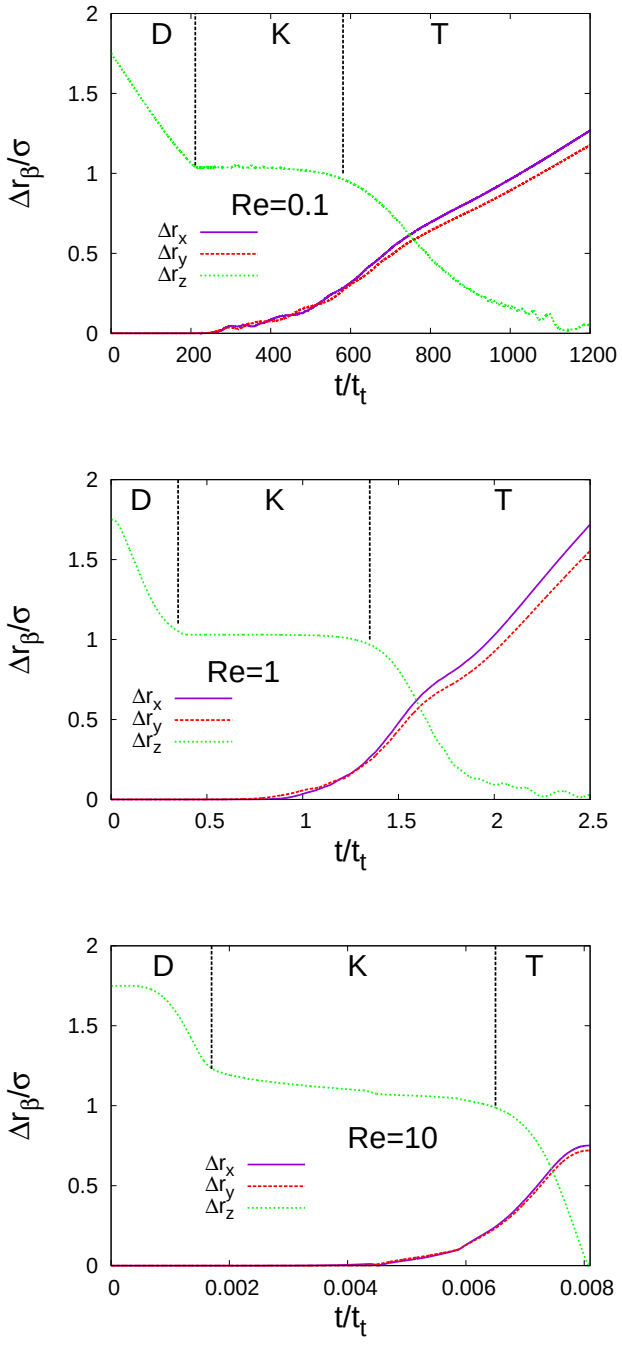

FIGURE 4.2: Distance between two particles in all three directions Δr_β, where $\beta \in x,y,z$, as a function of terminal time for three different Re. These three figures are divided into three sections, where "D" shows the drafting, "K" shows the kissing and "T" shows the tumbling phase of the DKT mechanism.

the drafting, "K" shows the kissing and "T" shows the tumbling phase. We can also see that the time required to undergo DKT type interaction decreases tremendously as Re is increased, which shows the fast phenomenological changes at high Re. In order to capture such a fast change, one has to use very sophisticated instruments in experiments and a very small time step and a refined mesh in simulations. This is why most of the experimental and simulation studies

on sedimentation are in the Stokes regime.

4.4 Results and Discussion

4.4.1 Hindered Settling

A particle settling in the vicinity of other particles experiences a hindered settling due to the drag force induced by the fluid back flow and the particle-particle interactions. Consequently, it reduces the average sedimentation velocity of the suspension with respect to the terminal velocity of an isolated particle. The effect of fluid back flow and particle particle interaction is very small at low volume fractions, whereas both of these effects increase with increasing volume fraction. We computed the average sedimentation velocity V_{sed} of the suspension and compared it with the theoretical [35, 91–93, 95], experimental [5] and simulation results [23, 52], as shown in Fig. 4.3, for different Re, where $V_{\text{sed}} = \langle V_{iz} \rangle$. Figure 4.3(a) shows that the average sedimentation velocity, normalized by the terminal velocity, decreases with the increase of volume fraction due to this hindered settling. The decay of V_{sed} as a function of volume fraction at Re=0.05 and 0.1 is same both qualitatively and quantitatively, which shows the weak inertial effects. In contrast, at Re ≥ 0.5, a decrease in V_{sed} is evident with the increase of Re due to enhanced inertial effects, which are more pronounced at low volume fractions. This decrease in V_{sed} is attributed to two factors: (1) fast DKT mechanism at high Re, where a particle spends less time in the wake of another particle as compared to low Re, which decreases the average sedimentation velocity of the particles; (2) particles are cross stream oriented and feel the full effects of fluid back flow at high Re, which also decreases the average sedimentation velocity. At high volume fractions, the inertial effects are suppressed by the increasing number of particles and the average sedimentation velocity at high volume fraction is independent of Re, as shown in Fig. 4.3(a). We compared our results for Re ≤ 0.5 with other studies in Fig. 4.3(b). Batchelor [35] was the first who found the effect of the particle volume fraction on the average sedimentation velocity by assuming a uniform distribution in the separation of pairs of spheres and ignoring the fluid back flow effects, which is valid only for low volume fraction, as evident in Fig. 4.3(b). This hindered settling in the Stokes regime is well described by the Richardson and Zaki [91] power law, $V_{\text{sed}}/V_{\text{t}} = (1-\phi)^n$, where the power law exponent n varies from 4.7 to 6.55 depending on the studies [5, 23, 24, 52, 92, 95]. In our study the best suited exponent is 5.3, well within these two extremes for Re=0.05 and 0.1, as shown in Fig. 4.3(b). A small deviation from the theoretical prediction for the Stokes regime is evident at Re=0.5 for low volume fractions, showing the onset of inertial effects.

Figures 4.3(c) and (d) show that the theoretical predictions for the Stokes regime are no longer applicable when inertial effects are relevant, rather a modified expression [95] of the form,

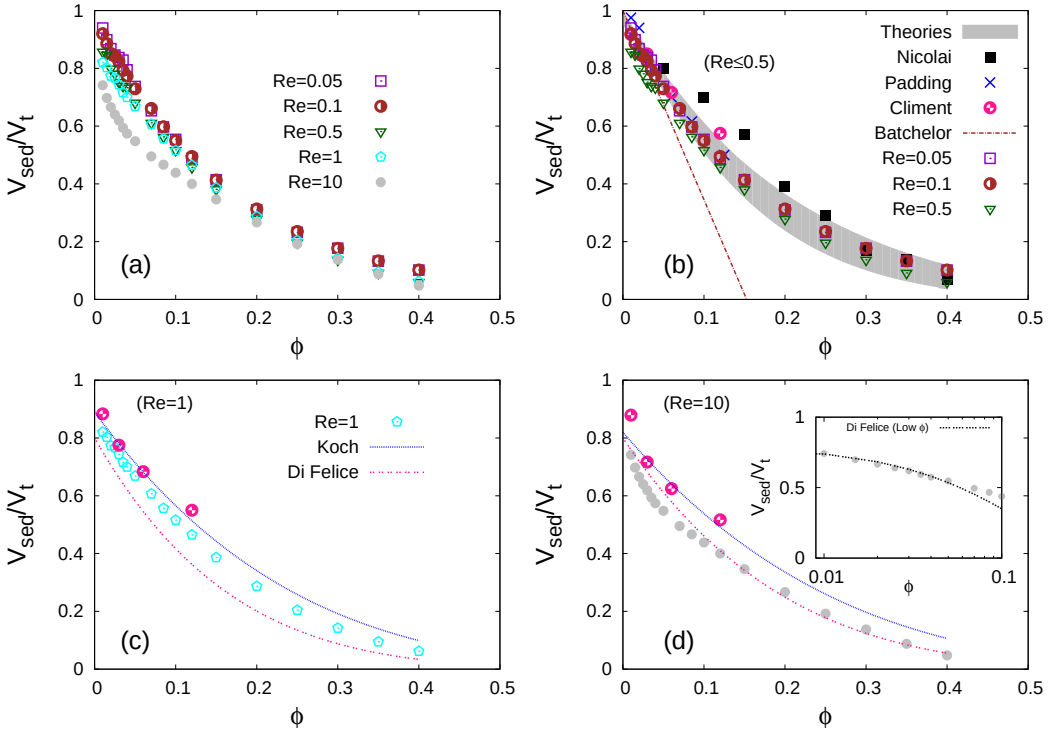

FIGURE 4.3: Average sedimentation velocity V_{sed} of particles normalized by the terminal velocity V_t of an isolated sphere, as a function of volume fraction for different Re. Theoretical predictions [35,91–93,95] are represented with shaded region, except for Batchelor [35] which is represented with the line, whereas points show the experimental dat of Nicolai [5] and simulation data of Padding [23] and Climent [52]. Figure "a" shows the comparison of V_{sed} for all Re, whereas "b" shows the results for Re ≤ 0.5 to highlight the Stokes regime behavior. Figures "c" and "d" show the comparison of V_{sed} with the theoretical predictions of Koch [45] and Di Felice [95] for Re=1 and Re=10, respectively. The value k is 0.89 and 0.82 for Re=1 and 10 respectively, for Koch and value of n is found from Eq. 4.3. Similarly, the value k for Di Felice is 0.81 and n is found from Eq. 4.4. Figure inset shows the low concentration behvior at Re=10. Legends mentioned in above figure apply to all sub figures.

$V_{sed}/V_t = k(1-\phi)^n$ provides a better solution, where the value of the prefactor k and the exponent n varies with the particle Re. Koch et al. [45], found in their simulation study that the values of k for Re=1 and 10 are 0.92±0.03 and 0.86±0.04, respectively, and suggested a quadratic polynomial expression for the value of n of the form,

$$n = 4.23 - 0.0526\mathrm{Re} + 0.00111\mathrm{Re}^2. \tag{4.3}$$

Furthermore, they also took into account the effects of periodic boundary conditions. Similary, Di Felice [95] found a value of $k \approx 0.81$ at intermediate Re in their experimental study and suggested an expression for n of the form,

$$\frac{6.5-n}{n-3} = 0.1\mathrm{Re}^{0.74}. \tag{4.4}$$

The value of k is found by fitting the data and it ranges from 0.8 to 0.95 in the literature [45, 95, 100–102]. We have compared our results with the Koch and Di Felice expressions in Figs. 4.3(c) and (d) for Re=1 and 10, respectively. At Re=1, our data shows a trend well in between these two expressions, whereas at Re=10, our data shows a good agreement with Di Felice, deviating at small volume fraction. Di Felice also suggested that the value of the exponent n at low ϕ is 1.5 times the corresponding value from Eq. 4.4 at Re > 1, denoted as n^*. We plotted the low concentration data in the inset of Fig. 4.3(d) and compared with the Di Felice expression by using n^* in Eq. 4.4 at Re=10. Our data shows a good agreement with Di Felice at low volume fractions ($\phi \leq 0.05$). As explained earlier, the rapid decay of average sedimentation velocity at low ϕ and Re=10 is attributed to the strong influence of the anisotropic microstructure [45] which will be explained later, having pronounced effects at high Re. At low ϕ and high Re, a particle is deficit of neighboring particles, due to the DKT mechanism [45]. This mechanism makes the spheres well separated, having a cross-stream orientation. These well separated particles feel the full effect of the fluid back flow, which in turn causes a rapid decay in the sedimentation velocity. As the concentration of particles increases, this mechanism competes with the many body interactions and as the latter overpower the phenomena, the rate of decrease slows down. Koch showed that this rate slows down at $\phi = 0.05$ at Re=10 and our data also shows a similar trend, as evident in the inset of Fig. 4.3(b).

A small deviation of our results from the Koch et al. and Di Felice is because of the finite size effects in our simulations. Furthermore, Di Felice used a large system size in their experimental study and suggested a constant value [100] of k, which is against the spirit of the phenomena at finite Re, as increase in the Re, decreases the settling velocity so the value of k should also decrease, as confirmed in the simulations of Koch [45], which also cause the deviation from our results.

4.4.2 Fluid Behavior

Before discussing the particle properties, we would like to look at the fluid behavior around a particle at different Re. At low Re in the Stokes regime, it is well established that the fluid has a fore-aft symmetry around a particle, whereas at high Re, fluid inertia breaks this symmetric behavior.

We calculate the fluid velocity as a function of position and time denoted as $\boldsymbol{v}_{\mathrm{f}}(\boldsymbol{x},t)$. In order to look at the fluid around the particle in cylindrical coordinates, we shifted the origin at the particle position as, $\boldsymbol{u}_{\mathrm{f}}(r_{\mathrm{cyl}},z) = \langle \boldsymbol{v}_{\mathrm{f}}(\boldsymbol{r}) \rangle$, where $\boldsymbol{r} = \boldsymbol{x} - \boldsymbol{R}_i$, is the position vector of the fluid from the particle in which $\boldsymbol{x}$ and $\boldsymbol{R}_i$ show the positions of fluid and particle, respectively, and averaged over time, number of particles and angular coordinate θ. If r^x, r^y and r^z are the components of $\boldsymbol{r}$ in the Cartesian coordinates, then $r_{\mathrm{cyl}} = \sqrt{(r^x)^2 + (r^y)^2}$, $\theta = \arctan(r^y/r^x)$ and $z = r^z$. In order to characterize the asymmetric behavior of fluid before (B) and after (A) the particle, we plotted

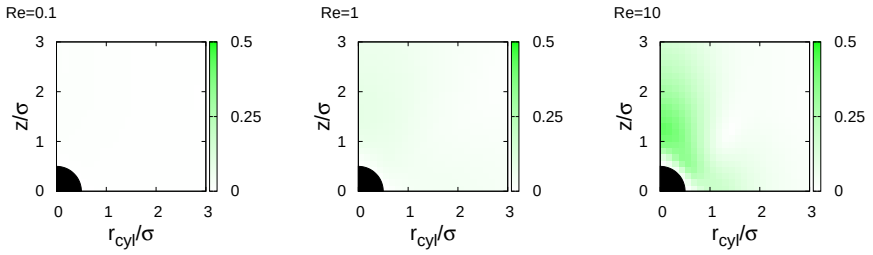

(a) $\phi = 0.025$

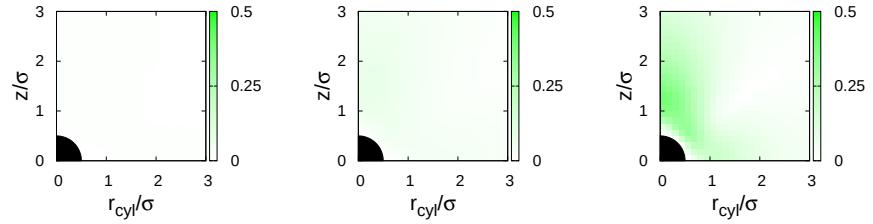

(b) $\phi = 0.04$

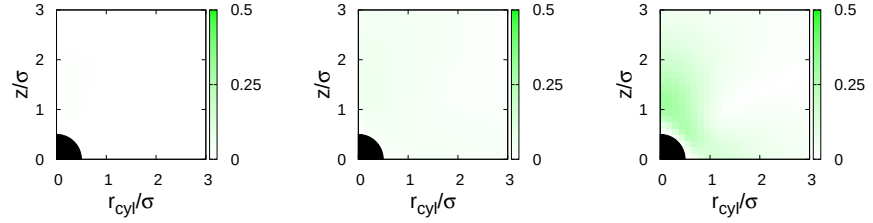

(c) $\phi = 0.07$

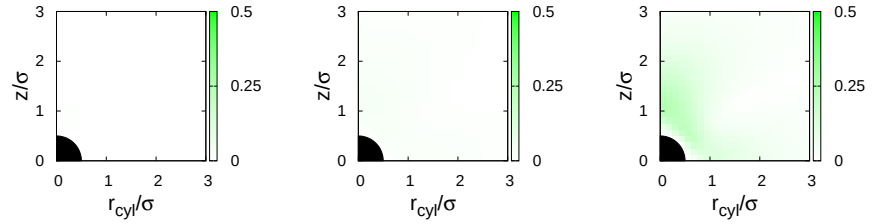

(d) $\phi = 0.1$

FIGURE 4.4: The absolute value of the difference in the fluid velocity before (B) and after (A) the particle $|\Delta \boldsymbol{u}_{\mathrm{f}}^{\mathrm{AB}}(r_{\mathrm{cyl}},z)| = |\boldsymbol{u}_{\mathrm{f}}^{\mathrm{A}}(r_{\mathrm{cyl}},z) - \boldsymbol{u}_{\mathrm{f}}^{\mathrm{B}}(r_{\mathrm{cyl}},z)|/V_{\mathrm{sed}}$, in cylindrical coordinates. Figures "(a)", "(b)", "(c)" and "(d)" show this difference at $\phi = 0.025$, 0.04, 0.07 and 0.1, respectively, for different Re.

$|\Delta \boldsymbol{u}_{\mathrm{f}}^{\mathrm{AB}}(r_{\mathrm{cyl}},z)| = |\boldsymbol{u}_{\mathrm{f}}^{\mathrm{A}}(r_{\mathrm{cyl}},z) - \boldsymbol{u}_{\mathrm{f}}^{\mathrm{B}}(r_{\mathrm{cyl}},z)|/V_{\mathrm{sed}}$, in Fig. 4.4. The fluid velocities before and after the particle are defined in term of their components as, $\boldsymbol{u}_{\mathrm{f}}^{\mathrm{A}}(r_{\mathrm{cyl}},z) = [u_{\mathrm{f}}^{r_{\mathrm{cyl}}}(r_{\mathrm{cyl}},z), u_{\mathrm{f}}^{z}(r_{\mathrm{cyl}},z)]$ and $\boldsymbol{u}_{\mathrm{f}}^{\mathrm{B}}(r_{\mathrm{cyl}},z) = [-u_{\mathrm{f}}^{r_{\mathrm{cyl}}}(r_{\mathrm{cyl}},-z), u_{\mathrm{f}}^{z},(r_{\mathrm{cyl}},-z)]$, respectively, for $z \geq 0$. Figures 4.4(a), (b) (c) and and (d) show this difference at $\phi = 0.025$, 0.04 , 0.07 and 0.1, respectively, for Re=0.1, 1, 10. By comparing these plots from left to right for different Re at a particular ϕ, we found that Re=0.1 shows a symmetric behavior, whereas with increasing Re the difference between the velocities after and before the particle increases, showing the effects of the fluid inertia. If we compare these figures from top to bottom for Re=1 and 10 for different ϕ, it is evident that

the inertial effects are suppressed with the increase of particle volume fraction, caused by the presence of more number of particles. Figure 4.4 clarifies the asymmetric behavior of the fluid

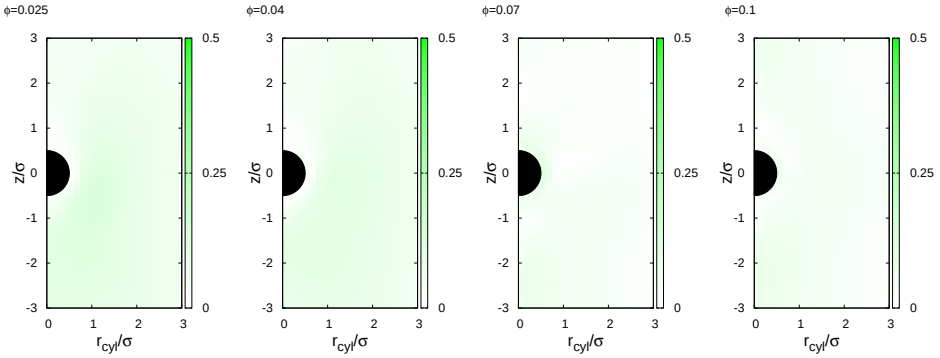

(a) Re = 1

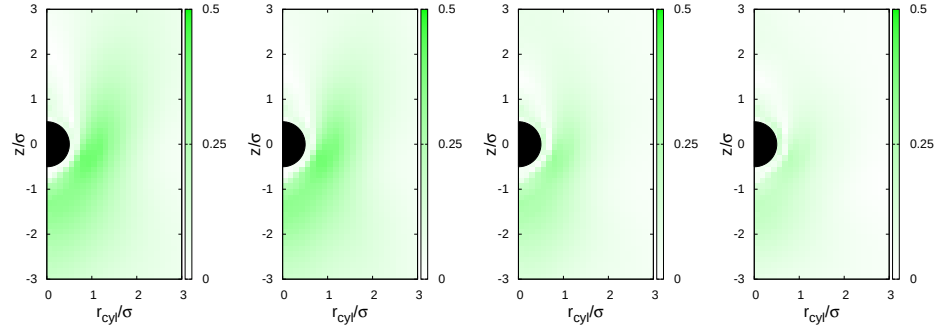

(b) Re = 10

FIGURE 4.5: The absolute value of the difference in the fluid velocity at Re=1 and 10 with the Re=0.1 as, $|\,\Delta \boldsymbol{u}_{\mathrm{f}}^{\mathrm{Re}=\gamma}(r_{\mathrm{cyl}},z)\,| = |\,\frac{\boldsymbol{u}_{\mathrm{f}}^{\mathrm{Re}=\gamma}(r_{\mathrm{cyl}},z)}{V_{\mathrm{sed}}^{\mathrm{Re}=\gamma}} - \frac{\boldsymbol{u}_{\mathrm{f}}^{\mathrm{Re}=0.1}(r_{\mathrm{cyl}},z)}{V_{\mathrm{sed}}^{\mathrm{Re}=0.1}}\,|$, for different ϕ, where $\gamma \in 1, 10$.

before and after the particle and to get a more insightful picture of the fluid behavior, we also plotted the difference of velocities at Re=1 and 10 with respect to the corresponding velocity at Re=0.1 as, $|\,\Delta \boldsymbol{u}_{\mathrm{f}}^{\mathrm{Re}=\gamma}(r_{\mathrm{cyl}},z)\,| = |\,\frac{\boldsymbol{u}_{\mathrm{f}}^{\mathrm{Re}=\gamma}(r_{\mathrm{cyl}},z)}{V_{\mathrm{sed}}^{\mathrm{Re}=\gamma}} - \frac{\boldsymbol{u}_{\mathrm{f}}^{\mathrm{Re}=0.1}(r_{\mathrm{cyl}},z)}{V_{\mathrm{sed}}^{\mathrm{Re}=0.1}}\,|$, in Fig. 4.5 for different ϕ, where $\gamma \in 1, 10$. Comparing Figs. 4.5(a) and (b) from left to right reveal that this difference decreases with the increase of particle volume fraction, as the increased packing of particles suppresses the effects of fluid inertia. Similarly, comparing figures from top to bottom reveal that this difference increases with the increase of Re. Furthermore, this difference is stronger before than after the particle at Re=10. If we look at the rear end of the particle at Re=10 in Fig. 4.5(b) this difference is almost negligible, whereas at the radial distance σ to 2σ the difference in the velocities is stronger because of the strong inertia of the fluid.

The fluid behavior around a particle has a great importance in the determination of the particle configuration and their transport properties. As it is shown that at high Re, normalized velocities are stronger, hence this strong behavior will push away the nearby particles. The effects of this asymmetric behavior of the fluid before and after the particle on the particle configuration is discussed in the next section.

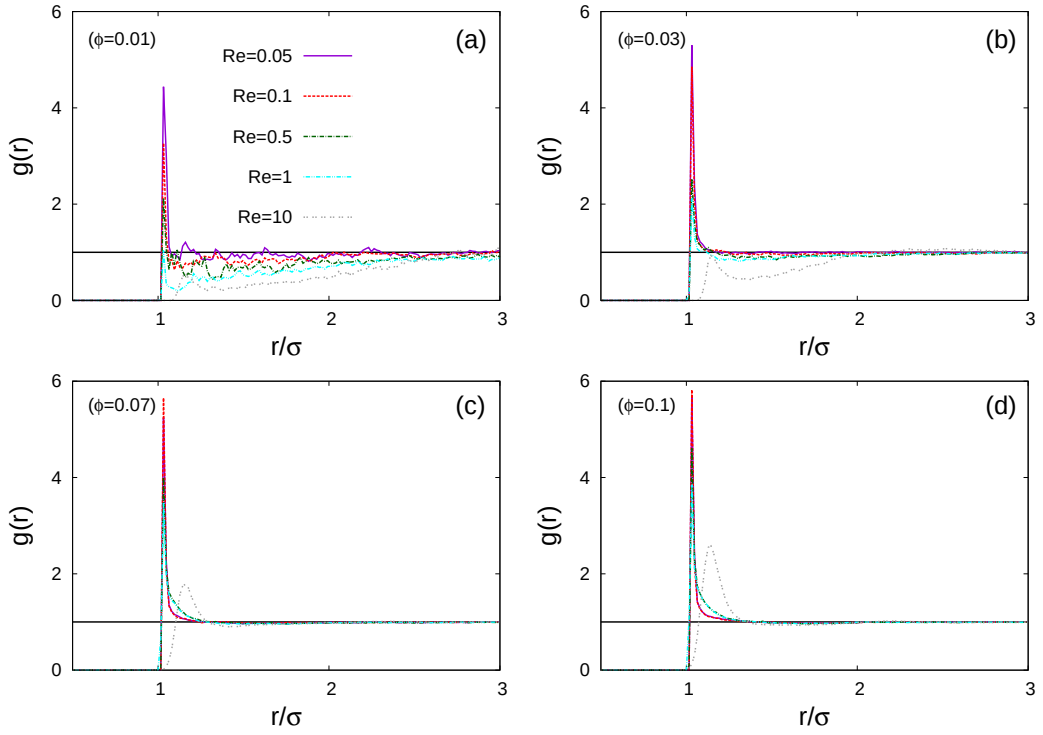

FIGURE 4.6: Radial distribution function as a function of radial distance for different Re at four different volume fraction.

4.4.3 Microstructure

The microstructure of the particles strongly affects the transport properties of the suspension. Like in Chapter 2 and 3, we explored the evolution of the microstructure with Re and volume fraction and its effects on transport properties. In order to have an idea of the average accumulation of the particles around a test particle in a shell, we calculated RDF $(g(r))$ based on Eq. (2.1), as shown in Fig. 4.6. We plotted the RDF for different volume fractions at different Re. For $\phi = 0.01$ and $\mathrm{Re} \leq 0.1$, the RDF shows a distribution typical of hard spheres, whereas at $\mathrm{Re} \geq 0.5$, the RDF shows the deficiency of neighbouring particles and this deficiency increases with increasing Re, in good agreement with Koch [45]. As ϕ is increased the deficit is decreased and at $\phi = 0.03$ and $\mathrm{Re} \leq 1$, particles already show the typical hard sphere distribution, whereas at Re=10, the deficit of particle pairs is still apparent, as shown in Fig. 4.6(b). With a further increase in volume fraction, particles start showing the RDF of a hard sphere distribution, as shown in Figs. 4.6(c) and (d). The increase in particle inertia at $\mathrm{Re} \geq 1$ not only induced the significant deficit of the particle pairs but it also shifted the peak and this shift decreases with the increase of volume fraction, as evident in Fig. 4.6.

The RDF provides the useful information of the particle deficiency and the shift in the peak with increasing Re, but it does not give any information about the particular direction where this deficiency exists. In order to find this preference, we calculated the pair distribution function in

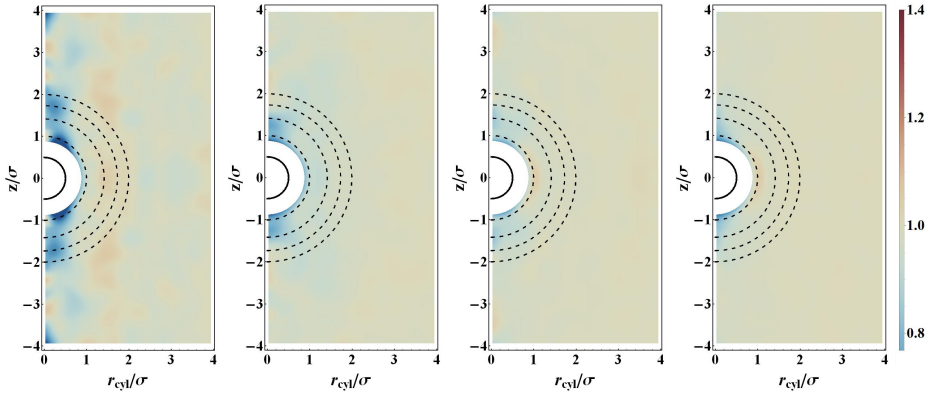

(a) $\phi = 0.01$ (b) $\phi = 0.02$ (c) $\phi = 0.03$ (d) $\phi = 0.05$

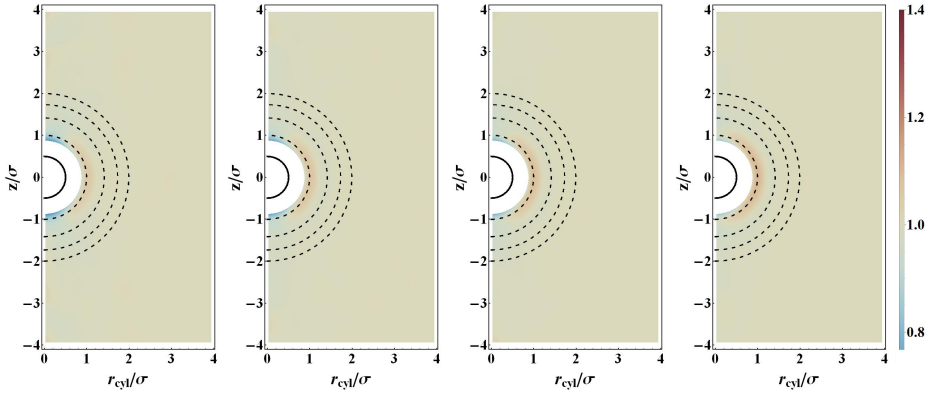

(f) $\phi = 0.07$ (g) $\phi = 0.1$ (h) $\phi = 0.12$ (i) $\phi = 0.15$

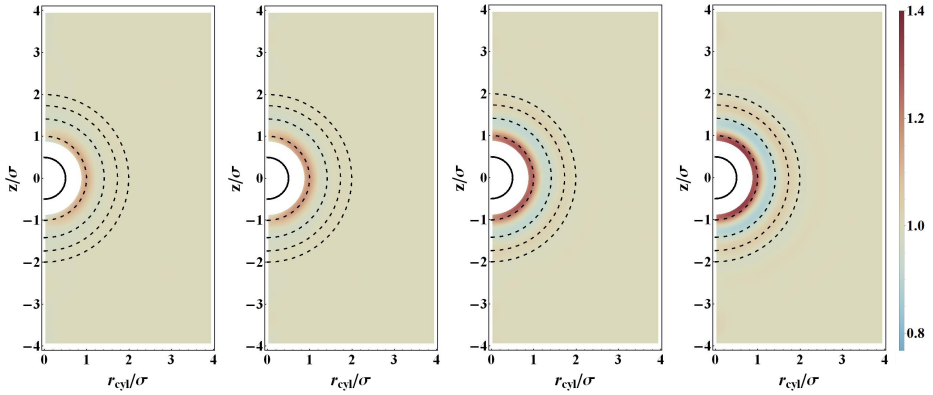

(k) $\phi = 0.2$ (l) $\phi = 0.25$ (m) $\phi = 0.35$ (n) $\phi = 0.4$

FIGURE 4.7: pair distribution function of particles in cylindrical coordinates ($g\left(r_{\text{cyl}}, z\right)$) for Re=0.1.

cylindrical coordinates $g\left(r_{\text{cyl}}, z\right)$, for three different Re, as shown in Figs. 4.7, 4.8 and 4.9. Figure 4.7 shows the non-Brownian distribution, similar to Fig. 3.4, where particles show the preference to orient themselves in a horizontal position with respect to a test particle and this preference decreases with increasing volume fraction. At $\phi \geq 0.15$, the microstructure is isotropic. At Re=1, PDF in cylindrical coordinates shows the deficit of particle pairs and this deficit is more pronounced in the vertical direction, as shown in Fig. 4.8.

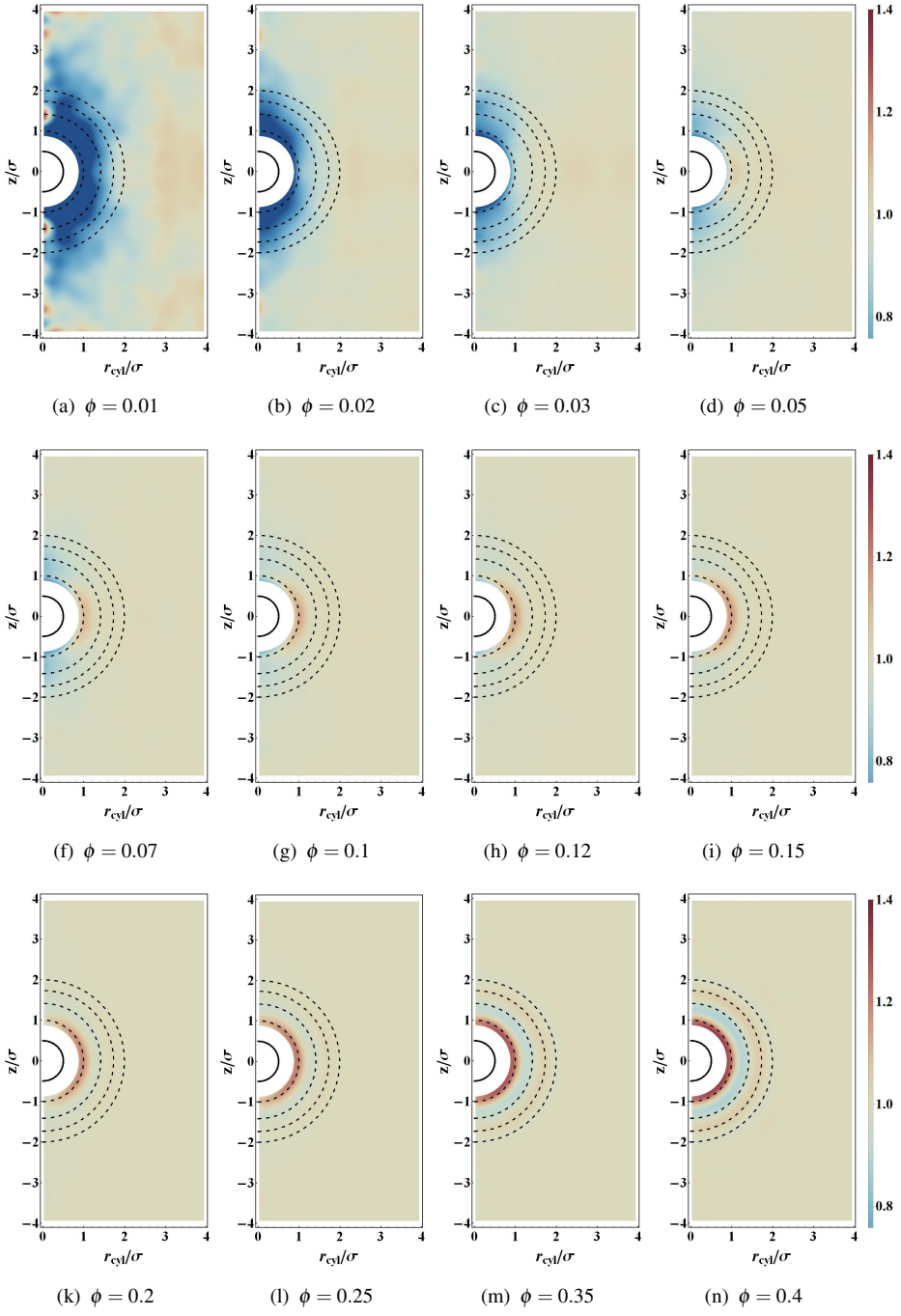

(a) $\phi = 0.01$ (b) $\phi = 0.02$ (c) $\phi = 0.03$ (d) $\phi = 0.05$

(f) $\phi = 0.07$ (g) $\phi = 0.1$ (h) $\phi = 0.12$ (i) $\phi = 0.15$

(k) $\phi = 0.2$ (l) $\phi = 0.25$ (m) $\phi = 0.35$ (n) $\phi = 0.4$

FIGURE 4.8: pair distribution function of particles in cylindrical coordinates ($g\left(r_{\text{cyl}}, z\right)$) Re=1.

At Re=10, PDF in cylindrical coordinates shows the deficit of particle pairs and this deficiency is stronger than the one at Re=1, in both directions. Compared to Re=1, PDF in cylindrical coordinates at Re=10 shows that the preference of particles in horizontal direction is stronger and shift in the peak is also evident. At high volume fraction $\phi \gtrsim 0.15$, an isotropic microstructure is visible. The comparative analysis of these maps revealed that with the increase of Re, the DKT mechanism grows stronger and its effects is felt over a larger volume fraction range. It is also evident from this microstructure analysis that deficit of particles is more stronger in the

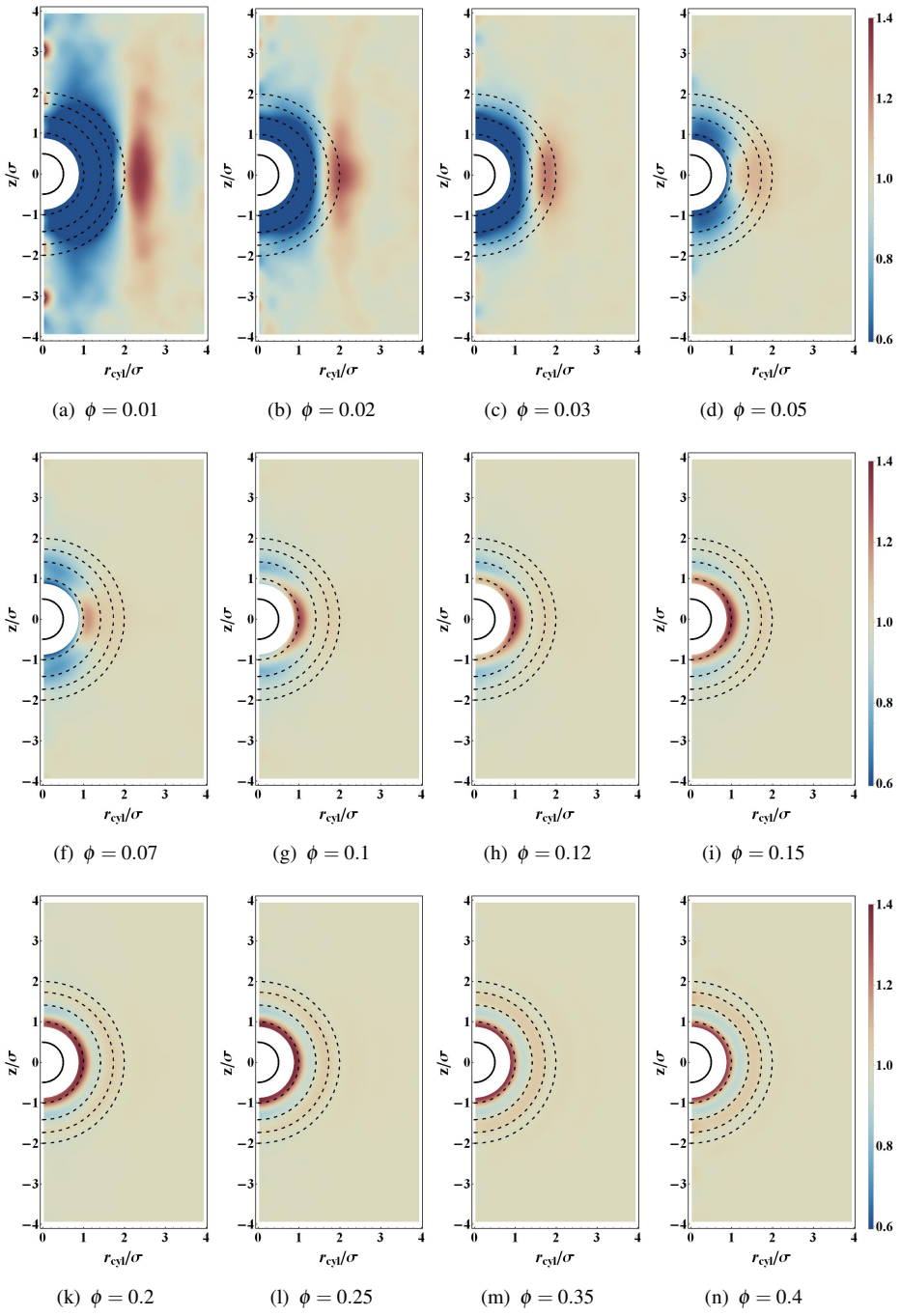

(a) $\phi = 0.01$ (b) $\phi = 0.02$ (c) $\phi = 0.03$ (d) $\phi = 0.05$

(f) $\phi = 0.07$ (g) $\phi = 0.1$ (h) $\phi = 0.12$ (i) $\phi = 0.15$

(k) $\phi = 0.2$ (l) $\phi = 0.25$ (m) $\phi = 0.35$ (n) $\phi = 0.4$

FIGURE 4.9: pair distribution function of particles in cylindrical coordinates ($g\left(r_{\mathrm{cyl}}, z\right)$) for Re=10.

vertical direction than the horizontal direction at all Re. This is because, a particle in the wake of a leading particle experiences a DKT type interaction, which leads the particle to horizontal orientation, whereas a horizontally orientated particle faces the source flow, which keeps the particle in the horizontal orientation as well. Hence, a preferred position of a particle is horizontal, which make the deficit stronger in the vertical direction, until many-body interactions suppress this DKT type interaction and make the microstructure isotropic.

The change in the microstructure of the particles at high Re is in accordance with the fluid behavior at high Re. The large difference of the fluid velocity at high Re with respect to Re=0.1, pushed the particle away from a given particle and created a deficiency near the given particle and DKT type interactions orient the particle pairs horizontally. Since this difference in fluid velocity is increased with the the increase of Re, which pushed the particle further away from a given particle and created the deficiency of the particle pairs in the near vicinity. The range of radial distance over which this deficiency is evident increased with the increasing Re due to the strong fluid velocity. Moreover, the range of volume fraction which showed this difference in fluid velocity is also increased with the the increase of Re, which in turn increase the range of volume fraction which shows the deficiency of nearby particles.

4.4.4 Velocity Fluctuations

The velocity fluctuations induced by HIs are quantified both in the parallel and perpendicular to gravity by its root mean square value as, $\Delta V_{\mathrm{H}}^{z} = \sqrt{\langle [V_{iz} - V_{\mathrm{sed}}]^2 \rangle}$ and $\Delta V_{\mathrm{H}}^{x} = \sqrt{\langle V_{ix}^2 \rangle}$, respectively. These velocity fluctuations are plotted in Fig. 4.10, as a function of particle volume fraction for different Re. For Re ≤ 0.5, velocity fluctuations in both directions show the Stokes regime characteristics discussed in previous Chapters: they scale as $\phi^{1/2}$ at low volume fraction regime ($\phi \lesssim 0.04$), remain unchanged at moderate volume fractions ($0.04 < \phi \lesssim 0.12$) and decrease sharply at high volume fraction regimes, in good agreement with other studies [5, 9, 23, 52]. At Re=1, vertical velocity fluctuations are decreased, whereas horizontal velocity fluctuations still show the Stokes regime behavior. The behavior of velocity fluctuations in both directions are in accordance with the microstructure changes, where deficit of particles is observed in the vertical direction, whereas there was no significant deficiency of particles in the horizontal direction, as shown in Fig. 4.8. At Re=10, with the enhanced inertial force effects, both vertical and horizontal velocity fluctuations are decreased, due to a pronounced DKT mechanism, which caused the significant deficit of the particles (Fig. 4.9) in both directions. Apart from the decrease in the velocity fluctuations, the range of volume fraction affected by an increase in Re is also increased. At Re=1, this range is increased up to $\phi \lesssim 0.07$, whereas at Re=10, it is up to $\phi \lesssim 0.12$, as evident in Figs. 4.10(c) and (d). This increase in the range is caused by the deficit of the neighbouring particles in the vicinity of a test particle, which increases with increasing Re, before many body interactions suppress the effects of inertial forces and the microstructure is similar to the Stokes regime microstructure.

The vertical and horizontal relaxation times decrease with the increase of volume fraction for all Re. These relaxation times are calculated as, $\tau_{\mathrm{H}}^{\beta} = [1/C_{\beta}(0)] \int_0^{\infty} C_{\beta}(t) dt$, where $\beta \in x, z$ and $C_{\beta}(t)$ is defined in Eqs. (2.2) and (2.3). The integration is performed from zero to the time at which these correlations start to oscillate around zero. The horizontal relaxation times at low volume fraction increase with the increase of Re. At high volume fractions and Re ≤ 1 horizontal

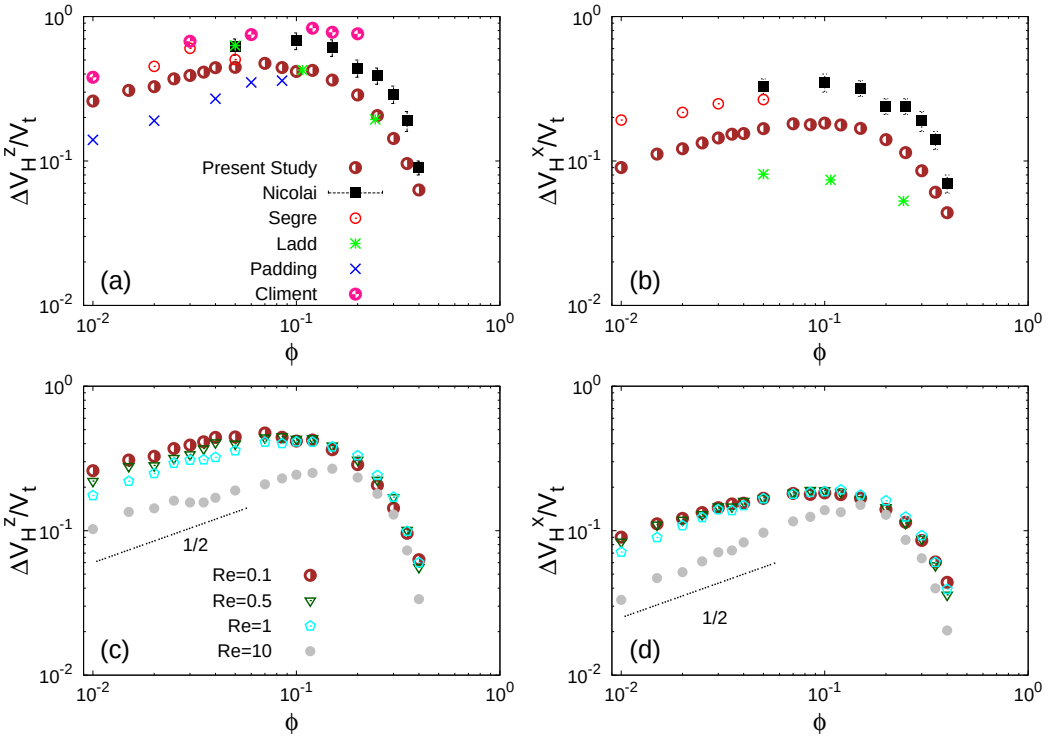

FIGURE 4.10: Scaling of the hydrodynamic velocity fluctuations normalized by the terminal velocity with respect to volume fraction for different Re. Figures "(a)" and "(b)" show the velocity fluctuations in z and x directions, respectively, for Re ≤ 0.5, which shows the typical Stokes regime characteristics. These results are also compared with the previous experimental data of Nicolai [5] and Segre [9] and simulation results of Ladd [18], Padding [23] and Climent [52]. Figures "(c)" and "(d)" show the velocity fluctuations in z and x directions, respectively, for different Re.

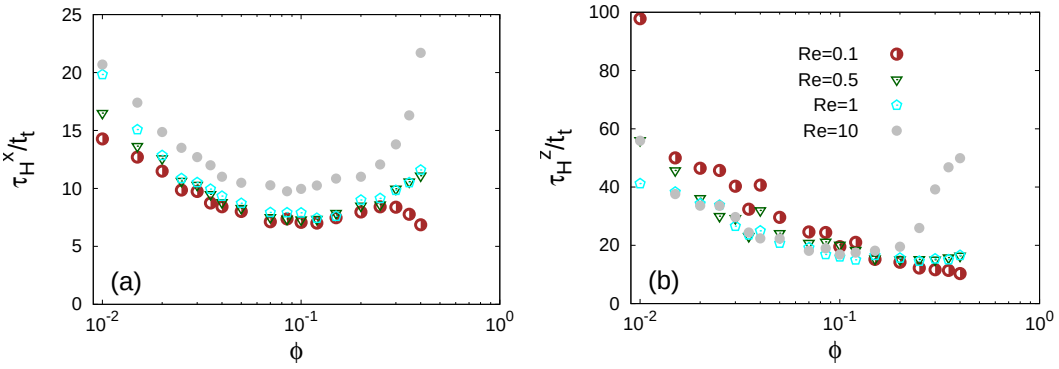

FIGURE 4.11: Decay of relaxation times normalized by the terminal time, as a function of volume fraction for different Re. Figures "(a)" and "(b)" show the x and z directions relaxation times, respectively.

relaxation times show the same quantitative behavior, whereas for Re=10, these are increased. A jump at $\phi \approx 0.3$ is attributed to the ordering of the particles, as shown in Fig 4.11(a). In contrast, the vertical relaxation time decreases with the increase of Re, at low volume fraction. At high volume fractions and Re ≤ 1 vertical relaxation times also show the same quantitative behavior,

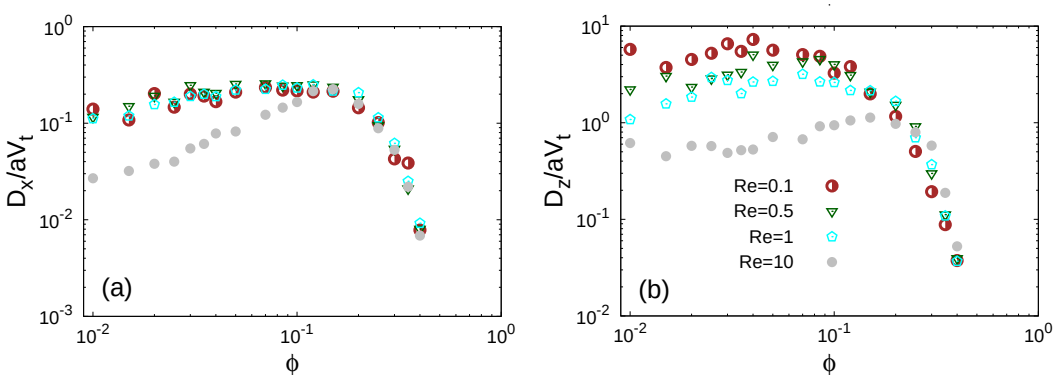

FIGURE 4.12: A comparison of the long time steady-state self-diffusion coefficients $D_\beta(\beta \in x,z)$, normalized by the product of particle radius a and terminal velocity V_t for different Re. Figures "(a)" and "(b)" show the horizontal and vertical directions, respectively.

as shown in Fig 4.11(b). The increase of relaxation time at Re=10 and at high volume fraction remains an open question.

4.4.5 Self-Diffusion

In the absence of an external force, particles exhibit an isotropic self-diffusion, whereas an external force such as gravity breaks this isotropic nature and induces the anisotropy in the system. We have seen the effects of the increase of inertial forces on the velocity fluctuations and their relaxation times. Both velocity fluctuations and their relaxation times dictate the diffusion of the particle. In order to quantify this dispersive motion, we calculated the self-diffusion from the slope of MSD in the x and z directions, as defined in Eqs. (2.12) and (2.13), respectively. The saturated value of these diffusion coefficients ($D_\beta = \lim_{t\to\infty} D_\beta(t)$) normalized by the product of the terminal velocity and particle radius are plotted in Fig. 4.12, as a function of volume fraction for different Re. It shows that at Re ≤ 0.5 the vertical diffusion coefficient shows the typical Stokes regime $\phi^{1/2}$ scaling at low volume fraction regime, decreasing at moderate volume fraction regime and then falls sharply at high volume fraction. The horizontal diffusion coefficient also increases as $\phi^{1/2}$ at low volume fractions, remains unchanged at moderate volume fraction and decreases sharply at high volume fractions, in good agreement with other studies [5,23,24]. The vertical diffusion coefficient decreases with the increase of Re at Re ≥ 1, whereas at high volume fraction this behavior becomes independent of Re, due to the dominance of many body interactions. Similar to the vertical velocity fluctuations, the effects of inertial forces is evident up to $\phi \lesssim 0.07$ at Re=1 and up to $\phi \lesssim 0.12$ at Re=10, which is attributed to change in microstructure, as discussed in Sections 4.4.3 and 4.4.4. Similar to horizontal velocity fluctuations, the diffusion coefficient in the horizontal direction remains unchanged at Re=1, due to small change in microstructure in horizontal direction, whereas at Re=10 a quantitatively large decrease in diffusion coefficient is evident up to $\phi \lesssim 0.12$, caused by the pronounced change in

the microstructure.

4.5 Concluding Remarks

We performed simulations of spherical particles for a volume fraction ranging from 0.01 to 0.4 and at finite Reynolds number. Inertial forces are increased with increasing Re, giving rise to a drafting-kissing-tumbling (DKT) mechanism [40]. With increasing Re, this mechanism creates a deficit of neighbouring particles which brings significant phenomenological changes and affects the transport properties of the suspension.

The microstructure analysis revealed that at Re ≤ 0.5, the microstructure shows the typical Stokes regime, non-Brownian particles characteristics, where at low volume fraction particles prefer to orient themselves in the horizontal direction and this preference decreases with increasing volume fraction and at high volume fraction $\phi \gtrsim 0.15$, the microstructure is isotropic due to dominance of many-body interactions. With the increase of inertial forces and the enhanced effects of the DKT mechanism, the microstructure shows the deficit of neighbouring particles around a test particle and this deficiency is stronger in the vertical direction than in the horizontal direction at Re=1. At Re=10, with the pronounced effects of inertial forces, both directions are affected by this deficiency and we also observed a shift in the radial distribution function's first peak. At high volume fractions, where many-body interactions dominate, microstructure resembles the typical Stokes regime's microstructure. Apart from the deficiency of the particles, the range of volume fraction affected by this deficiency is also increased with increasing Re.

The structural changes at high Re, strongly affected the transport properties of the suspension and at Re=1, where vertical velocity fluctuations and diffusion are decreased and the effects of inertial forces are visible up to $\phi \lesssim 0.07$, whereas above this range both properties resemble the Stokes regime's properties. In contrast, horizontal velocity fluctuations and diffusion remain unchanged at Re=1, due to less pronounced effects of inertial forces in the horizontal direction. Furthermore, at Re=10, due to strong effects of inertial forces, which caused the significant deficit of neighbouring particles in both directions, which in turn decreased both the vertical and horizontal velocity fluctuations and diffusion up to $\phi \lesssim 0.12$. Moreover, the vertical relaxation times decreased with the increase of Re at low volume fraction, whereas horizontal relaxation time increased with the increase of Re. Our analysis also revealed that at low volume fraction, where particles can interact with fewer neighbouring particles, microstructure governs the transport properties of the particles. With increasing Re, and the rise of the DKT mechanism creates the deficiency of the neighbouring particles, which means particles still interact with the fewer other particles even at higher volume fraction range, causing the microstructure to control the

transport properties of the suspension to the higher volume fraction range. At high volume fractions $\phi \gtrsim 0.15$, intrinsic many-body interactions suppress the DKT mechanism and takeover the control of transport properties.

Chapter 5

Conclusions

Sedimentation is one of the baffling and perplexing problems in colloidal science, due to the involvement of long space and time scales and the complexity involved in the accurate characterization of long ranged hydrodynamic interactions. Most of the experimental [5–13] and simulation [14–32] studies are carried out at low volume fraction, in the Stokes regime (Re of the order of 10^{-5} or less) and at large Peclet number (Pe) (of the order of 10^4 or larger) because: (a) at high volume fraction, it is difficult to track the particles by matching refractive index in experiments, whereas simulations require large cost; (b) at high Reynolds number (Re) phenomenological changes are so fast that these require very sophisticated instrumentation in experiments and a very refined mesh and small time step in simulations; (c) at small Pe, it is difficult to control the thermal force in experiments, whereas simulations require large simulation time. Hence, we investigated the above mentioned incomprehensively explored aspects of sedimentation by direct numerical simulations (DNS), using the smooth profile (SP) method because: (a) our method is insensitive to the number of particles because of the simplified boundary condition between the fluid and particles, which allows us to simulate dense suspension without any extra cost; (b) a fixed grid around the particles provides us a window to explore finite Re with relatively smaller cost, but we are limited to Re=10 because further increase in Re will increase the cost extensively; (c) thermal fluctuations are introduced in the particle domain as a random force, which can be controlled easily and effectively.

In this dissertation, we focused on characterizing the interplay of thermal and hydrodynamic interactions by increasing the Pe in Chapter 2, the behavior of non-Brownian particles in Chapter 3 and the effects of inertial forces at finite Re in Chapter 4. We analyzed the evolution of the microstruture, changes in the velocity fluctuations and their relaxation times and the behavior of the diffusion coefficients, as a function of Pe, Re, volume fraction and system size.

We found that at low Pe, thermal fluctuations are dominant, whereas at large Pe, hydrodynamic forces takeover the phenomena. Apart from these two regimes, we also observed a regime where both of these forces are trying to dominant each other. The analysis of microstructure, velocity

fluctuations, their relaxation times and particle diffusion at finite Pe revealed that at Pe $\gtrsim$ 30, hydrodynamic forces completely dominate the sedimentation phenomena and particles show typical non-Brownian characteristics.

The microsrtucture or the configuration of the particles is a key parameter because of its effects on transport properties, but little is known about its evolution and effects on transport properties. In this dissertation, we focused on the microstructure analysis and found that at low Pe, the microstructure is isotropic due to the dominance of thermal forces, whereas at high Pe (Pe $\gtrsim$ 30), we observed an anisotropic microstructure, where particles prefer to orient themselves horizontally with respect to a test particle. This anisotropic microstructure is attributed to the drafting-kissing-tumbling (DKT) mechanism, as explained by Koch [40]. At high Pe, with increasing volume fraction, this preference decreased and at large volume fraction ($\phi \gtrsim 0.15$), the microstructure became isotropic due to the dominance of many-body interactions. Inertial forces have very strong effects on the microstructure and at Re $\leq$ 0.5, the microstructure is similar to that of the Stoke regime, whereas at Re=1, it shows the deficiency of particles near a test particle at low volume fraction. This deficiency is more pronounced in the vertical direction than the horizontal one. At Re=10, with the enhanced DKT mechanism caused by the strong inertial forces, we observed the strong deficit of particles in both directions and the shift in the RDF peak. Apart from this deficiency, we also observed that the volume fraction range affected by the inertial force is also increased with increasing Re.

We also investigated the hydrodynamic velocity fluctuations, as a function of Pe, volume fraction, system size and Re. A finite Pe study revealed that at Pe $\gtrsim$ 30 hydrodynamic velocity fluctuations scaled with the Stokes velocity remained unchanged, due to dominance of hydrodynamic forces. We calculated the hydrodynamic velocity fluctuations at large Pe, where particles show the non-Brownian characteristics and reported both in Chapter 2 and 3. These velocity fluctuations followed a $\phi^{1/2}$ scaling, at low volume fraction regime ($\phi \lesssim 0.04$), due to the anisotropic microstructure, remained unchanged at moderate volume fraction or cross-over regime and decreased at the high volume fraction regime ($0.15 \lesssim \phi \leq 0.5$). The low volume fraction regime has been widely studied and Hinch [36] predicted that velocity fluctuations scale as $\phi^{1/2}$ at low volume fraction and this scaling has also been verified by other studies [23, 24, 52]. Our study is also in good agreement with Hinch's prediction. At high volume fractions, the phenomena is rather trivial, where the microstructure is isotropic due to many-body interactions, which suppressed the individual particle motion and transport properties are determined by the movement of clusters. Apart from these two regimes, we have the cross-over regime, where velocity fluctuations remain unchanged due to the interplay of anisotropic microstructure and many-body phenomena. Apart from the velocity fluctuations scaling with respect to the volume fraction, we also investigated its dependence on system size. We found that these velocity fluctuations show a $(L/a)^{1/2}$ scaling with respect to system size for $L/a \leq 64$, in accordance with the theoretical predictions [36]. Inertial forces had a strong effect on velocity fluctuations and these decreased with increasing Re at Re $\geq$ 1. We observed that velocity fluctuations at Re $\leq$ 0.5 showed the

Stokes regime characteristics. At Re=1, vertical fluctuations are decreased due to deficit of the particles in the vertical direction, whereas horizontal velocity fluctuations remained unchanged, as the microstructure did not show significant change in this direction. Apart from the decrease in vertical velocity fluctuations, the range of volume fraction affected by the inertial force is also extended up to $\phi \lesssim 0.07$. With a further increase in the inertial force at Re=10, a decrease of velocity fluctuations in both directions and an increase of affected volume fraction range up to $\phi \lesssim 0.12$ is observed.

Along with the velocity fluctuations, their relaxation time is another key parameter that dictates the dispersive motion of the particles. The vertical and horizontal relaxation times decreased as $\phi^{-1/2}$ at low volume fraction, in accordance with the theoretical predictions [36] and other studies [5, 23]. At the cross-over regime, the horizontal relaxation time remained unchanged, whereas the vertical relaxation time followed the same $\phi^{-1/2}$ scaling. At high volume fraction regime, we observed a sharp decrease in the relaxation times at $\phi > 0.3$ in both directions, mainly because of the ordering of the particles, whereas a jump in the relaxation time at $\phi = 0.5$ could be because of very long range ordering of the particles and the artefacts generated from the use of a finite-width interface. Our results showed large relaxation times at low volume fraction because of the cubic system size and finite size effects. The finite size effects are decreased with increasing volume fraction and the difference between the vertical and horizontal relaxation times are also decreased. Inertial forces increased the horizontal relaxation time at the low volume fraction and decreased the vertical relaxation times.

A particle settling in the vicinity of other particles performs a random walk characteristic of a diffusion process. We found that the diffusion coefficient normalized by the equilibrium diffusion coefficient increased linearly at high Pe, with increasing Pe, which shows the dominance of hydrodynamic interactions. We found that at low volume fraction and high Pe vertical and horizontal diffusion coefficients followed a $\phi^{1/2}$ scaling in good agreement with the theory [36], whereas at the cross-over regime (high Pe) the vertical diffusion coefficient decreased and the horizontal diffusion coefficient remained unchanged. The different behavior at the cross-over regime is attributed to the different scaling of relaxation times. At the high volume fraction regime both of these coefficients decreased due to many-body interactions. Anisotropy in diffusion is increased with the increase of Pe and saturated at high Pe. The saturated value of this anisotropy remains unchanged at the low volume fraction and then decreased at the cross-over and high volume fraction regimes. The high value at the low volume fraction is due to the cubic simulation box and finite system size. Particle diffusion showed the Stokes regime behavior as explained above at Re ≤ 0.5, whereas at Re=1 and 10 it is decreased due to deficit of the particles in the vicinity of a test particle. At Re=1, the effect of inertial forces in the vertical direction is more pronounced and it decreased the particle diffusion, whereas horizontal diffusion had a very little effect. At Re=10, we observed a significant decrease in the diffusion coefficient in both directions due to a large deficiency of the particles. This decrease extends over a larger volume fraction range, until many-body interactions dominate the phenomena.

Bibliography

[1] D. L. Koch and E. Shaqfeh, "Screening in sedimenting suspensions," *J. Fluid Mech.*, vol. 224, 1991.

[2] A. Levine, S. Ramaswamy, E. Frey, and R. Bruinsma, "Screened and unscreened phases in sedimenting suspensions," *Phys. Rev. Lett.*, vol. 81, no. 26, pp. 5944–5947, 1998.

[3] D. L. Koch, "Hydrodynamic diffusion in a suspension of sedimenting point particles with periodic boundary conditions," *Phys. Fluids*, vol. 6, pp. 2894–2900, 1994.

[4] R. E. Caflisch and J. H. C. Luke, "Variance in the sedimentation speed of a suspension," *Phys. Fluids*, vol. 28, no. 3, p. 759, 1985.

[5] H. Nicolai, B. Herzhaft, E. J. Hinch, L. Oger, and E. Guazzelli, "Particle velocity fluctuations and hydrodynamic of sedimenting non-Brownian spheres," *Phys. Fluids*, vol. 7, no. 1, pp. 12–23, 1995.

[6] H. Nicolai and E. Guazzelli, "Effect of the vessel size on the hydrodynamic diffusion of sedimenting spheres," *Phys. Fluids*, vol. 7, no. 1, pp. 3–5, 1995.

[7] H. Nicolai, Y. Peysson, and E. Guazzelli, "Velocity fluctuations of a heavy sphere falling through a sedimenting suspension," *Phys. Fluids*, vol. 8, no. 4, pp. 855–862, 1996.

[8] P. N. Segrè, O. P. Behrend, and P. N. Pusey, "Short-time Brownian motion in colloidal suspensions: Experiment and simulation," *Phys. Rev. E*, vol. 52, no. 5, pp. 5070–5083, 1995.

[9] P. N. Segrè, E. Herbolzheimer, and P. M. Chaikin, "Long-range correlations in sedimentation," *Phys. Rev. Lett.*, vol. 79, no. 13, pp. 2574–2577, 1997.

[10] P. Segrè, F. Liu, P. Umbanhowar, and D. A. Weitz, "An effective gravitational temperature for sedimentation," *Nature*, vol. 409, pp. 594–597, 2001.

[11] P. N. Segrè and J. McClymer, "Fluctuations, stratification and stability in a liquid fluidized bed at low Reynolds number," *J. Phys. Condens. Matter*, vol. 16, pp. S4219–S4230, 2004.

[12] S.-Y. Tee, P. J. Mucha, L. Cipelletti, S. Manley, M. P. Brenner, P. N. Segrè, and D. A. Weitz, "Nonuniversal velocity fluctuations of sedimenting particles," *Phys. Rev. Lett.*, vol. 89, no. 5, pp. 3–6, 2002.

[13] G. Bernard-Michel, A. Monavon, D. Lhuillier, D. Abdo, and H. Simon, "Particle velocity fluctuations and correlation lengths in dilute sedimenting suspensions," *Phys. Fluids*, vol. 14, no. 7, p. 2339, 2002.

[14] A. J. C. Ladd, "Dynamical simulations of sedimenting spheres," *Phys. Fluids A*, vol. 5, no. 2, pp. 299–310, 1993.

[15] A. J. C. Ladd, "Hydrodynamic screening in sedimenting suspensions of non-Brownian spheres," *Phys. Rev. Lett.*, vol. 76, no. 8, pp. 1392–1395, 1996.

[16] A. J. C. Ladd and R. Verberg, "Lattice-Boltzmann Simulations of Particle-Fluid Suspensions," *J. Stat. Phys.*, vol. 104, no. 5/6, pp. 1191–1251, 2001.

[17] A. J. C. Ladd, "Effects of container walls on the velocity fluctuations of sedimenting spheres," *Phys. Rev. Lett.*, vol. 88, p. 048301, Jan. 2002.

[18] A. J. C. Ladd, "Sedimentation of homogeneous suspensions of non-Brownian spheres," *Phys. Fluids*, vol. 9, no. 3, pp. 491–499, 1997.

[19] R. Verberg and A. J. C. Ladd, "Accuracy and stability of a lattice-Boltzmann model with subgrid scale boundary conditions," *Phys. Rev. E*, vol. 65, p. 016701, Dec. 2001.

[20] N.-Q. Nguyen and A. J. C. Ladd, "Sedimentation of hard-sphere suspensions at low Reynolds number," *J. Fluid Mech.*, vol. 525, pp. 73–104, Feb. 2005.

[21] J. T. Padding and A. Louis, "Hydrodynamic and brownian fluctuations in sedimenting suspensions," *Phys. Rev. Lett.*, vol. 93, p. 220601, 2004.

[22] J. T. Padding and A. Louis, "Hydrodynamic interactions and Brownian forces in colloidal suspensions: Coarse-graining over time and length scales," *Phys. Rev. E*, vol. 74, p. 031402, 2006.

[23] J. T. Padding and A. A. Louis, "Interplay between hydrodynamic and Brownian fluctuations in sedimenting colloidal suspensions," *Phys. Rev. E*, vol. 77, p. 011402, 2008.

[24] F. R. Cunha, G. C. Abade, A. J. Sousa, and E. J. Hinch, "Modeling and Direct Simulation of Velocity Fluctuations and Particle-Velocity Correlations in Sedimentation," *J. Fluids Eng.*, vol. 124, no. 4, p. 957, 2002.

[25] S.-Y. Tee, P. J. Mucha, M. P. Brenner, and D. A. Weitz, "Velocity fluctuations of initially stratified sedimenting spheres," *Phys. Fluids*, vol. 113304, p. 113304, 2012.

[26] M. Miguel and R. Pastor-Satorras, "Velocity fluctuations and hydrodynamic diffusion," *Europhys. Lett.*, vol. 54, no. 1, pp. 45–50, 2001.

[27] E. Kuusela, K. A. I. Höfler, and S. Schwarzer, "Computation of particle settling speed and orientation distribution in suspensions of prolate spheroids," *J. Eng. Math.*, vol. 41, pp. 221–235, 2001.

[28] E. Kuusela and T. Ala-Nissila, "Velocity correlations and diffusion during sedimentation," *Phys. Rev. E*, vol. 63, p. 061505, May 2001.

[29] E. Kuusela, J. M. Lahtinen, and T. Ala-Nissila, "Collective effects in settling of spheroids under steady-state sedimentation," *Phys. Rev. Lett.*, vol. 90, p. 094502, Mar. 2003.

[30] E. Kuusela, J. M. Lahtinen, and T. Ala-Nissila, "Sedimentation dynamics of spherical particles in confined geometries," *Phys. Rev. E*, vol. 69, p. 066310, June 2004.

[31] E. Kuusela, J. M. Lahtinen, and T. Ala-Nissila, "Origin of non-Gaussian velocity distributions in steady-state sedimentation," *Europhys. Lett.*, vol. 65, no. 1, pp. 13–19, 2004.

[32] P. Mucha and M. Brenner, "Diffusivities and front propagation in sedimentation," *Phys. Fluids*, vol. 15, no. 5, pp. 1305–1313, 2003.

[33] G. G. Stokes, *Mathematical and physical papers*. New York: Johnson Reprint Corporation, 1996.

[34] D. Cassidy, *Einstein and Our World*. Humanities Press, 2nd ed., 1999.

[35] G. K. Batchelor, "Sedimentation in a dilute dispersion of spheres," *J. Fluid Mech.*, vol. 52, no. 2, p. 245, 1972.

[36] E. J. Hinch, *Disorder and Mixing*. Netherland: Kluwer Academic publisher, 1988.

[37] G. K. Batchelor and V.-R. R. W. J, "Structure formation in bidisperse sedimentation," *J. Fluid Mech.*, vol. 166, pp. 379–407, 1986.

[38] Y. Peysson and E. Guazzelli, "An experimental investigation of the intrinsic convection in a sedimenting suspension," *Phys. Fluids*, vol. 10, no. 1, p. 44, 1998.

[39] M. P. Brenner, "Screening mechanisms in sedimentation," *Phys. Fluids*, vol. 11, no. 4, p. 754, 1999.

[40] X. Yin and D. L. Koch, "Velocity fluctuations and hydrodynamic diffusion in finite-Reynolds-number sedimenting suspensions," *Phys. Fluids*, vol. 20, no. 4, p. 043305, 2008.

[41] C. Beenakker and P. Mazur, "Self-diffusion of spheres in a concentrated suspension," *Physica A*, vol. 120, pp. 388–410, 1983.

[42] C. W. J. Beenakker and P. Mazur, "Diffusion of spheres in a concentrated suspension: resummation of many-body hydrodynamic interactions," *Phys. Lett.*, vol. 98A, no. 1, pp. 22–24, 1983.

[43] C. W. J. Beenakker, W. V. A. N. Saarloos, and P. Mazur, "Many-sphere hydrodynamic interactions III. The influence of a plane wall," *Physica A*, vol. 127, pp. 451–472, 1984.

[44] J. Ham and G. Homsy, "Hindered settling and hydrodynamic dispersion in quiescent sedimenting suspensions," *Int. J. Multiph. Flow*, vol. 14, no. 5, pp. 533–546, 1988.

[45] X. Yin and D. L. Koch, "Hindered settling velocity and microstructure in suspensions of solid spheres with moderate Reynolds numbers," *Phys. Fluids*, vol. 19, no. 9, p. 093302, 2007.

[46] D. L. Koch, "Hydrodynamic diffusion in dilute sedimenting suspensions at moderate Reynolds numbers," *Phys. Fluids A*, vol. 5, no. 5, p. 1141, 1993.

[47] E. Kuusela, *Steady-state sedimentation of non-brownian particles with finite Reynolds number*. PhD thesis, Helsinki University of Technology, Espoo, Finland, 2005.

[48] A. Hamid, J. J. Molina, and R. Yamamoto, "Sedimentation of non-Brownian spheres at high volume fractions," *Soft Matter*, vol. 9, pp. 10056–10068, 2013.

[49] A. Hamid and R. Yamamoto, "Anisotropic velocity fluctuations and particle diffusion in sedimentation," *J. Phys. Soc. Japan*, vol. 82, no. 2, p. 024004, 2013.

[50] A. Hamid and R. Yamamoto, "Direct numerical simulations of anisotropic diffusion of spherical particles in sedimentation," *Phys. Rev. E*, vol. 87, no. 2, p. 022310, 2013.

[51] A. Hamid and R. Yamamoto, "Sedimentation at finite peclet number: Direct numerical simulation," *AIP Conf. Proc.*, vol. 1518, pp. 444–447, 2013.

[52] E. Climent and M. Maxey, "Numerical simulations of random suspensions at finite Reynolds numbers," *Int. J. Multiph. Flow*, vol. 29, pp. 579–601, Apr. 2003.

[53] S. Jafari, R. Yamamoto, and M. Rahnama, "Lattice-Boltzmann method combined with smoothed-profile method for particulate suspensions," *Phys. Rev. E*, vol. 83, p. 026702, Feb. 2011.

[54] R. Yamamoto, Y. Nakayama, and K. Kim, "A method to resolve hydrodynamic interactions in colloidal dispersions," *Comput. Phys. Commun.*, vol. 169, pp. 301–304, July 2005.

[55] R. Yamamoto, Y. Nakayama, and K. Kim, "Smoothed profile method to simulate colloidal particles in complex fluids," *Int. J. Mod. Phys. C*, vol. 20, no. 9, pp. 1457–1465, 2009.

[56] R. Yamamoto, Y. Nakayama, and K. Kim, "A smooth interface method for simulating liquid crystal colloid dispersions," *J. Phys. Condens. Matter*, vol. 16, pp. S1945–S1955, May 2004.

[57] R. Yamamoto, K. Kim, and Y. Nakayama, "Strict simulations of non-equilibrium dynamics of colloids," *Colloids Surfaces A Physicochem. Eng. Asp.*, vol. 311, pp. 42–47, 2007.

[58] R. Yamamoto, K. Kim, Y. Nakayama, K. Miyazaki, and D. R. Reichman, "On the role of hydrodynamic interactions in colloidal gelation," *J. Phys. Soc. Japan*, vol. 77, p. 084804, Aug. 2008.

[59] H. Tanaka and T. Araki, "Simulation method of colloidal suspensions with hydrodynamic interactions : fluid particle dynamics," *Phys. Rev. Lett.*, vol. 85, no. 6, pp. 1338–1341, 2000.

[60] Y. Nakayama, K. Kim, and R. Yamamoto, "Simulating (electro) hydrodynamic effects in colloidal dispersions : Smoothed profile method," *Eur. Phys. J. E*, vol. 368, pp. 361–368, 2008.

[61] A. Zick and G. Homsy, "Stokes flow through periodic arrays of spheres," *J. Fluid Mech.*, vol. 115, pp. 13–26, 1982.

[62] W. McCabe, J. Smith, and P. Harriott, *Unit Operations of Chemical Engineering*. McGraw Hill Chemical Engineering Series, 7th ed., 2004.

[63] T. Iwashita, Y. Nakayama, and R. Yamamoto, "Velocity autocorrelation function of fluctuating particles in incompressible fluids," *Prog. Theor. Suppl.*, vol. 11, no. 178, pp. 86–91, 2009.

[64] A. Ahmed and R. J. Sadus, "Phase diagram of the Weeks-Chandler-Anderson potential from very low to high temperature and pressure," *Phys. Rev. E*, vol. 80, p. 061101, 2009.

[65] Y. Nakayama and R. Yamamoto, "Simulation method to resolve hydrodynamic interactions in colloidal dispersions," *Phys. Rev. E*, vol. 71, p. 036707, Mar. 2005.

[66] R. B. Bird, W. E. Stewart, and E. N. Lightfoot, *Transpor Phenomena*. John Wiley and Sons, 2nd ed., 2006.

[67] Y. Nakayama, K. Kim, and R. Yamamoto, "Direct simulation of flowing colloidal dispersions by smoothed profile method," *Adv. Powder Technol.*, vol. 21, no. 2, pp. 206–211, 2010.

[68] Y. Nakayama, K. Kim, and R. Yamamoto, "Hydrodynamic effects in colloidal dispersions studied by a new efficient direct simulation," *AIP Conf. Proc.*, pp. 245–251, 2006.

[69] K. Kim, Y. Nakayama, and R. Yamamoto, "Direct numerical simulations of electrophoresis of charged colloids," *Phys. Rev. Lett.*, vol. 96, p. 208302, May 2006.

[70] K. Kim, Y. Nakayama, and R. Yamamoto, "Simulating (electro)hydrodynamic effects in colloidal dispersions: smoothed profile method," *AIP Conf. Proc.*, pp. 251–256, Aug. 2006.

[71] T. Iwashita, Y. Nakayama, and R. Yamamoto, "A numerical model for brownian particles fluctuating in incompressible fluids," *J. Phys. Soc. Japan*, vol. 77, p. 074007, July 2008.

[72] T. Iwashita and R. Yamamoto, "Short-time motion of Brownian particles in a shear flow," *Phys. Rev. E*, vol. 79, p. 031401, Mar. 2009.

[73] T. Iwashita and R. Yamamoto, "Direct numerical simulations for non-Newtonian rheology of concentrated particle dispersions," *Phys. Rev. E*, vol. 80, p. 061402, 2009.

[74] T. Iwashita, Y. Nakayama, and R. Yamamoto, "Velocity autocorrelation function of fluctuating particles in incompressible fluids," *Prog. Theor. Suppl.*, vol. 11, no. 178, pp. 86–91, 2008.

[75] T. Iwashita, T. Kumagai, and R. Yamamoto, "A direct numerical simulation method for complex modulus of particle dispersions," *Eur. Phys. J. E*, vol. 32, pp. 357–63, Aug. 2010.

[76] H. Kobayashi and R. Yamamoto, "Reentrant transition in the shear viscosity of dilute rigid-rod dispersions," *Phys. Rev. E*, vol. 84, p. 051404, Nov. 2011.

[77] H. Kobayashi and R. Yamamoto, "Implementation of Lees-Edwards periodic boundary conditions for direct numerical simulations of particle dispersions under shear flow," *J. Chem. Phys.*, vol. 134, p. 064110, Feb. 2011.

[78] H. Kobayashi and R. Yamamoto, "Tumbling motion of a single chain in shear flow: A crossover from Brownian to non-Brownian behavior," *Phys. Rev. E*, vol. 81, p. 041807, Apr. 2010.

[79] J. J. Molina, Y. Nakayama, and R. Yamamoto, "Hydrodynamic interactions of self-propelled swimmers," *Soft Matter*, vol. 9, pp. 4923–4936, 2013.

[80] J. J. Molina and R. Yamamoto, "Direct numerical simulations of rigid body dispersions. I. Mobility/Friction tensors of assemblies of spheres," *J. Chem. Phys.*, 2013.

[81] R. Tatsumi and R. Yamamoto, "Direct numerical simulation of dispersed particles in a compressible fluid," *Phys. Rev. E*, vol. 85, p. 066704, June 2012.

[82] R. Tatsumi and R. Yamamoto, "Propagation of hydrodynamic interactions between particles in a compressible fluid," *Phys. Fluids*, vol. 25, no. 4, p. 046101, 2013.

[83] R. Tatsumi and R. Yamamoto, "Velocity relaxation of a particle in a confined compressible fluid," *J. Chem. Phys.*, vol. 138, p. 184905, May 2013.

[84] X. Luo, M. R. Maxey, and G. E. Karniadakis, "Smoothed profile method for particulate flows: Error analysis and simulations," *J. Comput. Phys.*, vol. 228, pp. 1750–1769, Mar. 2009.

[85] R. M. Kirby, T. C. Warburton, I. Lomtev, and G. E. Karniadakis, "A discontinuous galerkin spectral/hp method on hybrid grids," *Appl. Numer. Math.*, vol. 33, pp. 393–405, 2000.

[86] D. L. Koch and E. Shaqfeh, "The instability of a dispersion of sedimenting spheroids," *J. Fluid Mech.*, vol. 209, pp. 521–542, 1989.

[87] E. Guazzelli and J. Hinch, "Fluctuations and instability in sedimentation," *Annu. Rev. Fluid Mech.*, vol. 43, pp. 97–116, Jan. 2011.

[88] D. C. Rapaport, *The art of molecular dynamics simulation*. Edinburgh: Cambridge university press, 2nd ed., 2004.

[89] G. Bossis and J. F. Brady, "Self-diffusion of Brownian particles in concentrated suspensions under shear," *J. Chem. Phys.*, vol. 87, no. 9, pp. 5437–5448, 1987.

[90] M. S. Wertheim, "Exact solution of the PERCUS-YEVICK integral equation for hard spheres," *Phys. Rev. Lett.*, vol. 10, p. 321, 1963.

[91] R. F. Richardson and W. N. Zaki, "Sedimentation and fluidisation. Part 1," *Trans. Inst. Chem. Eng.*, vol. 32, pp. 35–53, 1954.

[92] J. Garside and M. Al-Dibouni, "Velocity-voidage relationships for fluidization and sedimentation in solid-liquid systems," *Ind. Eng. Chem. Process Des. Dev.*, vol. 16, no. 2, pp. 206–2014, 1977.

[93] H. Hayakawa and K. Ichiki, "Statistical theory of sedimentation of disordered suspensions," *Phys. Rev. E*, vol. 51, no. 5, pp. R3815–R3818, 1995.

[94] J. F. Brady and L. J. Durlofsky, "The sedimentation rate of disordered suspensions," *Phys. Fluids*, vol. 31, no. 4, p. 717, 1988.

[95] R. Di Felice, "The sedimentation velocity of dilute suspensions of nearly monosized spheres," *Int. J. Multiph. Flow*, vol. 25, pp. 559–574, 1999.

[96] D. Saintillan, E. S. G. Shaqfeh, and E. Darve, "The effect of stratification on the wave number selection in the instability of sedimenting spheroids," *Phys. Fluids*, vol. 18, p. 121503, 2006.

[97] D. C. Rapaport and E. Clementi, "Eddy formation in obstructed fluid flow: A molecular-Dynamcis study," *Phys. Rev. Lett.*, vol. 57, no. 6, pp. 695–698, 1986.

[98] A. A. Johnson and T. E. Tezduyar, "Simulation of multiple spheres falling in a liquid-filled tube," *Comput. Methods Appl. Mech. Eng.*, vol. 134, no. 3, pp. 351–373, 1995.

[99] R. Clift, J. R. Grace, and M. E. Weber, *Bubbles, Drops and Particles*. Academic Press, London, 1978.

[100] R. Di Felice and E. Parodi, "Wall effects on the sedimentation velocity of suspensions in viscous flow," *Am. Inst. Chem. Eng. J.*, vol. 42, no. 4, pp. 927–931, 1996.

[101] R. Di Felice and R. Kehlenbeck, "Sedimentation Velocity of Solids in Finite Size Vessels," *Chem. Eng. Technol.*, vol. 23, no. 12, pp. 1123–1126, 2000.

[102] Y. Chong, D. Ratkowsky, and N. Epstein, "Effect of particle shape on hindered settling in creeping flow," *Powder Technol.*, vol. 23, pp. 55–66, May 1979.